Winding Function Modeling of Synchronous Reluctance Machines

Seyede Sara Maroufian

A Thesis

In the Department

of

Electrical and Computer Engineering

Presented in Partial Fulfillment of the Requirements

For the Degree of

Doctor of Philosophy (Electrical and Computer Engineering) at

Concordia University

Montreal, Quebec, Canada

August 2018

CONCORDIA UNIVERSITY

SCHOOL OF GRADUATE STUDIES

This is to certify that the thesis prepared

By: Seyede Sara Maroufian

Entitled: Winding Function Modeling of Synchronous Reluctance Machines

and submitted in partial fulfillment of the requirements for the degree of

Doctor of Philosophy (Electrical and Computer Engineering)

complies with the regulations of the University and meets the accepted standards with respect to originality and quality.

Signed by the final examining committee:

_____Chair

Dr. Luis Amador

_____External Examiner

Dr. Joseph O. Ojo

_____External to program

Dr. Marius Paraschivoiu

_____Examiner

Dr. Chunyan Lai

_____Examiner

Dr. Luiz. A.C. Lopes

_____Thesis Supervisor

Dr. Pragasen Pillay

Approved by: _____

Dr. William E. Lynch, Chair of Department

October 01, 2018

Date of defense   _____

Dr. Amir Asif, Dean, Gina Cody School of Engineering and Computer Science

ABSTRACT

Winding Function Modeling of Synchronous Reluctance Machines

Seyede Sara Maroufian, Ph.D.
Concordia University, 2018

The current electric vehicle market, as well as many other industrial applications, is heavily focused on the application of permanent magnet (PM) machines and induction machines (IM). However the limitations of these two types of electric machines reveal the necessity for further research in the field of electrical machines to substitute the existing types with less expensive, and more fault tolerant machines. The synchronous reluctance machine (SynRM) is a singly excited machine with great potential to replace permanent magnet machines and induction machines in traction, as well as many other industrial applications. The rotor structure is simple and only made of steel laminations, which makes the manufacturing procedure less expensive compared to PM machines and IMs. Moreover the absence of rotor windings and a rotor cage eliminates the rotor copper loss, thus enhancing the efficiency compared to IMs. However, the use of the SynRM has not yet reached the same maturity level of its counterparts and still faces problems like low power density, poor power factor, and limited torque-speed envelope, representing a fertile terrain for research.

The aim of this research is to develop an analytical approach based on the winding function method for modeling, analysis, and design of SynRMs and PM assisted SynRMs. The proposed analytical approach is based on the winding configuration of the machine, and the magnetic characteristics of the rotor topology. It provides insight of the machine's characteristics, and can be used to apply design modifications on existing SynRMs to improve the performance of future designs. The analytical model is later modified for designing a PM assisted SynRM using AlNiCo magnets, with the aim to improve the power factor and torque density of the regular SynRM.

The self-excitation phenomenon in synchronous reluctance generators (SynRGs) is also investigated and the requirements for the assurance of self-excitation are identified. Therefore

in traction applications, and electric vehicles with vehicle to grid (V2G) capability, the possibility of utilizing the onboard SynRM as a power generation unit for emergency situations can be considered. The stand-alone SynRG can also be used as a fault tolerant power generation unit to supply electric power in remote areas.

Acknowledgement

My sincere appreciation goes to my supervisor, Prof. Pillay for his help, support, and guidance through the past 4 years. He has been more than just a supervisor, he has been my mentor. He gave me the opportunity to pursue my dreams 4 years ago for which I will forever be grateful.

I appreciate the valuable comments and suggestions from the committee members, specially Prof. Ojo, and Dr. Lai, who have helped to improve this thesis.

I would like to thank my friends and colleagues in PEER Group; Amit, Rajendra, and Chirag for helping me during the experiments; Amir, Gabriel, and again Amit for their valuable friendships; and all the members of the PEER Group for being part of the new family I found in Canada.

Finally I would like to thank my family, for their support, help, and trust in my decisions. My father has been always my greatest support, and my mother has been my role model as a woman. I would also like to thank my little brother, Arash, for being the "Best Brother" one could ever ask for.

To my little brother, Arash

Table of Contents

List of Figures

List of Tables

List of Abbreviations

ALA	Axially laminated anisotropic
CRGO	Cold rolled grain oriented
CRNGO	Cold rolled non grain oriented
EMF	Electromotive force
ESS	Energy storage system
EV	Electric vehicle
FEA	Finite element analysis
HEV	Hybrid electric vehicle
ICE	Internal combustion engine
IPM	Interior permanent magnet machine
MEC	Magnetic equivalent model
MMF	Magneto motive force
PHEV	Plug-in hybrid electric vehicle
PM	Permanent magnet
PMSM	Permanent magnet synchronous machine
PWM	Pulse width modulation
SynRG	Synchronous reluctance generator
SynRM	Synchronous reluctance machine
TLA	Transversally laminated anisotropic
V2G	Vehicle to grid

List of Symbols

A_g	Air gap area
A_m	Permanent magnet surface area
B_m	Magnetic flux density of the permanent magnet at the operating point
B_r	Remnant magnet flux density of the magnet
B_{rad}	Radial component of the magnetic flux density in the air gap
B_{tan}	Tangential component of the magnetic flux density in the air gap
$C_\emptyset$	Flux concentration factor
H_R	Reversible field
H_d	Demagnetization field
H_l	Irreversible field
H_m	Magnetic field intensity of the permanent magnet at the operating point
I_s	Current vector
K_c	Carter's coefficient
L_d	d-axis inductance
L_m	Magnetizing inductance
L_q	q-axis inductance
N_d	Demagnetization factor
P_c	Permeance coefficient
R_c	Core loss resistance
R_s	Phase winding resistance
i_d	d-axis current
i_q	q-axis current
l_{fb}	Equivalent air gap length of the flux barrier
l_g	Air gap thickness
l_{stack}	Stack length of the machine
v_d	d-axis voltage
v_q	q-axis voltage
$\mathbb{T}$	Maxwell stress tensor
λ_d	d-axis flux linkage
λ_{pm}	Flux linkage due to the permanent magnet
λ_q	q-axis flux linkage
μ_0	Magnetic permeability of the free space
μ_R	Relative magnetic permeability
ω_r	Rotor speed (rad/s)

$\mathcal{F}$	Magneto motive force (MMF)
$\mathcal{R}$	Reluctance
C	Capacitance
D	Outer diameter of the rotor
H	Magnetic field intensity
J	Current density
K	Torque constant
M	Total magnetization
$N(\theta)$	Winding function
T	Electromagnetic torque
V	Phase voltage
g	Air gap function
m	Relative magnetization
P	Number of poles
θ	Rotor angle
ξ	Saliency ratio
φ	Magnetic flux
ω	Electrical speed and speed of the frame (rad/s)
ϑ	Power factor angle

Chapter 1   Introduction

1. 1.   Potential Applications of Synchronous Reluctance Machines

With recent developments in power electronics and electrical machine design, the application of pure electric vehicles and hybrid electric vehicles, to replace the conventional ones, has become more economically feasible. This has led to the design and manufacturing of varieties of electric vehicles (EVs) which are usually categorized into three main groups. The first group is the purely electric vehicle without the internal combustion engine (ICE) [1]. The abbreviation, EV is sometimes used interchangeably for electric vehicles of this category. The second group is the combined system of an EV and a conventional ICE, named as Hybrid Electric Vehicle (HEV). The third group is a variation of HEV in which the possibility of charging the energy storage system (ESS) through the utility grid is provided [2]. This group is the Plug-in Hybrid Electric Vehicle (PHEV).

The ESS of a HEV, which is usually a battery pack is exclusively charged through the regenerative braking procedure, or using a small on-board electric generator driven by the ICE, while the main source of recharging the batteries in EVs and PHEVs is the on board battery charger through which the vehicle is plugged to the electrical grid. The on board battery charger can be designed to provide electric power flow in both directions, thus enabling the possibility to send the power back to the grid. Such EVs or PHEVs is said to have the vehicle to grid capability (V2G) [1, 3] and can operate as a distributed power generation system to provide the peak power demand of the utility grid or to operate as a stand-alone electric power generation unit for emergency situations [1, 4]. In the generation mode, current research is focusing on utilizing the stored energy in the batteries. However in a PHEV the option to use the on board electric machine operating as the generator, driven by the ICE as the prime mover, also exists. Therefore the choice of the electric machine for a PHEV must consider this possibility, as well.

Different types of electrical machines can be used as the electric propulsion motor of the EV. Currently permanent magnet machines (PM machines) are the most popular type of electrical machines used in the EV industry. However the cost and limitations of PM machines create a motivation to find an alternative electric machine which has the capability to overcome

those limitations and provide the same performance. The synchronous reluctance machine (SynRM) possess unique characteristics which makes it an interesting choice for EVs. The absence of PMs in the SynRM makes the manufacturing and maintenance cost comparatively low. It also provides a fault tolerant machine which is capable of operation at high speed and at high temperature [5].

The SynRM is considered as a potential candidate to replace PM machines, and induction machines in the current market of EVs. In principle, the SynRM operates in the same manner as the traditional salient pole synchronous machine except that the rotor of a SynRM has no excitation winding, and operates based on the inductance ratio of the d-axis, and q-axis, named as the saliency ratio [6]. A higher saliency ratio results in higher torque density, higher power factor, and an improved performance. Therefore, enhancing this ratio has been the motivation of several research works [7, 8, 9].

The absence of rotor windings also provides other benefits to this type of electric machine, which is lower copper loss and the possibility to operate at higher temperatures compared to IMs and PM machines. The SynRM also shares many of the advantages of the switched reluctance machine (SRM) [10, 11]; however since it uses a distributed three phase winding identical to the induction machine's stator winding, its operation is smoother and quieter than the SRM.

In this research the electrical machine as the main component which distinguishes an EV from a conventional vehicle, is studied. The design of the electric machine used in the electrical propulsion system, affects the performance of the vehicle significantly. Therefore it is important to enhance the machine's performance by choosing proper design parameters. Analytical design methods which can provide an insight to the magnetic and electric characteristics of electrical machines are powerful tools to achieve the desired output parameters, required by the application. An analytical method, based on the electromagnetic equations for SynRMs is proposed in this thesis. The analytical approach creates an opportunity to characterize and analyze the existing SynRMs, and has the capability to be transformed into a design method through which the choice of design parameters can be done for the specific requirements of EV as well as other application. The generator application of the SynRM is also studied and its criteria are identified. The importance of this study is to identify the possibility of V2G

operation for a PHEV, which utilizes the SynRM in its propulsion system. Such a vehicle can also be used to supply emergency power, when needed. Thus the electric power generation capability of the electric machine is of great importance.

Despite numerous merits to this date, SynRMs are not commercialized at the same level of induction machines, and their applications are limited to small fans and pumps [12]. However the advantages of the SynRM such as low copper loss and low manufacturing cost reveals the SynRM's potential to substitute the induction machine in many applications. This chapter briefly introduces SynRMs, design variations, operational principles, and possible applications.

1. 2. Synchronous Reluctance Machines

The SynRM is a salient pole machine with usually a three phase winding placed in the stator slots [10, 13, 14]. The rotor is made of steel laminations and is free of permanent magnets or windings. The electromechanical energy conversion in SynRMs relies on the reluctance variation in the rotor topology [7]. It is an alternative AC drive which can replace permanent magnet (PM) machines and induction machines [7, 6] in many applications such as EVs due to its simple, robust, and low-cost manufacturing. The simple structure of the rotor reduces the cost of manufacturing in comparison with PM machines and induction machines [6]. Moreover the absence of rotor windings and the rotor cage eliminates the rotor conduction loss, thus enhancing the efficiency compared to induction machines [15]. The SynRM has a fast dynamic response [6, 16], is fault tolerant [17, 18], and is capable of operating at higher speeds than various types of PM machines such as surface mounted PM machines [19]. These advantages make it a suitable choice for many applications like power generation from renewable energy resources, traction and EVs [6, 9].

1.2.1. Design Variations and Operational Principles

The torque production of the SynRM depends on the reluctance variation in the rotor topology. The reluctance variation results in the rotor tendency to align itself with the magnetic field produced by the current flowing in the stator winding which is usually a distributed three phase winding, producing a sinusoidal magneto motive force (MMF). To achieve the desired reluctance variation, the rotor design can be done in three different manners [10, 11]:

- Salient pole rotor

- Transversally laminated anisotropic rotors (TLA)

- Axially laminated anisotropic rotors (ALA)

Fig. 1-1 shows some of the design variations introduced by different authors [10]. Fig. 1-1 (a) shows a salient pole rotor structure. In order to achieve low q-axis inductance, the interpolar cut-out must be widened, however this will result in an undesirable reduction of d-axis inductance [11]. In other words although the reluctance of the q-axis flux path is considerably reduced by removing the core piece, the reluctance of the d-axis flux path is also highly affected. The small saliency ratio, and high windage losses are the main disadvantages of this design [20]. This design topology also produces a high torque ripple compared to more advanced designs (Fig. 1-1 (b) and Fig. 1-1 (c)). Fig. 1-1 (b) depicts an ALA core in which the rotor is made of steel sheets bent into a "u" shape and stacked in the radial direction [10]. This structure is theoretically appealing since it closely resembles an ideally distributed anisotropy structure [15]. However, this is only true for a two-pole machine [15]. Moreover in a usual toothed stator structure, both torque ripple and iron losses are higher [15]. ALA rotors are reported to produce saliency ratios in the range of 9 to 12 [21] but in the direct line start application, the ALA rotor produces the same value of saliency ratio as the TLA rotors [11]. The TLA rotor, shown in Fig. 1-1 (c) is a preferable design in many applications because of its simple manufacturing process and lower iron losses [9]. A TLA rotor is made of conventional steel laminations and has a multi-flux barrier design. The goal of the flux barrier introduction to the rotor design is to minimize the q-axis flux. Fig. 1-1 (d) demonstrates the position of the d-axis and q-axis of a typical 4-pole TLA rotor with three flux barriers in each rotor pole. All the above mentioned topologies aim at increasing the saliency ratio of the rotor in order to improve the performance of the SynRM.

The saliency ratio, ξ, presented in (1.1) determines almost all of the important performance parameters of the SynRM. Therefore in all design variations shown in Fig. 1-1 the main goal is to provide a low reluctance path for the d-axis flux, while minimizing the q-axis flux by increasing the reluctance of the q-axis flux path. In the process of increasing the q-axis flux path reluctance, the reluctance of the d-axis flux path is also affected. Therefore it is of great

importance to identify the most influential parameters on the q-axis path in the rotor geometry to achieve a high d-axis inductance while limiting the q-axis inductance.

(a)   (b)   (c)

(d)
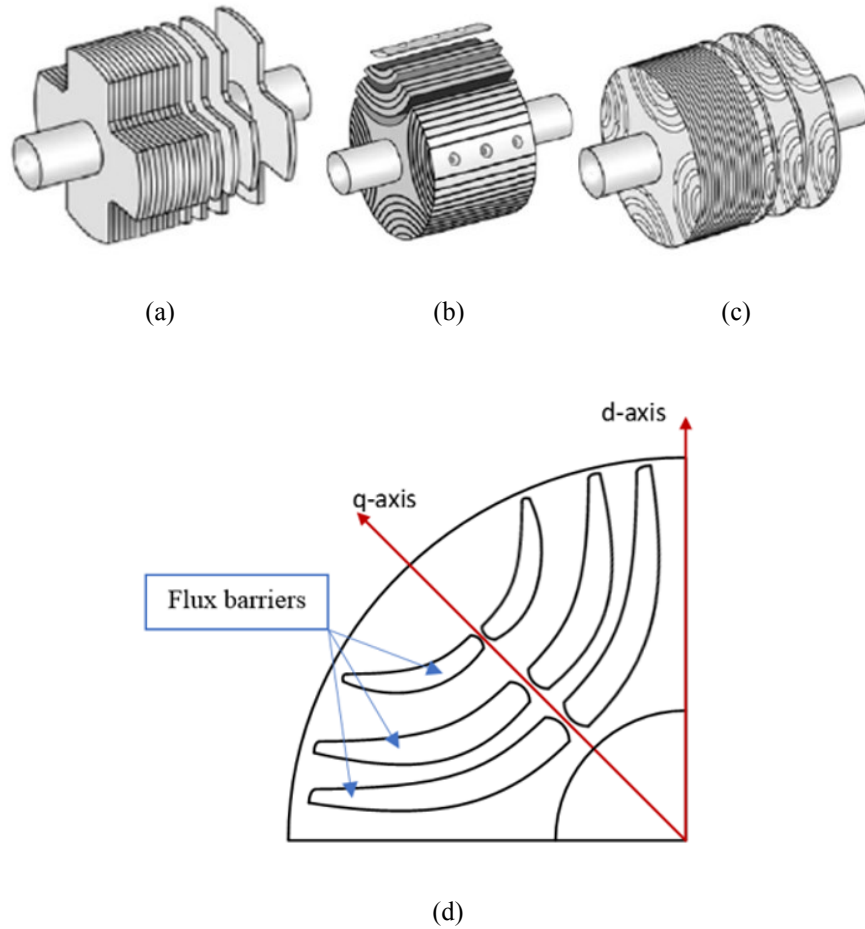
Fig. 1-1 Rotor design variations of the SynRM; (a) Salient pole rotor; (b) Axially laminated rotor; (c) Transversally laminated rotor; (d) A schematic lamination of a transversally laminated rotor

Identifying these parameters, as well as reducing the torque ripple of the SynRM are the main challenges of the SynRM design process. Equation (1.1) shows the saliency ratio of the SynRM.

$$\xi = \frac{L_d}{L_q} \tag{1.1}$$

where L_d, and L_q are the d-axis and q-axis inductances of the machine, respectively.

The *dq* model is generally used as a powerful and yet simple tool for modeling and analysis of various types of electric machines. This model has been used for SynRMs throughout the literature [10, 7, 11, 20, 22]. Equation (1.2) and equation (1.3) show the *d*-axis voltage v_d, the *q*-axis voltage v_q of the SynRM as a function of the machine's parameters and currents. The electromagnetic torque T is presented in equation (1.4) [10]:

$$v_d = R_s i_d + \frac{d\lambda_d}{dt} - \frac{P}{2}\omega_r\lambda_q \tag{1.2}$$

$$v_q = R_s i_q + \frac{d\lambda_q}{dt} + \frac{P}{2}\omega_r\lambda_d \tag{1.3}$$

$$T = \frac{3}{2}\frac{P}{2}(L_d - L_q)i_d i_q \tag{1.4}$$

where R_s, i_d, i_q, λ_d, λ_q, ω_r, and P are stator winding resistance, *d*-axis current, *q*-axis current, *d*-axis flux linkage, *q*-axis flux linkage, rotor speed (mechanical), and number of poles, respectively.

The vector diagram of the synchronous reluctance motor is shown in Fig. 1-2.
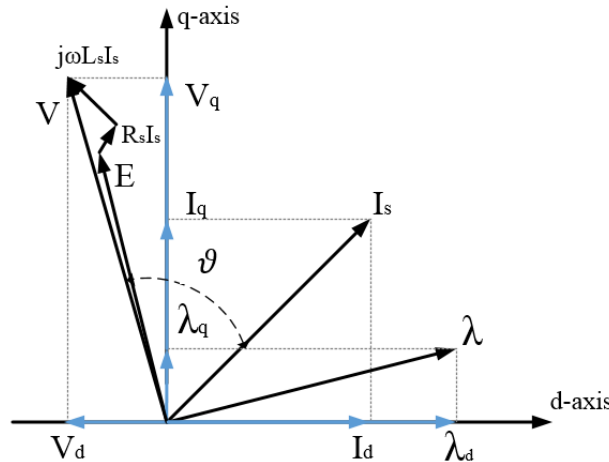
Fig. 1-2 Vector diagram of the SynRM

The absence of field excitation in SynRMs results in the necessity of providing the required magnetizing current (*d*-axis current) from the supply. Thus as is shown in Fig. 1-2 the angle between the current phasor (I_s) and the phase voltage (V), ϑ is large. Therefore the power factor

of the SynRM is relatively poor when compared to PM machines. In this diagram λ is the flux linkage of the machine and consists of the two components of d-axis and q-axis (λ_d, λ_q).

E represents the induced electromotive force (EMF) as a result of the flux linkage (λ). L_s is the phase winding inductance (shown in the single phase equivalent circuit of the SynRM in Fig. 1-3). V is the phase voltage and is equal to the phasor summation of the EMF and the voltage drop on the winding impedance. R_s and ω are the phase resistance, and the electrical speed.
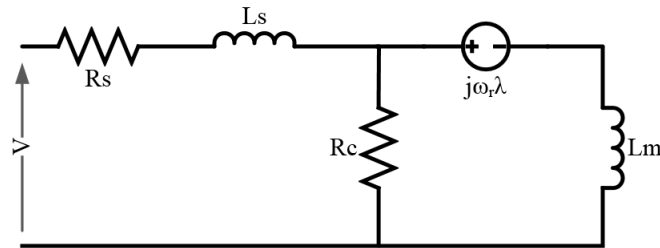
Fig. 1-3 Single phase equivalent circuit of the SynRM

Fig. 1-3 shows the single phase equivalent circuit of the SynRM [6] based on the parameters shown on the vector diagram of the SynRM. The stator core loss component is shown as R_c in this figure. Since the machine operates at synchronous speed, the magnetic field of the rotor can be considered as a DC field, which produces negligible loss. Therefore it is not mentioned in the figure. L_m is the magnetizing inductance of the machine.

Although the *dq* model has great potential for transient and steady-state modeling and analysis of the SynRM, it cannot be used as a design tool. To apply the *dq* model of the SynRM (or any other electrical machine) the phase inductances and winding resistance must be identified (see equations (1.2) to (1.4)). Thus if the machine characteristics such as winding resistance and inductance are not available, this modeling method cannot be applied. Hence to design electrical machines and in particular SynRMs, it is necessary to choose a mathematical modeling method that can provide a proper estimation of magnetic and electric features of the machine based on the desired dimensions and topology. In that regard, a mathematical modeling approach is presented in chapter 2 of this thesis which has a great potential for design, modeling and analysis of SynRMs.

1. 3. Design Approaches

The Rotor design is the main challenge of the SynRM design procedure, while the stator design is relatively straightforward. To achieve high saliency ratio values while maintaining a smooth torque waveform, the flux barriers design must be done carefully. The choice of the number of the flux barriers, their shape, and span affects the performance and torque production capability of the SynRM significantly. A literature review on the available design approaches is provided in this section.

1.3.1. Stator Design

The stator of a SynRM is usually similar to the stator of an IM or permanent magnet synchronous machines (PMSM), with a distributed winding to eliminate or mitigate the space harmonics. Although the stator is usually similar to the stator of an induction machine, the joint design of stator and rotor must also be considered since the relationship between the number of stator slots and the number of rotor flux barriers (in a TLA rotor) affects the torque waveform of the machine. To choose the number of stator slots according to the number of rotor flux barriers in a TLA rotor, guidelines are provided in the literature [22]. However since the main goal of the stator design in a SynRM is to provide a smooth air gap MMF, the choice of the number of stator slots is done in a manner to generate a proper sinusoidal MMF. Hence the number of the rotor flux barriers is chosen accordingly.

1.3.2. Rotor Design

As stated earlier in this section, the rotor design is the most challenging part of the SynRM design. Over the past four decades several methods are addressed in the literature for design modification, and performance improvement of SynRMs. These methods can be categorized into two main groups:

- Numerical methods- Based on Finite Element Analysis (FEA), and evolutionary algorithms for design optimization
- Analytical methods- Based on the electromagnetic equations of the system

The analytical design is usually followed by a FEA simulation to ensure achieving the application's requirements. FEA can also be used as a powerful design tool and it has been used directly for design of various types of electrical machines including SynRMs [23], [24].

Although FEA software is capable of providing accurate results when compared to measurement results, initiating a design approach based on a FEA simulation might not always result in the best outcome. Electrical machines in general, and the SynRMs in particular possess numerous geometric, magnetic, electric, and thermal features. For example the torque, T produced by any electrical machine is directly proportional to its stack length, l_{stack}, times the rotor outer diameter, D squared as shown:

$$T = Kl_{stack}D^2 \tag{1.5}$$

where K is a constant which depends on the magnetic loading, electric loading, and number of poles. To achieve the desired torque value the outer diameter of the rotor and its stack length can be chosen to satisfy equation (1.5). However due to the magnetic, electric, thermal, and mechanical restrictions, not any two values can be used for the stack length, and rotor outer diameter. In any electrical machine there is a large number of parameters that must be evaluated before FEA simulation. Therefore although FEA is capable of providing an accurate calculation and prediction of the machine's performance, it cannot be used as a design tool to decide the machine's parameters.

The FEA design, as stated earlier, depends on a set of parameters which must be decided by the designer and refined through trial and error. In order to fully utilize the capabilities of FEA software, the main geometric, magnetic, and electric features of the SynRM (or in general any electric machine) must be decided beforehand. Once the main geometrical parameters; that is, the rotor outer diameter, and the stack length of the machine; and the main electromagnetic parameters of the machine; that is, the electric loading and the magnetic loading, and the number of poles are decided, the output power of the machine can be calculated. However the output power, torque, and the base speed of the machine are chosen based on the application requirements. Therefore the electromagnetic and geometrical characteristics of the machine must be adjusted in a manner to meet the desired application requirements. For SynRM design, the large number of geometrical parameters in the rotor, such as number, shape, location, and widths of the flux barriers, makes the design procedure more complicated when compared to other rotor topologies. Some of these geometrical parameters are shown in Fig. 1-4. The radial rib thickness has a direct impact on the q-axis flux inductance. Therefore a large radial rib

thickness results in a high q-axis inductance, resulting in a low saliency ratio value. However a small rib thickness reduces the mechanical strength of the lamination. The same constraint also applies to the tangential rib thickness value. The width of the flux barrier influences both the d-axis and the q-axis inductances. However it is not possible to draw a general conclusion on the desired width of the flux barriers, since although a large flux barrier width can reduce the q-axis inductance, it can also result in the saturation of the lamination and the consequent reduction of the d-axis inductance. The rotor slot pitch affects the torque waveform, and the torque ripple of the SynRM [6]. Thus it must be designed carefully as stated in [5].
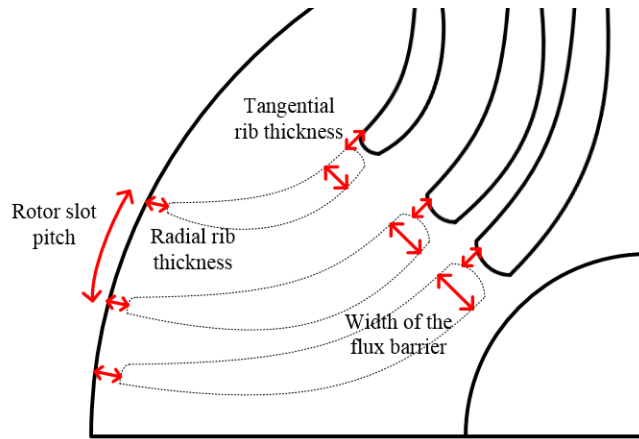
Fig. 1-4 Geometrical parameters of the rotor of a SynRM

Since the performance of a SynRM is highly affected by its rotor design, several guidelines are proposed in the literature to be used as initial design tools [17, 22]. As an example the number of rotor flux barriers can be chosen as a function of the number of stator slots as stated in [25], so that the torque ripple of the machine remains in an acceptable range. Such guidelines however only provide a limited number of initial design parameters, and are not capable of estimating the output characteristics of the machine. In [22] design criteria of SynRMs which enhance the output torque, by increasing the saliency ratio through analytical calculations are presented. In the proposed analytical approach the ratio between the d-axis and the q-axis inductances are calculated, and the most influential geometrical parameters are identified. It is shown that the width of the flux barriers of the rotor, is an influential parameter that defines the value of the q-axis inductance and thereby the saliency ratio of the machine. However for a complete design procedure the relative value of the d-axis and q-axis inductances of the machine is not sufficient. Using the proposed technique in [22] the torque waveform and other

characteristics of the machine cannot be calculated. That reveals the necessity of having an analytical design, and modeling method which can provide initial insight into the electrical machine. The modeling method must be capable of taking the effect of most of the geometric, electric, and magnetic parameters into account. Various analytical models are proposed in the literature which are used for design modification or characterization of electrical machines [26]. Analytical approaches are relatively fast and easy to implement. They can be used both as a design tool and as a modeling method. In a proper analytical model, the model accuracy is adjustable according to the application requirements and the available modeling resources and software. Some of these methods which are proposed and used for SynRMs are briefly discussed here.

An analytical model which can determine the proper position for the flux barriers of a TLA SynRM is proposed in [27]. The aim of the proposed model is to minimize the torque ripple of the machine. The model is developed initially for a SynRM with one flux barrier and then extended to practical rotor topologies with more than one flux barrier. The proposed model in [27] is initially introduced in [17] and is developed to compensate the torque harmonics in SynRMs. In this modeling approach the electric loading of the stator winding is expressed using the Fourier series. Based on the obtained electric loading, the stator magnetic potential along the stator periphery is calculated. Finally the magnetic flux density in the air gap is calculated using the magnetic potential values of the stator and rotor. The magnetic flux density value in the air gap is later used to calculate the electromagnetic torque based on the Lorentz force equation. However the procedure to obtain the magnetic vector potential values in the rotor is not simple, and not discussed in the paper in detail. Moreover in order to calculate the magnetic potential value in each rotor section, the rotor geometry and dimensions, and the electric loading produced by the stator winding must be available. Therefore since these parameters are not available in initial design steps, the application of this method is difficult and requires several steps of calculations to achieve a proper design topology. A similar approach is used in [28]. Using FEA the analytical model is verified and optimized. In [13], the inductances and the torque of an axially laminated SynRM are calculated using winding function theory. In this model an air gap function which is defined based on the rotor topology, and a winding function which is defined according to the winding distribution of the machine are used to calculate the inductances of the phases and eventually the electromagnetic torque

of the machine. However in the proposed method, the equation which is used to estimate the effect of the flux barriers is only applicable to ALA rotors and cannot be used for TLA rotor designs. A semi numerical method is presented in [29]. In this model the Maxwell Stress Tensor is used to calculate the harmonic torque components in a fractional slot concentrated winding SynRM. A multiple coupled circuit model of SynRMs is presented in [30]. The proposed method is derived based on the magnetic circuit (MEC) model. Although the accuracy of the results obtained from the MEC modeling approach is relatively higher than other modeling methods, it is time consuming to implement the model, and once the model is completed, it is not easy to vary the design parameters. Therefore this analytical approach is more suitable for modeling and analysis of an existing machine, and cannot be used as a flexible design tool.

The design procedure of the rotor structure can be started by defining a basic rotor structure as shown in [31]. In this approach the number of flux barriers, eventual cutoffs, etc. are initially chosen. Then barrier widths, rib widths, and their placement are optimized numerically. The advantage of this procedure is that the magnetic cross saturation and other complex phenomena are taken into account in the numeric optimization process using finite element software [15]. On the other hand the results may depend on the preliminary choices of the initial rotor structure. Thus the initially chosen number of flux barriers can significantly affect the performance, torque ripple, and torque density.

Another approach is based on the generalized lumped-parameter modeling of the rotor magnetic circuit [15, 22]. In this model a purely sinusoidal MMF is considered, thus only a rough approximation of the real system is obtained. Moreover only the d-axis saturation is taken into account [15] and the cross saturation effect is neglected. In this method, in order to minimize the q–axis flowthrough flux, the permeance of the various flux barriers are considered to be related to each other. It has been shown that for four-pole machines, this minimum-inductance distribution of permeance practically coincides with a constant-permeance distribution [15]. [32] uses FEA to study the effect of several combined configurations of star-delta connected winding on the output torque and efficiency of SynRMs through FEA simulations and experiments.

1.3.3. Problem Statement and Methodology

The complicated rotor topology of the TLA SynRM reveals the necessity of using an analytical design method prior to FEA simulation. However the analytical modeling method must have some level of flexibility for design parameter variations. In that regard, methods such as Magnetic Equivalent Circuit (MEC) which are developed based on a discretization of the machine's topology are not suitable for SynRMs because the variation of the parameters in MEC modeling is not easy to perform. Some of the methods mentioned earlier [17], also require design parameters to begin with the initial calculations.

To overcome the design challenges and obtain a SynRM which is capable of providing the application requirements, a proper understanding of the machine's features and characteristics is a necessity. It is also important to improve the machine's saliency ratio in order to increase the output torque, enhance the power factor, and improve the efficiency of the SynRM.

Performance improvement can also be achieved using design variations of the SynRM with permanent magnet materials, called permanent magnet assisted SynRMs (PM assisted SynRMs). Analytical modeling and design approaches can also be useful to better understand the characteristics of such design variations of SynRM. Although several topologies of PM assisted SynRM are presented in the literature, the absence of proper analytical design approaches and the possibility of design improvement reveals the necessity of further research and study in this field.

While the performance of a PM assisted SynRM can be improved through d-axis flux enhancement, the existing design topologies in the literature usually operate based on limiting the q-axis flux using permanent magnet materials. In this research the possibility of performance improvement in PM assisted SynRMs, using a different topology is investigated. The proposed topology provides a PM assisted SynRM with a relatively high saliency ratio, and benefits from the additional permanent magnets to obtain a higher power factor. In this design configuration, the permanent magnets are placed in a manner to enhance the d-axis flux of the machine.

The proposed analytical model of the SynRM is presented in Chapter 2 of this thesis. Later in Chapter 3 a modified version of the analytical model is used to design a PM assisted SynRM.

1. 4. Generator Operation of Synchronous Reluctance Machines

1.4.1. Synchronous Reluctance Generators

Generator operation of the SynRM as a robust [33], simple, and comparatively less expensive generator dates back to 1990s. Since then, different aspects of the generator operation of the SynRM have been discussed in the literature, like performance [34, 35, 36], operating limits [37, 38] and control strategies [39, 40, 41, 42]. The absence of field excitation as in conventional synchronous machines or permanent magnet machines results in operational challenges for electric power generation of the SynRM. In that regard, the SynRM can be operated as a stand-alone power generation unit, or as a grid-connected generator. In grid-connected mode the required magnetizing current is provided by the grid, while the SynRG supplies active power to the grid. In stand-alone operation the required magnetizing current (the required reactive power of the SynRG) is provided by a properly sized capacitor bank. This capacitor bank can also be sized in a manner to provide the reactive power demand of the load. The start-up procedure of the SynRG as a stand-alone power generation unit requires careful consideration of the SynRM's characteristics and maintaining certain initial conditions in the system. In that regard, the generator operation of the SynRM as a stand-alone unit is similar to that of a stand-alone induction generator [43].

Although various aspects of the SynRG operation are addressed in several research works, the start-up procedure of the stand-alone SynRG and the required criteria to ensure a successful voltage build-up are not discussed to this date. The build-up procedure of the terminal voltage in SynRMs and induction machines in stand-alone generator operation is called self-excitation, and it depends on the nonlinear characteristic of the ferromagnetic core material [39], presence of the initial condition (capacitor initial voltage or residual flux in the core) in the system [43], a properly sized capacitor bank, and maintaining a minimum speed. The self-excitation phenomenon in stand-alone induction generators is discussed in [44, 45, 46]. However this phenomenon in SynRMs has not been fully investigated. Most of the available research on SynRGs as presented earlier, focus on the output characteristics of the SynRG. As an example in [47] it is shown that the steady-state performance of the SynRG is significantly affected by the air gap flux linkage and core saturation. Control strategies of the SynRG such as operation of the SynRG in an extended speed range while decreasing the conduction loss are discussed in

[34]. [42] presents voltage control for a super high-speed SynRG system with a pulse width modulation (PWM) voltage source converter. Studies of SynRG performance at different loading conditions, obtaining the efficiency and power factor of the machine, and identifying the maximum power-conversion capability of the SynRG are presented in [48]. However none of these research works consider the criteria for self-excitation of the SynRM in stand-alone operation.

1.4.2. Problem Statement and Methodology

Although numerous studies present the stand-alone operation of the SynRG in steady state condition, the build-up procedure of the terminal voltage has been neglected. The self-excitation phenomenon in induction generators are discussed in [44], [43]. However the self-excitation of the SynRG is not presented in any research work. The start-up procedure of a SynRM in stand-alone generation mode, requires maintaining certain criteria. A section of this thesis is dedicated to the self-excitation in SynRGs and the required criteria to ensure a successful voltage build-up. The *dq* model of the SynRG is used in simulations and the modeling results are validated by numerous experiments performed on a stand-alone SynRM connected in parallel to a capacitor bank. This study is presented in detail in chapter 4 of the thesis.

1. 5.   Objectives

The main objective of this research work is to generate analytical models for the design, analysis and characterization of SynRMs and permanent magnet assisted SynRMs. The proposed analytical model is developed in a manner to take the main geometric, and electromagnetic properties of the machine into account while maintaining a flexible analysis platform which enables it to be used as a design tool. Therefore the design parameters can be varied with minimum effort and their impact on the output performance of the machine can be studied. This flexibility enables the designer to achieve the desired performance of the specific application in a relatively short time with a proper accuracy.

The proposed analytical model is initially used to characterize a previously prototyped SynRM. The model is validated using experimental results and FEA simulation results. Later the model is modified for PM assisted SynRMs. Using the modified analytical model, a PM assisted SynRM rotor is designed, based on the stator dimensions of the existing SynRM.

Therefore the rotor outer diameter and stack length are similar to the rotor of the SynRM. The design objective is to obtain a PM assisted SynRM with improved torque density and power factor when compared to the existing SynRM. The permanent magnet material used in the PM assisted SynRM is AlNiCo 9 magnet which results in low manufacturing cost (compared to rare-earth magnets). However the magnetic features of AlNiCo magnets (low coercivity) has to be considered in the design procedure to avoid unwanted demagnetization of the permanent magnets. The analytical model is also modified for analysis and characterization of another design topology of the SynRM using Cold Rolled Grain Oriented (CRGO) steel in which the superior magnetic characteristics of the CRGO steel is used for saliency ratio improvement of the SynRM.

The study of the generator operation of the stand-alone SynRM and the required criteria to ensure a successful voltage build-up is another part of this research work. The objective of this study is to identify the self-excitation criteria of the stand-alone SynRG. Using the *dq* model of the SynRG, the minimum residual magnetism, and the maximum start-up acceleration to ensure a successful self-excitation are calculated based on the machine's characteristics and the size of the capacitor bank. Later the obtained criteria are verified by experimental results.

1. 6. Contributions

The research contributions of the work can be summarized as:

- Developing an analytical model for design, analysis, and characterization of SynRMs and PM assisted SynRMs.
- Designing and prototyping a PM assisted SynRM rotor using low cost AlNiCo magnets based on the stator dimensions of the previously prototyped SynRM.
- Self-excitation criteria of the stand-alone SynRG.

Journal papers:

- S. Maroufian, and P. Pillay, "Self-Excitation Criteria of the Synchronous Reluctance Generator in Stand-Alone Mode of Operation," IEEE transaction on Industry Applications, Year: 2018, Volume: 54, Issue: 2, Pages: 1245-1253

- S. Maroufian, and P. Pillay, "Torque Characterization of a Synchronous Reluctance Machine Using an Analytical Mode," IEEE Transaction on Transportation Electrification, Year: 2018, Volume: 4, Issue: 2, Pages: 506-516

Conference papers:
- S. Maroufian, and P. Pillay, "Analytical Modeling of a Segmented-Pole Synchronous Reluctance Machine with CRGO Laminations" in IEEE Energy Conversion Congress and Exposition (ECCE 2018), Portland, Oregon

- S. Maroufian and P. Pillay, PM Assisted Synchronous Reluctance Machine Design Using AlNiCo Magnets" , in IEEE International Electric Machines and Drives Conference (IEMDC 2017), Miami, FL, USA

- S. Maroufian and P. Pillay, "Self-Excitation Criteria of the Synchronous Reluctance Generator in Stand-Alone Mode of Operation," in IEEE International Conference On Power Electronics, Drives And Energy Systems (PEDES 2016), Trivandrum, India

- S. Maroufian, and P. Pillay, "Torque Characterization of a Synchronous Reluctance Machine Using an Analytical Model," in IEEE International Conference On Power Electronics, Drives And Energy Systems (PEDES 2016), Trivandrum, India

1. 7.   Organization of this Thesis

Chapter 2 presents the analytical modeling and design approach which is used for analysis of a previously designed and prototyped SynRM. The results of the analytical model are compared with the results obtained from FEA and measurements.

Chapter 3 starts with introducing the PM assisted SynRM. In this chapter the analytical model presented in chapter 2 for analysis and modeling of the SynRM is modified and used to obtain initial design parameters of the PM assisted SynRM. The PM assisted SynRM designed in this chapter benefits from low cost AlNiCo magnets.

Chapter 4 presents the stand-alone operation of the synchronous reluctance generator (SynRG) using a properly sized capacitor bank.

Chapter 5 provides the conclusion and the possible future work of the thesis.

Chapter 2   Analytical Modeling of Synchronous Reluctance Machines

2.1. Introduction

The large number of geometrical parameters in the rotor of the SynRM results in design complexities. The width, and the number of the flux barriers in a TLA, as well as their respective shapes, can vary over a wide range resulting in considerable differences in the output torque and performance of the machine. Thus to obtain the desired output characteristics regarding the application requirements, the design parameters must be chosen carefully, and precisely. To overcome the design challenges of SynRMs, several guidelines are suggested in the literature. These guidelines such as the choice of the number of the flux barriers to minimize the torque ripple production presented in [25], can be used as initial design estimations. However such estimations can only provide a limited number of design parameters, and will not provide the output characteristics of the machine.

In order to provide a reliable approach to design the SynRM regarding the application requirements, the machine's characteristics must be assessed as a function of different design parameters. Thus a mathematical model for design and analysis of the SynRM is a convenient tool to guide the design procedure. This approach expends less resources during the design phase, while increasing the chances of successful prototyping. In the literature, several methods are described to model the behavior of electric machines, each presenting positive aspects and drawbacks. Basically, the modeling methodologies can be divided into two main categories: Analytical methods, which are based on abstractions of the machines elements, and numerical methods, which describe the behavior of the fields inside of the machine. The following section presents the most common design methods for electric machines briefly. The modeling approach which is used for analysis and characterization of a previously prototyped SynRM is presented in details. The model is verified using FEA and measurements and the results are presented in this chapter. Later in Chapter 3 the proposed model is modified in a manner to be used for designing a PM assisted SynRM.

2.2. Literature Review of the Available Analytical Methods

Three of the main analytical approaches for modeling and analysis of electrical machines are:

- Lumped parameters method
- Magnetic Equivalent Circuit (MEC) method
- Winding function method

Electrical equivalent circuit models are derived using classical field analysis [49] and are widely used to describe the behavior of synchronous machines and induction machines. This simple model has the capability to calculate the per phase voltage, current, output power, torque average value and losses of the machine. The equivalent circuit models of electrical machines are useful tools to obtain an estimation of the machine's behavior in steady-state condition. The *dq* model of electrical machines is also considered a lumped parameter model and as discussed in the previous chapter is widely used for the analysis of SynRMs. The *dq* model is used for modeling generator operation of the SynRM in this thesis (Chapter 4).

In the MEC model, the machine's structure is divided into several elements [50, 51]. The elements are characterized by their reluctance which is a function of the material properties and the machine's geometry. Solving the obtained equivalent circuit, the magnetic potential values of the nodes connecting the elements at different magnetic potential levels, are obtained. The electromagnetic torque is then calculated using the Maxwell Stress Tensor or other methods. The main advantage of the MEC is the trade-off between the desired accuracy and the complexity of the model. However, the inflexibility of the method brings challenges to the use of MEC as a design tool, since applying design variations in the model is relatively difficult once the model is generated.

The winding function method is a mathematical approach for modeling electrical machines based on the estimation of the winding inductance. This model is used in this thesis for modeling and characterization of a prototyped SynRM and later expanded to a design tool for designing a PM assisted SynRM. The analytical design is followed by a FEA simulation prior to prototyping.

FEA is a numerical approach to describe the behavior of the magnetic fields inside the machine. This method is usually used in the analysis of electrical machines due to its capability in providing accurate results. This method can be used as a design tool for electric machines, however the FEA design depends on a set of parameters which must be estimated by the designer and refined through trial and error, rendering the process, time consuming.

To design SynRMs, both analytical and numerical methods have been applied in the literature. [22] presents a design criteria of SynRMs to enhance the output torque by increasing the saliency ratio through analytical calculations. However the proposed analytical approach only provides the ratio between the two main inductances of the machine, that is the d-axis and the q-axis inductances. Thus the torque waveform and other characteristics of the machine cannot be calculated. In [13] the inductances and the torque of an ALA SynRM are calculated using winding function theory. The referred paper presents an air gap function. However the proposed equation to estimate the effect of the flux barriers is only applicable to ALA rotors. In [29], a semi numerical method based on Maxwell Stress Tensor is presented to calculate the harmonic torque components in a fractional slot concentrated winding SynRM. In [30], a multiple coupled circuit modeling of SynRMs is presented. The proposed method is derived based on the magnetic circuit model. In [52] the MEC modeling method is used to calculate the open circuit characteristic of a PM assisted SynRM; that is the back-EMF. Later based on the derived model, the torque pulsation of the machine is estimated and compared with FEA simulation result. Using this model the air gap flux density and its radial and tangential components are calculated. However as mentioned earlier the main challenge of the MEC modeling method is its complexity and lack of flexibility for design variations. Thus for each new design topology that the designer aims for, a new magnetic circuit must be developed, which is time consuming. Therefore although this method provides an accurate result as shown in [52], it cannot be considered as a flexible design tool.

In this research, the winding function method [53] is applied to model the behavior of the SynRM. This method which has been used by many researchers [54], [55], [13], [56] relies on the MMF calculation based on the winding configuration, and the definition of an air gap function based on the machine's geometry. The winding function permits the parameters to be changed easily, which is an important characteristic for an analytical method to be used as a design tool. The main contribution in application of the winding function for design and

characterization of SynRMs is proposing a mathematical approach to include the effect of the flux barriers in the air gap function determination of the TLA SynRM. The obtained results of the winding function model are also extended from inductance calculation to torque-angle curves and torque waveform estimations of the SynRM using the coenergy method and the Maxwell stress tensor method, respectively.

All the available modeling approaches based on the winding function method presented by various authors [54], [55], are mainly limited to the calculation of the inductances and analyzing the inductance curve for fault detection or parameter estimation [14, 57]. For example [54] uses the inductances calculated using the winding function method for analysis of the air gap eccentricity in a salient pole synchronous machine. By comparing the shape of the inductance curves for healthy and unhealthy machines and analyzing the spatial harmonics, the faulty condition is detected. [55] uses the winding function approach to obtain a generalized closed-form equation for the inductances of surface mounted PM machines and induction machines. The same approach is followed in [13] for inductance estimation of axially laminated synchronous reluctance machines. However the model is not far extended beyond inductance calculation. In this thesis the winding function method is established based on the topology of a previously prototyped transversally laminated synchronous reluctance machine. Initially the model is used to calculate the inductance matrix of the machine, and later extended for characterization and torque waveform calculation.

The analytical model presented in this research can be used for both characterization, and design of TLA SynRMs. Using the proposed approach as a characterization method provides an opportunity to obtain an estimation of the machine's performance without having to do the time consuming procedure of measurement. The capability of the model as a design tool helps to improve the design prior to FEA simulation, and prototyping. Therefore the effect of various design parameters on the performance of the SynRM can be examined. The winding function method is initially presented in the following section, then followed by the application of the model on a previously designed and prototyped SynRM. The results are then compared with the FEA and measurement results. The comparison shows an acceptable agreement thus proving the validity of the method.

The verified model of the SynRM is later modified to be used for characterization and design of variations of SynRMs such as PM assisted SynRMs, and a segmented-pole SynRM made with CRGO steels.

2.3. Winding Function Method

2.3.1. Basic Formulation

All conventional machines rely upon the MMF produced by the current flowing in the winding placed in the stator slots to perform the electromechanical energy conversion process. Therefore one approach to model and analyze the machine would be the direct analysis of the winding configuration and the air gap MMF produced by the current flow. Consider a concentrated single phase winding as shown in Fig. 2-1. In this figure only one side of the coil is depicted.

According to the geometry shown in Fig. 2-1 one can write the Ampere's Law for the path 12341, as:

$$\oint_{12341} H.dl = \int_S J.dS \qquad (2.1)$$

where H, and J are the magnetic field intensity, and the current density, respectively. S represents the surface enclosed by the depicted path.
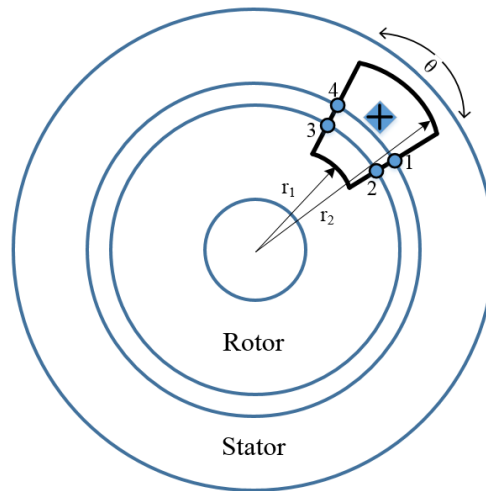
Fig. 2-1. Electrical machine schematic

Since all the current on the surface is concentrated in the winding, (2.1) can be rewritten as:

$$\oint_{12341} H.dl = n(\theta)i \qquad (2.2)$$

where $n(\theta)$ expresses the number of turns enclosed by the path, and is usually named as turns function [53], and i is the current. θ shows the rotor angle. The left hand side of (2.2) can also be expressed in terms of MMFs.

$$\mathcal{F}_{12} + \mathcal{F}_{23} + \mathcal{F}_{34} + \mathcal{F}_{41} = n(\theta)i \qquad (2.3)$$

Neglecting the MMF drop in the ferromagnetic core parts (rotor, $\mathcal{F}_{23}$ and stator, $\mathcal{F}_{41}$), and considering the path from 1 to 2 at zero angle, (2.3) can be written as:

$$\mathcal{F}_{12}(0) + \mathcal{F}_{34}(\theta) = n(\theta)i \qquad (2.4)$$

$\mathcal{F}_{12}$ and $\mathcal{F}_{34}$ show the MMF drop in the air gap at zero and θ degrees.

$\mathcal{F}_{12}(0)$ and $\mathcal{F}_{34}(\theta)$ are expressed as:

$$\mathcal{F}_{12}(0) = -H_r(r,0)g \qquad (2.5)$$

$$\mathcal{F}_{34}(\theta) = H_r(r,\theta)g \qquad (2.6)$$

H_r represents the magnetic field intensity in the air gap at a specific angle and r shows the radius at the air gap, and g is the air gap function.

Using Gauss' Theorem and after some mathematical calculations the MMF from 1 to 2, $\mathcal{F}_{12}(0)$ is obtained:

$$\mathcal{F}_{12}(0) = i\left[\frac{1}{2}\int_0^{2\pi} n(\theta)d\theta\right] \qquad (2.7)$$

The part shown in brackets in (2.7) is the average value of the turns function $n(\theta)$, introduced previously (equation (2.2)).

$$\langle n \rangle = \frac{1}{2}\int_0^{2\pi} n(\theta)d\theta \qquad (2.8)$$

Then according to (2.6), $\mathcal{F}_{34}(\theta)$ can be calculated as:

$$\mathcal{F}_{34}(\theta) = (n(\theta) - \langle n \rangle)i \tag{2.9}$$

The term shown on the right hand side of (2.9) $(n(\theta) - \langle n \rangle)$, is the turns function without its average value, and is usually referred to as the Winding Function, and is defined in (2.10):

$$N(\theta) = n(\theta) - \langle n \rangle \tag{2.10}$$

Therefore the MMF at any point along the air gap can be written as the winding function times the current.

$$\mathcal{F}(\theta) = N(\theta)i \tag{2.11}$$

Once the winding function of the machine is identified, the mutual and phase inductances can be calculated in the following manner.

The magnetic flux in the air gap is related to the air gap MMF according to (2.12).

$$\varphi = \mathcal{F}/\mathcal{R} \tag{2.12}$$

where φ, and $\mathcal{R}$ are the air gap flux and the magnetic reluctance of the air gap. (2.12) can be written for a differential element with the length g, and the cross sectional area of $(rd\theta)$.

$$d\varphi = \mathcal{F}_A(\theta)\frac{\mu_0 r l_{stack} d\theta}{g} \tag{2.13}$$

where $\mathcal{F}_A$ is the MMF due to the phase A winding, and μ_0 is the permeability of the free space. l_{stack}, r, and g are the stack length, radius at the air gap, and the air gap function, respectively.

After some mathematical calculations, the flux linkage of winding B due to the current in phase A is obtained using (2.14):

$$\lambda_{AB} = \frac{\mu_0 r l_{stack}}{g} \int_0^{2\pi} n_B(\theta) \, \mathcal{F}_A(\theta) d\theta \tag{2.14}$$

Where $n_B(\theta)$ is the winding turns of the winding B, and is defined as:

$$n_B(\theta) = N_B(\theta) + < n_B > \tag{2.15}$$

Where $N_B(\theta)$ is the winding function of the phase B.

The mutual inductance between phase A and phase B can be defined as the flux linkage of winding B divided by the current in the winding A. Therefore the mutual inductance between phase A and phase B can be expressed as:

$$L_{BA} = \frac{\mu_0 r l_{stack}}{g} \int_0^{2\pi} N_B(\theta) \, N_A(\theta) d\theta + \frac{\mu_0 r l_{stack}}{g} \int_0^{2\pi} <n_B> N_A(\theta) d\theta \qquad (2.16)$$

The winding function for any winding is a symmetrical function with zero average value. Thus the second term in the right hand side part of (2.16) is equal to zero. Therefore the mutual inductance between phase A and phase B can be written as:

$$L_{BA} = \frac{\mu_0 r l_{stack}}{g} \int_0^{2\pi} N_B(\theta) \, N_A(\theta) d\theta \qquad (2.17)$$

where $N_B(\theta)$, and $N_A(\theta)$ are the winding functions of phase B and phase A.

Using the same approach the self-inductance of the phases are also obtainable. Hence the self-inductance of phase A is expressed as:

$$L_{AA} = \frac{\mu_0 r l_{stack}}{g} \int_0^{2\pi} N_A(\theta) \, N_A(\theta) d\theta \qquad (2.18)$$

Once the inductances of the machine are obtained, the electromagnetic torque, T can be calculated using the coenergy method:

$$T = \frac{1}{2} [I]^T \left[\frac{\partial L(\theta)}{\partial \theta} \right] [I] \qquad (2.19)$$

where $[I]$ is the current vector, which for a three phase machine consists of the currents of the three phases, and $\partial L / \partial \theta$ is the derivative of the inductance matrix according to the rotor angle, θ. Therefore the electromagnetic torque at each rotor angle is calculated for different current magnitudes.

2.3.2. Winding Function of the SynRM

For the SynRM which is studied in this research, first the winding configuration is obtained in detail. Table. 2-1 shows the winding information of the SynRM and some of the other important parameters.

Table. 2-1. Machine parameters

Parameter	Value
Winding type	distributed
Coil pitch	9
Rated current	20 A
Number of stator slots	36
Number of poles	4
Number of winding turns	25
Rotor outer diameter	134.2 mm
Stack length	200 mm
Air gap length	0.4 mm
Base speed	850 rpm
Stator outer diameter	204.8 mm

Fig. 2-2 shows the winding configuration of the SynRM for one pole, and the corresponding turns function.

As mentioned earlier in this section, the winding function for any winding configuration is the turns function minus its average value. For the studied SynRM the winding function is obtained as shown in Fig. 2-2.
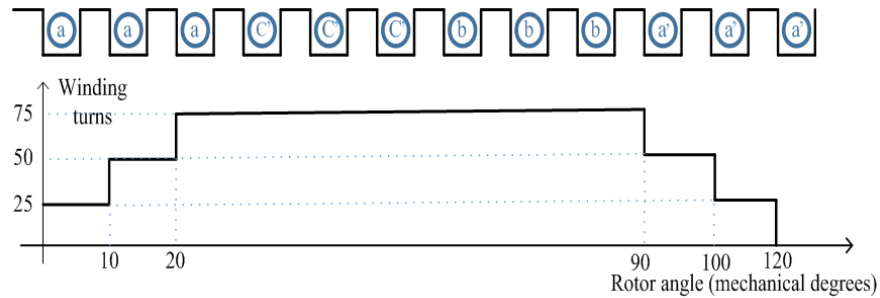
Fig. 2-2. Per pole winding configuration of the SynRM

For a three phase machine the winding function of each phase is similar in shape and magnitude, but displaced 120 degrees from one another. The obtained winding function is then used to calculate the air gap MMF according to (2.12). Note that for a three phase balanced system the resultant air gap MMF forms a sinusoidal waveform which rotates in the air gap at synchronous speed.
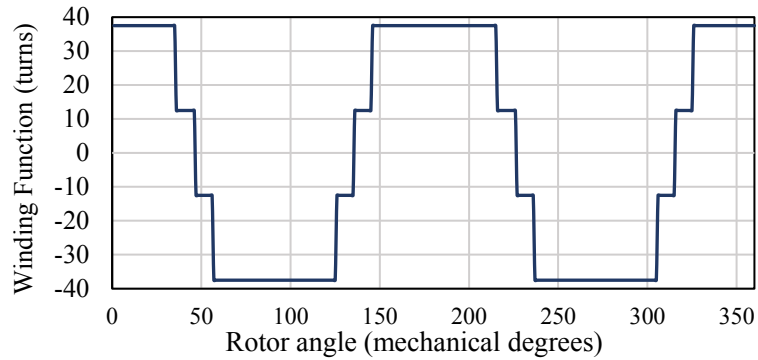
Fig. 2-3 Winding function of the SynRM

Fig. 2-4 Shows the air gap MMF at an instant of time.
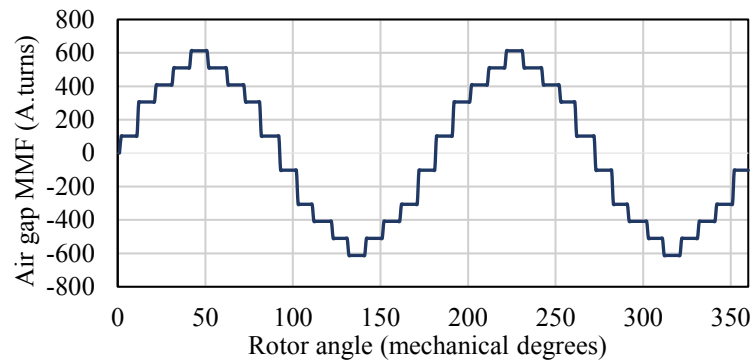
Fig. 2-4 Air gap MMF of the SynRM

2.3.3. Air Gap Function of the SynRM

The inductances of the machine calculated using (2.17) and (2.18) are highly dependent on the air gap function of the machine, g. For a typical machine like a PMSM or IM the air gap function, is equal to the physical air gap length, and is a constant value along the rotor outer diameter. However in a SynRM, though the physical air gap is uniform, the presence of the flux barriers in the rotor structure, form a variable magnetic property along the air gap periphery which changes from a minimum value in the d-axis to a maximum value along the q-axis. This section briefly introduces the methods presented in the literature to estimate the air gap function, which is suitable for ALA rotors. The proposed method in this thesis which is based on a TLA rotor design is later discussed and the results are provided.

28

The air gap function depends on the rotor geometry, and can be modeled based on the geometrical parameters of the rotor, such as pole arc to pole pitch ratio. In [13], the air gap is modeled by Fourier series as:

$$g(\varphi, \theta_r) = K_c g_1 + \beta K_c (g_2 - g_1)$$
$$+ \frac{2}{\pi} \sum_{n=1}^{\infty} \frac{1}{n} K_c (g_2 - g_1) \times sin(n\beta\pi) \times cos(Pn(\varphi - \theta_r)) \quad (2.20)$$

where K_c, g_2, g_1, β, P, φ, and θ_r are the Carter's coefficient, air gap length at q-axis, air gap length along the d-axis, pole arc to pole pitch ratio, number of poles, stator angle, and the rotor angular position, respectively.

An analytical expression for the air gap function of an ALA rotor is provided in [21, 58], which defines this function for the d-axis and the q-axis separately. Thus it cannot be used for the purpose of the winding function method. Since in this approach the air gap function must be identified for all rotor angles from 0 to 360 degrees. In [59] an air gap function for ALA rotors is proposed as:

$$g(\theta_r)$$

$$= \begin{cases} K_c g_1 & 0 \le \theta_r \le \frac{1}{2}\beta\pi \\ K_c g_1 + R(cos(\theta_r) - cos(\theta_i)) + \left(\frac{1}{2}\pi - \psi\right)(sin(\theta_i) - sin(\theta_r)) & \frac{1}{2}\beta\pi \le \theta_r \le \left(1 - \frac{1}{2}\beta\right)\pi \\ K_c g_1 & \left(1 - \frac{1}{2}\beta\right)\pi \le \theta_r \le \pi \end{cases} \quad (2.21)$$

The parameters in (2.21) are shown in Fig. 2-5. All the above mentioned methods to calculate the air gap function are designed based on the ALA rotor geometry and cannot be applied to TLA rotors.
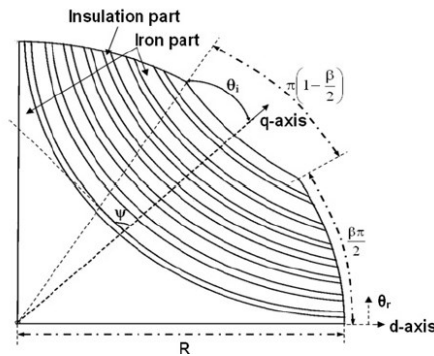
Fig. 2-5 ALA rotor and geometrical parameters [27]

To identify the effect of the rotor flux barriers on the air gap function of a TLA rotor, a mathematical procedure is proposed in this thesis. In this method the impact of individual flux barriers on the air gap function of the SynRM is modeled as an additional air gap length. The following presents the analytical approach to obtain the air gap function of the 7.5 hp SynRM presented earlier in this chapter. The results obtained from this modeling method can be used for design modifications of the SynRM. The proposed analytical model can also be modified for design and analysis of other variations of SynRMs, such as permanent magnet assisted SynRMs, and segmented pole SynRMs made of CRGO steel laminations [60].

The modeling process begins with estimating the shape of the flux barriers. The analyzed SynRM has semi-circular flux barriers, however for ease of modeling the flux barriers are assumed to be completely circular with a constant width. Fig. 2-6 (a) and Fig. 2-6 (b) show the rotor structure of the SynRM and the estimated flux barrier shapes, respectively.

(a)   (b)
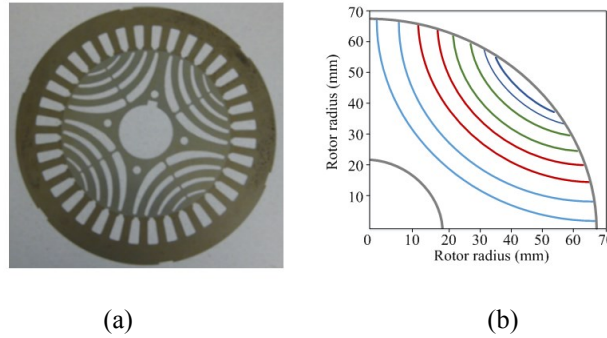
Fig. 2-6 (a) Rotor and stator laminations of the SynRM, (b) simplified model of the rotor

The effect of each flux barrier on the air gap flux is considered independently from other flux barriers. The rotor part is divided into four sections, each section encompassing one of the four flux barriers. The first three sections each cover 10 degrees of the half rotor pole, while the fourth section which includes the smallest flux barrier on the top covers 15 degrees of the half rotor pole. The flux barrier in each section increases the reluctance of the flux path when compared to the same section with no flux barrier. Thus with a constant air gap MMF produced by the stator winding, the air gap flux reduces in the presence of the flux barriers. The reluctance of each pole section $\mathcal{R}$, can be calculated using (2.22):

$$\mathcal{R} = \frac{l}{\mu A} \tag{2.22}$$

where l, μ, and A are the length, magnetic permeability, and surface area of the magnetic flux path, respectively. The presence of the flux barrier affects the available area in each section, A. The aim of the proposed method in here is to translate the reduction in the available area into an additional air gap length which covers the span of the flux barrier. Fig. 2-7 shows a schematic view of the of the rotor pole, and its flux barriers.
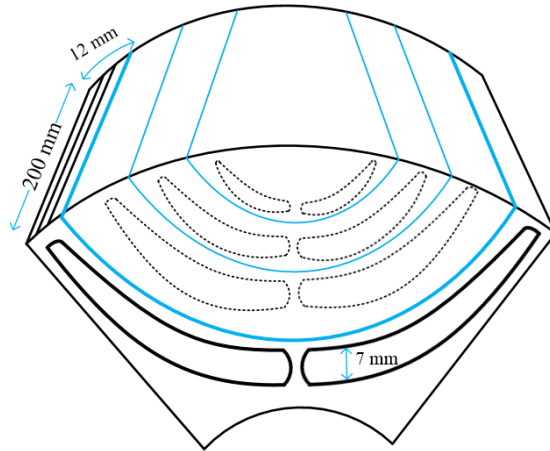
Fig. 2-7 Modeling the effect of the flux barrier on the air gap magnetic flux

The first section in the rotor pole contains the largest flux barrier and is highlighted in Fig. 2-7. The approximate dimensions of this section are presented in this figure. The available pole section as a result of the presence of the flux barrier is reduced from 0.0023 m² to 0.00134 m². Since a constant air gap MMF is provided by the stator winding, increasing the section reluctance, results in air gap flux reduction ($\mathcal{F} = \mathcal{R}\varphi$). To model the increased reluctance of the flux path, an additional air gap length, l_{fb} for each rotor section is considered which substitutes the flux barrier. In a pole section with no flux barrier (only made of highly permeable steel), the reluctance of the flux path, $\mathcal{R}_1$ is mainly the reluctance of the air gap section above the rotor core (with length of l_g, and area of A). However when the flux barrier is considered in the section, the reluctance of the flux path, $\mathcal{R}_2$ increases due to the reduced steel area ($\mathcal{R}_1 < \mathcal{R}_2$). Thus the flux value reduces from φ_1 to φ_2 under constant MMF supply from the stator winding. At this stage of the modeling procedure it is assumed that the steel area is similar for a rotor section with no flux barrier and a rotor section with the flux barrier. This assumptions enables the following derivation shown in (2.23). Therefore, the effect of the reduced section area is modeled as a an increased air gap length shown by l_{fb}. Thus to model

the increased reluctance, an additional air gap length, l_{fb} is considered which accounts for the effect of the flux barrier and is obtained using the following derivation:

$$\mathcal{F}_1 = \mathcal{F}_2 \rightarrow \mathcal{R}_2\varphi_2 = \mathcal{R}_1\varphi_1 \rightarrow \left(\frac{l_{fb}}{\mu_0 A} + \frac{l_g}{\mu_0 A}\right)\varphi_2 = \frac{l_g}{\mu_0 A}\varphi_1 \rightarrow \left(l_{fb1} + l_g\right)\varphi_2 = l_g\varphi_1$$

$$\rightarrow l_{fb1} = \left(\left(\frac{\varphi_1}{\varphi_2}\right) - 1\right)l_g$$

(2.23)

where l_{fb}, φ_1, φ_2, and l_g are the equivalent air gap length representing the first flux barrier, air gap flux per pole of the section without the flux barrier, air gap flux per pole of the section when the flux barrier is present in the section, and the air gap length, respectively. Considering the machine's geometry, and according to the dimensions provided in Fig. 2-7 the additional air gap length as a result of the biggest flux barrier, shown in Fig. 2-7, is 0.7 mm. To obtain the value of the l_{fb1} from (2.23), knowing the values of the magnetic flux φ_1, and φ_2 is not necessary (The flux values are not available at this stage of modeling). Assuming a similar air gap MMF value produced by the stator winding in the two cases of with and without flux barrier in the section, and considering a constant relative magnetic permeability for the steel, μ_R in the two cases, one can write:

$$(\mathcal{R}_{iron1} + R_{ag1})\varphi_1 = (\mathcal{R}_{iron2} + R_{ag2})\varphi_2 \rightarrow \left(\frac{l_{iron}}{\mu_0\mu_R A_1} + \frac{l_g}{\mu_0 A_1}\right)\varphi_1$$

$$= \left(\frac{l_{iron}}{\mu_0\mu_R A_2} + \frac{l_g}{\mu_0 A_2}\right)\varphi_2 \rightarrow \frac{\varphi_1}{\varphi_2} = \frac{\mu_R A_1\left(\mu_R l_g + l_{iron}\right)}{\mu_R A_2\left(\mu_R l_g + l_{iron}\right)} \rightarrow \frac{\varphi_1}{\varphi_2} = \frac{A_1}{A_2}$$

(2.24)

where $\mathcal{R}_{iron1}$, $\mathcal{R}_{iron2}$, R_{ag1}, R_{ag2}, l_g, A_1, A_2, and l_{iron} are the reluctance of the rotor section without the flux barrier, the reluctance of the section in the presence of the flux barrier, the reluctance of the air gap above the section without the flux barrier, the reluctance of the air gap above the section with the flux barrier, the length of the air gap, the area of the section without the flux barrier, the area of the section with the flux barrier ($A_2 < A_1$), and the length of the flux path in the rotor which is equal to the equivalent length of the section, and similar for the two cases (with and without the flux barrier in the section). The air gap section area is considered according to the steel area for each case. Therefore the ratio between the magnetic flux values in (2.23) can be replaced by the final equation obtained from (2.24). This equation shows how

the variation in the section area due to the flux barrier affects the amount of magnetic flux that passes through under constant supply MMF condition.

The effect of other flux barriers on the air gap flux is also calculated in the same manner and then added to obtain the equivalent air gap length at each point along the pole. This method is easy to apply and it considers the main characteristics of the flux barriers; that is the covering span, and the width. Fig. 2-8 (a) shows the individual equivalent air gap lengths for each of the flux barriers and their overall effect.

The overall air gap function is estimated based on the obtained individual air gap lengths of each rotor section. A straight line connecting the start point of each flux barrier to the start point of the next one is used to model the transition between two adjacent flux barriers as shown in Fig. 2-8 (b). Eventually the effect of the physical air gap is added to the final function, which creates a shift in the final air gap function. Fig. 2-8 (b) shows the calculated air gap function using the simplified flux barrier structure.

To examine the accuracy of the proposed air gap function for the SynRM, the air gap flux of the SynRM is calculated using the analytical model and compared with the air gap flux obtained from FEA simulation. The same calculations are also performed for two other design variations; a rotor with no flux barriers, and a rotor with three flux barriers (without the smallest flux barrier). Fig. 2-8 (c) compares the air gap magnetic flux curves under DC excitation, obtained from the analytical model with the curves obtained from FEA for three different cases; the SynRM with all four flux barriers (the base SynRM), a SynRM rotor without the smallest flux barrier on the top, and a rotor topology with no flux barriers (solid rotor). Although there is a small deviation between the curves obtained from the analytical model, and the corresponding curves obtained from FEA simulation, the two modeling methods depict the effect of the flux barriers on the air gap flux distribution of the machine. It is observed from FEA simulation that the presence of the flux barriers alters the uniform distribution of the magnetic flux in the air gap (under DC excitation) from a case with no flux barriers (solid rotor) to the cases where the flux barriers are present in the rotor. The minimum value of the air gap magnetic flux is also affected by the number of the flux barriers as shown for the base SynRM, and a SynRM with three flux barriers.
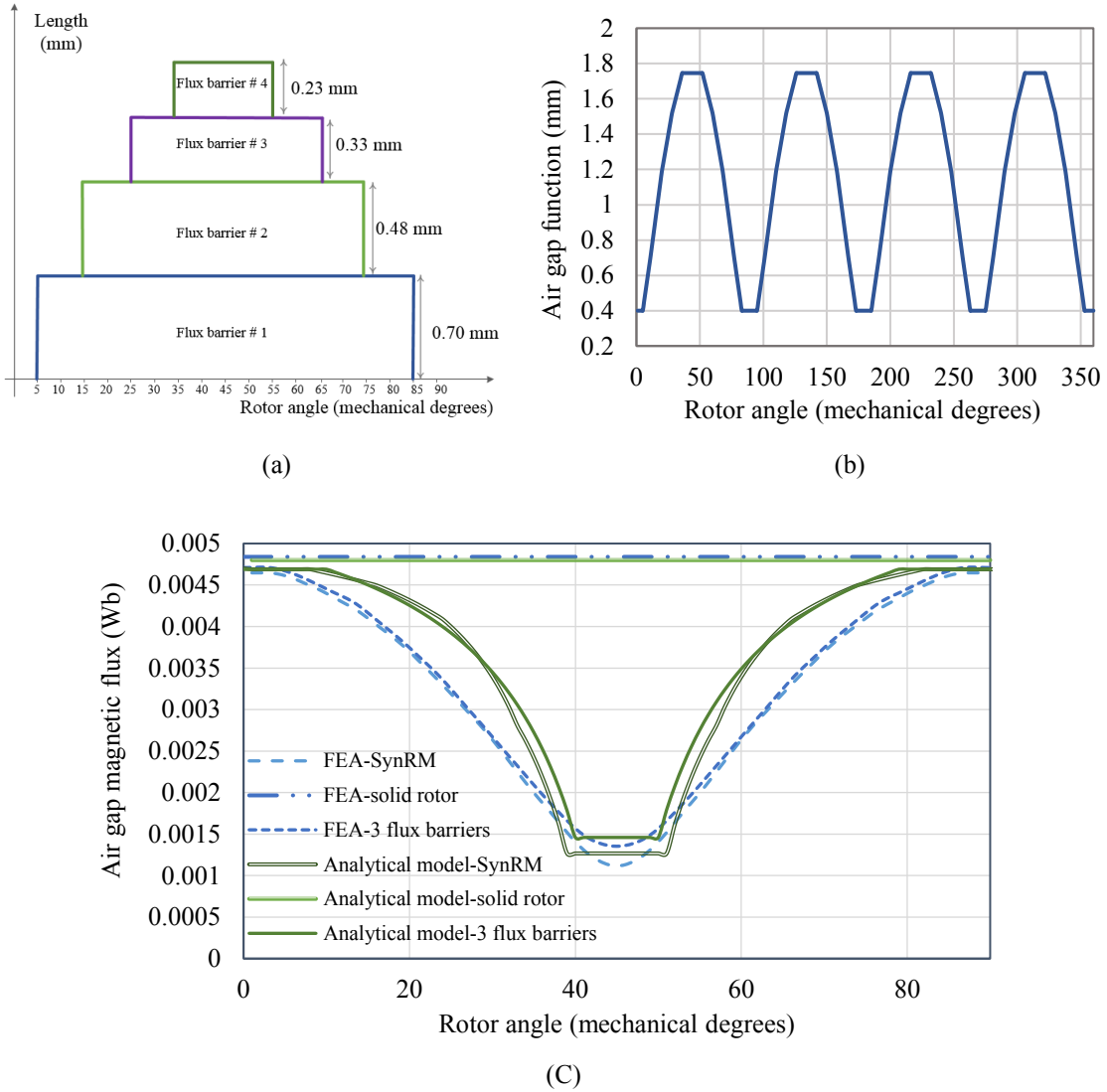
Fig. 2-8 (a) The extra equivalent air gap length of individual flux barriers; (b) the overall air gap function of the SynRM (c) air gap magnetic flux obtained from FEA and the analytical model for the three cases of the SynRM rotor, a rotor with three flux barriers, and a solid rotor

2.3.4. Electromagnetic Torque Calculation

Once the winding function and the air gap function are obtained, the self-inductance of each phase and the mutual inductances between the phases are calculated using (2.25) and (2.26) [13].

$$L_{AA} = \mu_0 r l_{stack} \int_0^{2\pi} N_A N_A g_\theta^{-1} d\theta \qquad (2.25)$$

$$L_{AB} = \mu_0 r l_{stack} \int_0^{2\pi} N_A N_B g_\theta^{-1} d\theta \tag{2.26}$$

where μ_0, r, l_{stack}, N_A, N_B, g_θ^{-1}, and θ are the magnetic permeability of the free space, rotor outer radius, stack length of the machine, winding function of phase A, winding function of phase B, inverse of the air gap function, and the rotor angle, respectively. L_{AA}, and L_{AB} are the self-inductance of phase A, and the mutual inductance between phase A and phase B, presented here as an example. The rest of the matrix inductance element are also calculated in the same manner considering the spatial displacement between the windings. Fig. 2-9 (a) and Fig. 2-9 (b) show the self-inductance and the mutual inductance of the machine's phases calculated using (2.25) and (2.26). The self-inductance of the other two phases are similar to the one depicted in Fig. 2-9 (a), only displaced by 120 degrees.

Using the coenergy method, the electromagnetic torque is calculated at different rotor angles, and for various current magnitudes. Equation (2.27) shows the electromagnetic torque, T equation.

(a)   (b)
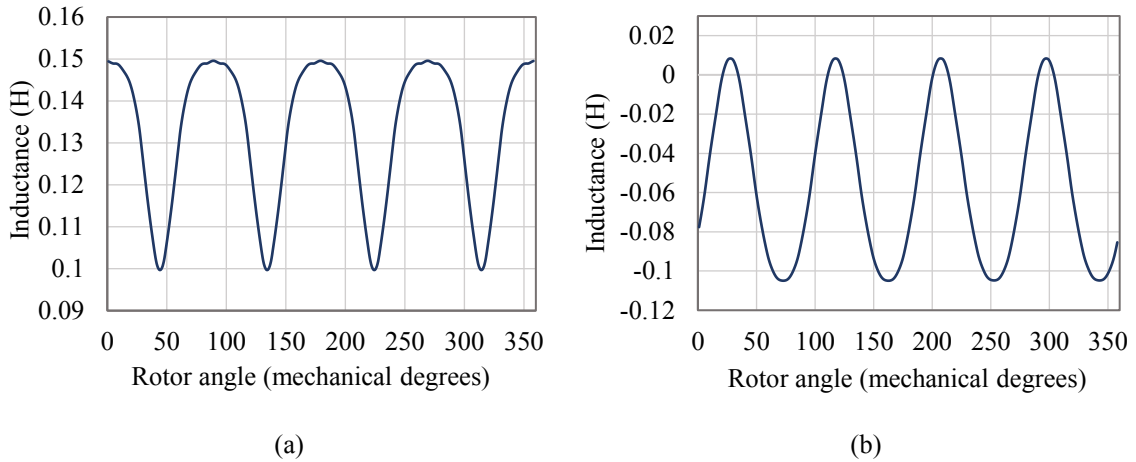
Fig. 2-9 (a) Self-inductance of the machine's phase, (b). Mutual inductance between two phases

$$T = \frac{1}{2}[I]^T \left[\frac{\partial L(\theta)}{\partial \theta}\right] [I] \tag{2.27}$$

$[I]$ is the current vector, which for a three phase machine consists of the currents of the three phases, and $\partial L/\partial \theta$ is the derivative of the inductance matrix with respect to the rotor angle, θ. Using (2.27) the torque-angle curves of the SynRM for various phase currents are obtained.

The results of the analytical model are compared with FEA simulation and experimental results in section 2.4.

The proposed model is also used to calculate the torque waveform of the SynRM. In this approach the tangential and radial components of the magnetic flux density in the air gap of the SynRM are initially estimated using the air gap function (Fig. 2-7 (b)), and the air gap MMF (Fig. 2-4). The electromagnetic torque waveform of the machine is later calculated based on the Maxwell Stress Tensor method.

Using the Maxwell Stress Tensor $\mathbb{T}$, the force on a moving charge in an electromagnetic field can be calculated using (2.28) in a cylindrical coordinate system [61].

$$\mathbb{T} = \frac{1}{\mu_0} \begin{bmatrix} \dfrac{B_{rad}^2 - B_{tan}^2 - B_z^2}{2} & B_{tan}B_{rad} & B_{rad}B_z \\[3mm] B_{tan}B_{rad} & \dfrac{B_{tan}^2 - B_{rad}^2 - B_z^2}{2} & B_{tan}B_z \\[3mm] B_z B_{rad} & B_z B_{tan} & \dfrac{B_z^2 - B_{rad}^2 - B_{tan}^2}{2} \end{bmatrix} \tag{2.28}$$

where B_{rad}, B_{tan}, B_z are the radial, tangential, and the z component of the magnetic flux density in a cylindrical coordinate system. Accordingly, the electromagnetic force, F can be written as [61]:

$$F = \int_V \nabla.\mathbb{T}\, dv \tag{2.29}$$

where V is the volume encompassing the object on which the force is calculated (for example the rotor of the SynRM). Since the rotor has only one degree of freedom (spinning around the z axis), the tangential component of the force performs the electromechanical energy conversion. Equation (2.30) shows the tangential component of the electromagnetic force calculated using the Maxwell Stress Tensor.

$$F_\theta = \frac{1}{\mu_0} \oint_S B_{rad}.B_{tan}\, dS \tag{2.30}$$

Using equation (2.30), the electromagnetic torque is calculated as shown in (2.31) [62, 51]:

$$T = \frac{1}{\mu_0} \oint_S r. B_{rad}. B_{tan} dS \tag{2.31}$$

where S, and r are the surface of integration which in this case is a cylinder enclosing the rotor, located in the air gap of the machine, and the rotor outer radius, respectively. Equation (2.31) can be rewritten as [29]:

$$T = \frac{r^2}{\mu_0} \int_0^{2\pi} \int_0^{l_{stack}} B_{rad}. B_{tan} d\theta dl \tag{2.32}$$

where θ, and l_{stack} are the rotor angle, and the stack length, respectively.

(a)   (b)
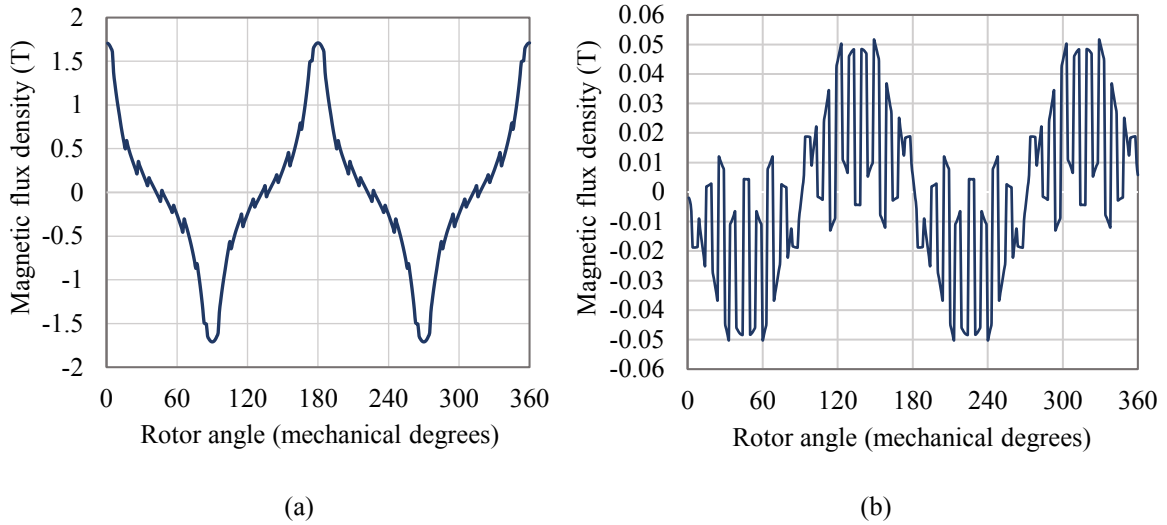
Fig. 2-10 Magnetic flux density components in the air gap, (a). Radial component, and (b). Tangential component

To obtain the radial and tangential components of the air gap magnetic flux density, the air gap function and the air gap MMF equations are used. The radial component of the magnetic flux in the air gap, φ_{rad} is calculated for 360 points located in the air gap of the machine enclosing the rotor (the air gap function and the winding function are also calculated with one degree resolution). The tangential component of the air gap flux, φ_{tan} is also calculated using the air gap MMF and the reluctance of the tangential flux path, $\mathcal{R}_{ag_{tan}}$. The two components are shown in equation (2.33):

$$\varphi_{rad} = \frac{\mathcal{F}_s}{\mathcal{R}_{ag_{rad}}} \quad , \quad \varphi_{tan} = \frac{\mathcal{F}_{s_{n+1}} - \mathcal{F}_{s_n}}{\mathcal{R}_{ag_{tan}}} \tag{2.33}$$

where, $\mathcal{F}_s$, and $\mathcal{R}_{ag_{rad}}$ are the MMF produced by the stator at each point along the rotor periphery, and the reluctance of the flux path which is obtained using the air gap function shown in Fig. 2-8 (b). To calculate $\mathcal{R}_{ag_{rad}}$ the length of the flux path is considered according to the air gap function, while the surface area covers one degree span of the rotor periphery times the stack length of the machine. The tangential component of the air gap magnetic flux density is also calculated using the stator MMF. The difference between the two adjacent values of the air gap MMF ($\mathcal{F}_{s_{n+1}}$ and $\mathcal{F}_{s_n}$) is obtained using the MMF curve shown in Fig. 2-4, and divided by the reluctance of the path between the two adjacent points in the air gap of the machine, $\mathcal{R}_{ag_{tan}}$. Both radial and tangential components of the air gap flux density are calculated based on one degree resolution which is used for MMF and air gap function calculations, and are shown in Fig. 2-10 (a) and Fig. 2-10 (b).

Once the tangential and radial components of the air gap magnetic flux density are calculated for 360 points along the rotor periphery for a particular rotor position, the rotor and the stator MMF are shifted in step of one degree and the whole procedure is repeated to obtain the new values of the radial and tangential air gap flux densities at the new rotor position along the air gap. Therefore a set of curves similar to the curves shown in Fig. 2-10 (a), and Fig. 2-10 (b) are obtained which are shifted with respect to one another.

To obtain the torque waveform (2.32) must be solved for a sufficient number of rotor positions which depends on the machine periodic structure (for this SynRM 90 degrees mechanical is sufficient). At each rotor position the radial and tangential components of the magnetic flux density in the air gap varies when compared to the previous rotor position, and thus the obtained value for the torque changes. Fig. 2-11 shows the electromagnetic torque waveform calculated using the analytical model for 12 A line rms current, and the electromagnetic torque waveform obtained from the FEA (both curves show the peak torque of the machine). The analytical model predicts an average torque of 27.9 Nm, while the average torque obtained from the FEA is 28.8 Nm.
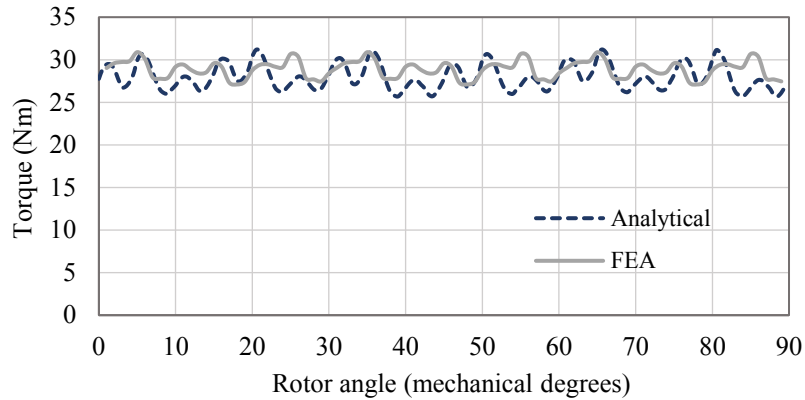
Fig. 2-11 Electromagnetic torque calculated by the analytical model compared with FEA

2.3.5. Design Variation of the Synchronous Reluctance Machine

One of the main applications of an analytical model of electrical machines and in particular the SynRM, is the possibility to estimate the effect of various design parameters on the performance of the machine. The proposed analytical model enables the examination of the effects of various parameters such as winding distribution, and number of winding turns, rotor diameter, stack length of the machine, number of the flux barriers, width of the flux barriers, and pole arc to pole pitch ratio of the machine on the output characteristics. This study can provide a guideline for an initial design procedure. The initial design parameters obtained from the analytical model can be later verified using FEA software simulation. Therefore the FEA simulation can be performed on a limited number of initial designs obtained from the analytical model. To examine the capability of the proposed analytical model as a design tool three cases of design variations are presented, of which two are focused on design parameters associated with rotor geometry, and the third one considers the stator winding turns.

The pole arc to pole pitch ratio of the machine, and the widths of the flux barriers are two of the most important geometrical parameters in a SynRM. The former affects the average torque of the SynRM as well as the torque ripple. While the latter mainly alters the average torque produced by the motor.

Pole arc to pole pitch ratio of a SynRM is defined based on the location of the tip points of the biggest flux barrier. This parameter directly affects the air gap function of the machine, shown in Fig. 2-8 (b). Two different values for the pole arc of the analyzed machine are used, one larger than the pole arc of the original SynRM, and one smaller (the pole arc to pole pitch

ratio of the original SynRM is 0.8). Fig. 2-12 (a) shows the two air gap functions obtained for the two design variations with different pole arc to pole pitch ratio. Fig. 2-12 (b) shows the difference in the electromagnetic torque waveform obtained from the two design variations with the same supply condition as shown in Fig. 2-11. The average value of the torque waveform for the SynRM with a larger pole arc is 29.3 Nm, while the average value of the torque waveform for the SynRM with smaller pole arc is 31.2 Nm. This depicts how small variations in design parameters can affect the machine's performance. The torque ripple percentage of the SynRM is also affected by the pole arc to pole pitch ratio. The torque ripple of the design with small pole arc is 19.1 percent, while the torque ripple of the design with a larger pole arc is 22.4 percent.
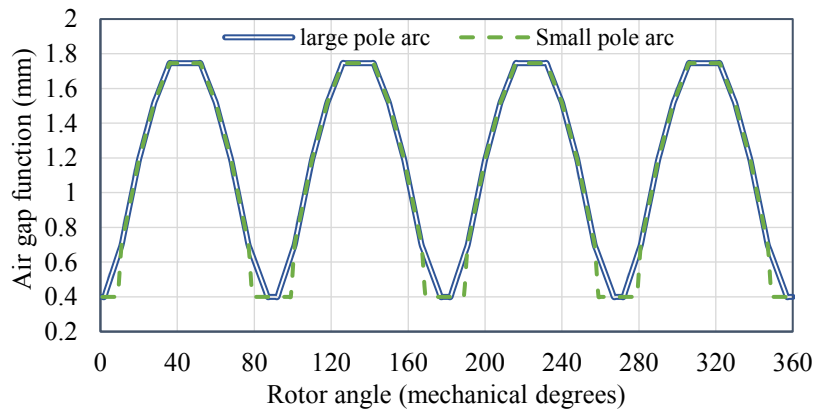
(a)
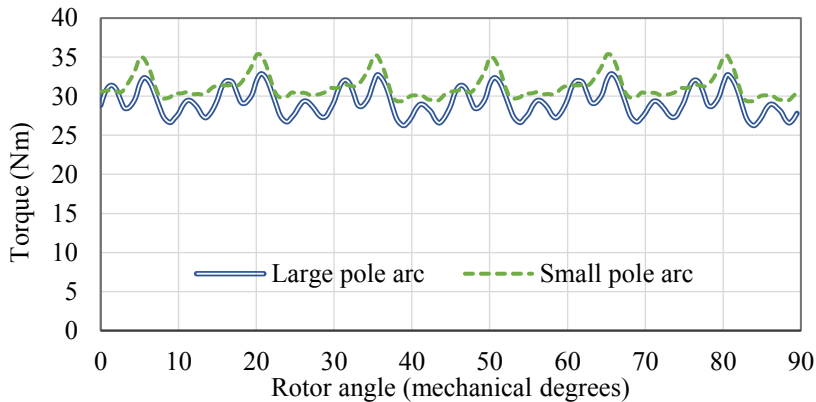
(b)

Fig. 2-12 The air gap function of the design variations of the SynRM with different pole arc to pole pitch ratios; (b) The electromagnetic torque waveform of the design variations with different pole arc to pole pitch ratios

The torque production capability of the SynRM is also affected by the width of the flux barriers [25], [58], [7]. Generally speaking, a larger flux barrier width results in the *d*-axis flux

reduction due to the smaller available area, as well as the saturation of the steel core. For this study an additional width of 1 mm is added to each flux barrier of the SynRM. The air gap function of the machine shown in Fig. 2-8 (b) is modified to account for the effect of the larger flux barrier width. The air gap function of this design variation is shown in Fig. 2-13 (a), and compared with the air gap function of the base SynRM. Fig. 2-13 (b) compares the torque waveforms obtained from the analytical model. The average value of the torque waveform is 27.03 Nm which is 0.9 Nm less than the average torque obtained from the base SynRM (shown in Fig. 2-8).
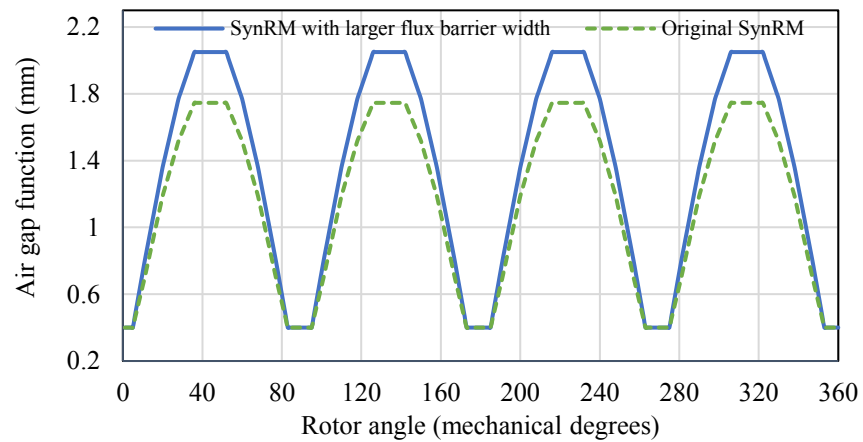
(a)
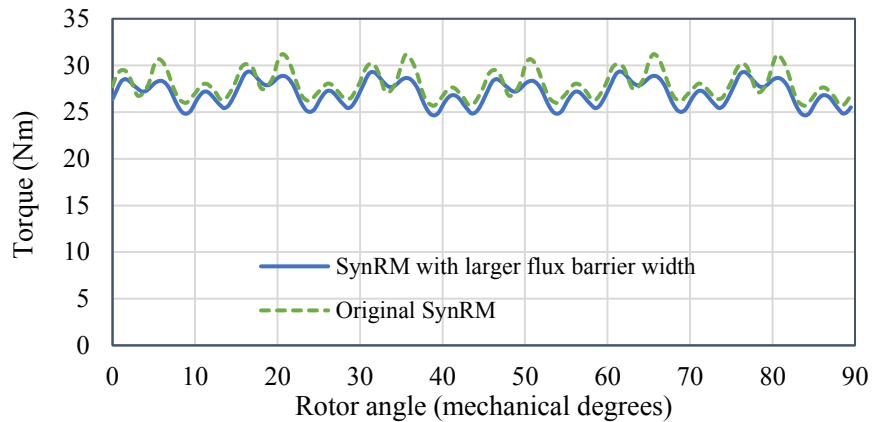
(b)

Fig. 2-13 The air gap function of the design variations of the SynRM with different flux barrier widths; (b) The electromagnetic torque waveform comparison

The effect of stator parameters such as winding configuration is also examined using the proposed analytical model. Here the effect of the number of the winding turns on the torque production capability of the SynRM is examined using the proposed analytical model, and the

result is compared with the FEA result. Fig. 2-14 shows the torque waveform of a SynRM with 15 winding turns per slot, while other geometrical parameters are similar to that of the original SynRM. The torque waveforms shown in Fig. 2-14 present the steady state operation of the SynRM with 12 A line rms current obtained from the analytical model and the FEA. The average value of the torque waveform obtained from the analytical model for this operating condition is 10.79 Nm, while the FEA waveform has an average value equal to 11.12 Nm.

This study shows the capability of the proposed analytical model of the SynRM as a relatively accurate model for design and analysis of SynRMs. Similarly other design parameters such as winding distribution, and the main dimensions (rotor outer diameter, and the stack length) can be altered and their effect on the performance of the SynRM (in terms of output torque, torque ripple, torque-angle curve) can be studied. In the third chapter the proposed analytical model is used for modeling and design of a PM assisted SynRM. However to further analyze the accuracy and capability of the proposed analytical model, the torque-angle curves of the SynRM at different phase currents are compared with the torque-angle curves obtained from FEA, and measurement. The test procedure, FEA model, and the obtained results are compared with the analytical model's results in section 2.4.
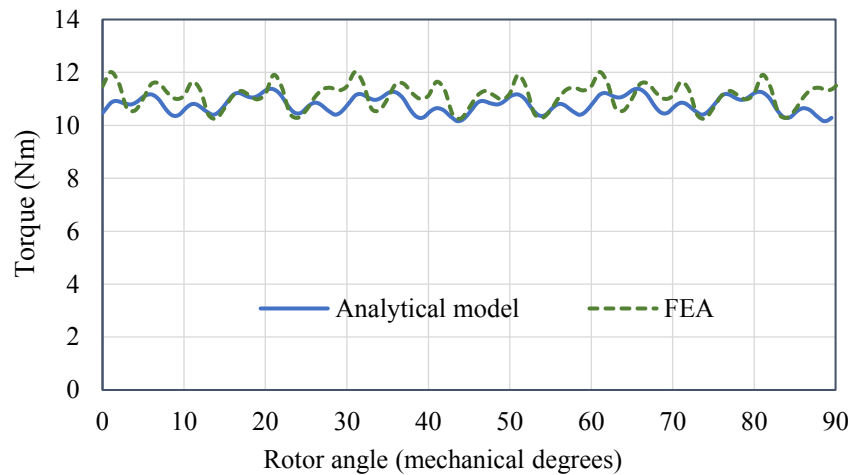
Fig. 2-14 Torque waveform comparison of FEA and analytical model for a SynRM with 15 winding turns per slot

2.4. Results and Validation

The proposed analytical model is verified with the result obtained from the FEA simulation, and the measurements performed on the prototyped SynRM. To perform the

verification of the proposed analytical model a specific test procedure is followed in which the static torque of the SynRM is measured at different rotor positions, and for various phase current magnitudes. A similar static simulation known as Magneto-static analysis is performed on the FEA model which replicates the actual measurement conditions. The obtained results are then compared with the analytical model results. The FEA model and the test procedure are explained in this section.
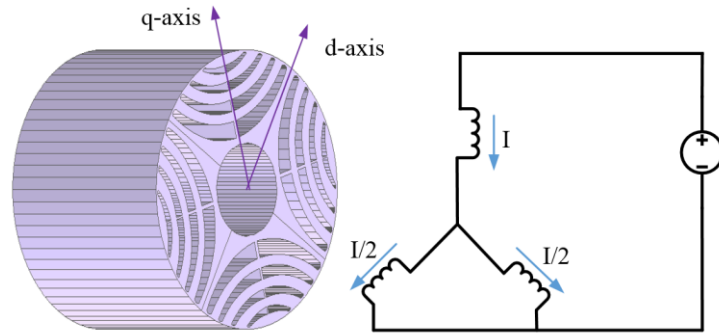
(a)
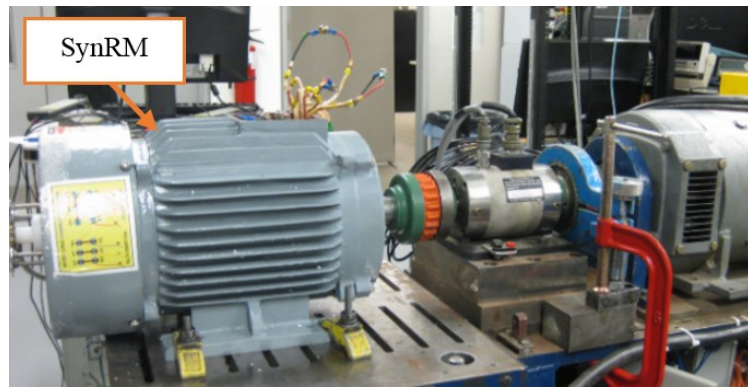
(b)

Fig. 2-15 (a) Schematic demonstration of the phase winding connection and the rotor of the SynRM, (b) Experimental setup

2.4.1. Experimental Procedure

The test procedure introduced here is a static torque measurement method in which the rotor of the electric machine (in this case the SynRM) is locked using a mechanical lock; the phase winding is connected in star mode while two of the phases are shorted, and a DC power

supply is connected across the shorted phases and the third phase winding as shown in Fig. 2-15 (a). The actual test setup is shown in Fig. 2-15 (b).

Initially the *d*-axis of the SynRM is located by supplying a proper amount of current which can rotate and lock the rotor. Once the *d*-axis is identified, the rotor is shifted in steps of 5 degrees electrical and a constant current magnitude is injected to the winding at each step, and the exerted torque on the shaft is measured using the torque transducer of the test bench. This procedure is repeated for rotor positions varying from 0 (*d*-axis) to 90 (*q*-axis) degrees, in steps of 5 degrees, and for current magnitudes from 4 A to 18 A, in steps of 2 A. The obtained results are shown in Fig. 2-17.

2.4.2. FEA Simulation

FEA is used by many researchers for modeling, design, and analysis of various types of electric machines [6, 23, 25, 59, 63, 64, 65, 66]. In this research FEA simulation is used for verification of the proposed analytical model. This verification is done based on the torque-angle curves at different rotor positions, and for various current magnitudes as stated for the test procedure.
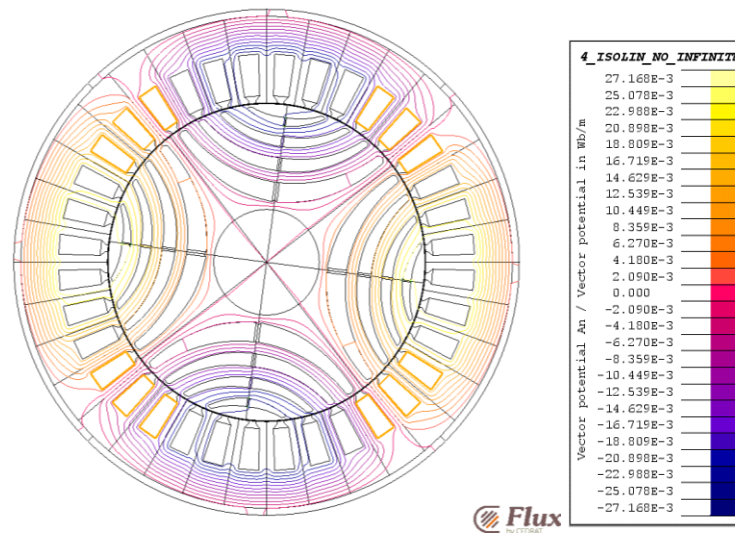
Fig. 2-16 Magnetic vector potential at 14 A and 37.5 mechanical degrees

To perform the FEA simulation of the SynRM and obtain the torque-angle curves of the machine, the Magneto-Static package of Flux.11.1 is used. Fig. 2-16 shows the cross section of the simulation result of the magnetic vector potential at 14 A and 37.5 mechanical degrees.

2.4.3. Torque-Angle Curves of the Synchronous Reluctance Machine

The torque values obtained from the test procedure described in section 2.4 and the FEA simulation presented in section 2.4.2 are compared with the results of the analytical model obtained from the coenergy method (equation (2.27)), and are shown in Fig. 2-17. Each graph shown in Fig. 2-17 depicts the average value of the torque from 0 to 90 degrees electrical and at two different current magnitudes obtained from the measurement, FEA simulation, and the proposed analytical model.
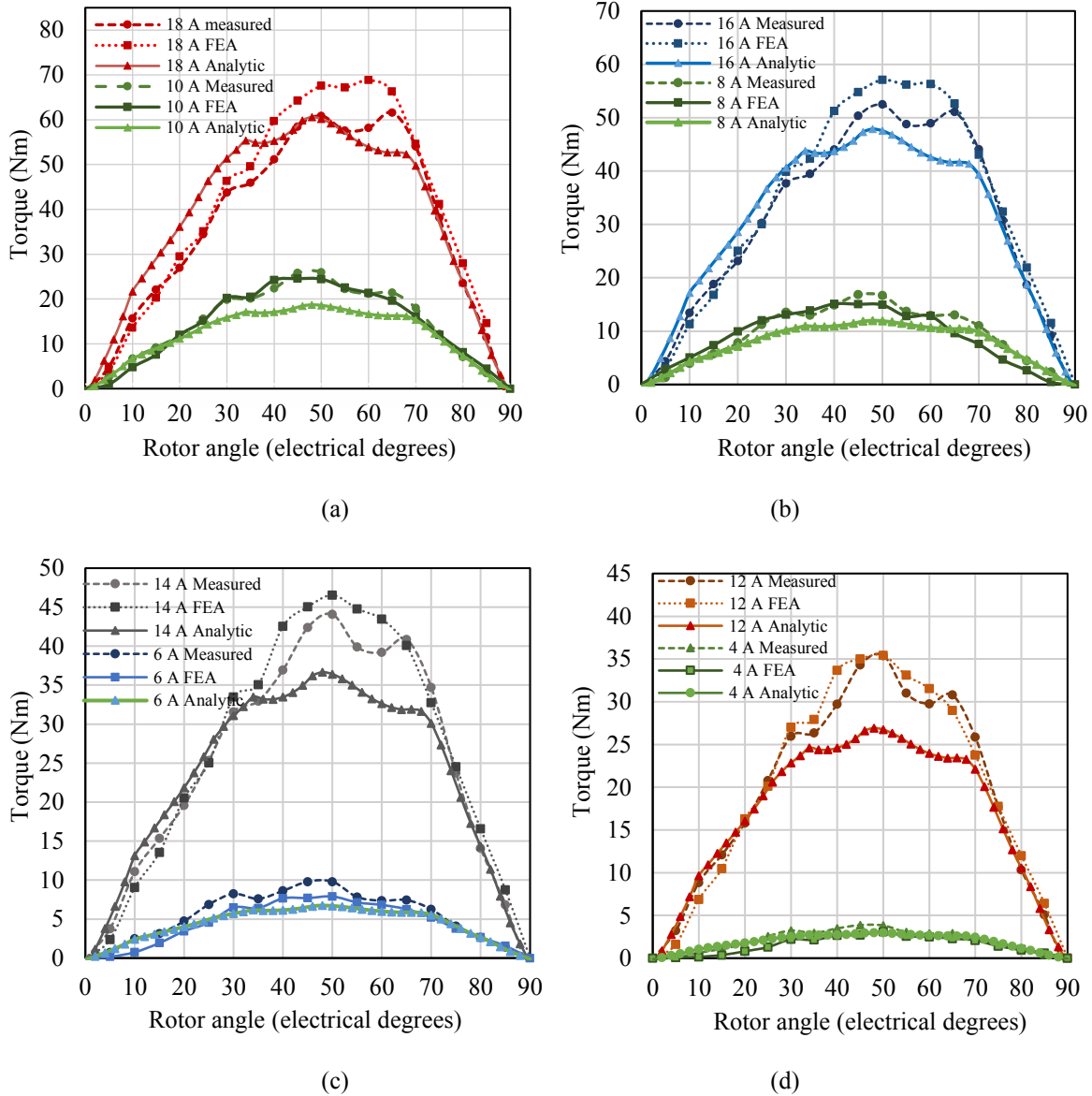
Fig. 2-17 FEA, analytical model, and experimental results, (a). 18 A and 10 A, (b). 16 A and 8 A, (c). 14 A and 6 A, (d). 12 A and 4 A
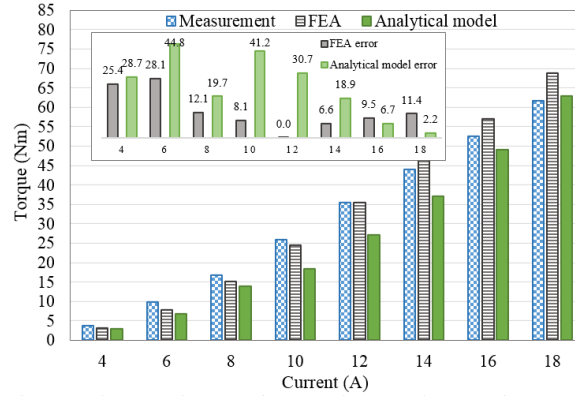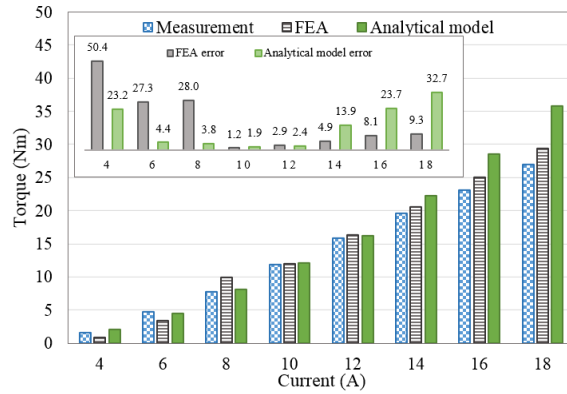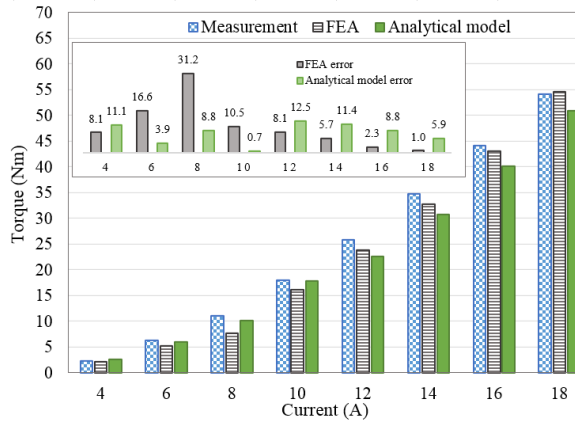
Fig. 2-18 Torque comparison of the three methods, at (a) 20 degrees; (b) 50 degrees; (c) 70 degrees

In Fig. 2-18 the torque magnitude for three different rotor positions (50, 20, and 70 degrees), and for various phase currents, obtained from FEA, analytical model, and measurement are compared. These bar charts also include the percentage relative error of the analytic model results, and FEA results at different current magnitudes for the three rotor position values. Fig. 2-18 (a) shows the result of torque magnitude for the angle of 20 degrees. The highest deviation between the measurement and the analytical model happens at this load

angle when compared to the other two rotor angles shown in Fig. 2-18 The maximum error of the analytical model at this rotor angle is 44.8 percent for 6 A, while the maximum error of the FEA is 28.1 percent which happens at the same current magnitude. Fig. 2-18 (b) depicts the torque magnitude at the peak point of the load angle (50 degrees electrical). The maximum error of the analytical model is 32.7 percent which happens at 18 A. The maximum error of the FEA result is 50.4 percent and is at 4 A. Fig. 2-18 (c) represents the torque value for the rotor angle of 70 degrees for different phase currents. The maximum error of the analytical model when compared to the measurement is 12.5 percent which occurs at 12 A, while the maximum error of the FEA happens at 8 A, and is around 31.2 percent.

The observed error between the measurement and the FEA simulation has various origins. The change in the steel lamination magnetic properties during the cutting, bonding, and machining procedure of the rotor and the stator assembly, the inevitable difference between the BH curve of the lamination used in the software and the steel used in the prototype are two of the causes of such errors. On the other hand, the measurement error which originates from the uncertainties in the measurement devices such as the torque transducer, the power supply, and the encoder, adds up to the deviations between the measurements and the simulated torque.

The analytical model can be improved by specifying various air gap functions for certain regions of rotor, and different current magnitudes. However this adds to the complexity of the model. The effect of steel saturation or other physical parameters such as grain orientation in CRGO steel can also be added to the analytical model. The modeling procedure of the CRGO steel is also discussed in this chapter, and the results are shown for a previously prototyped SynRM made of CRGO steel sheets.

2.5. Segmented-Pole Synchronous Reluctance Machine Modeling

A design variation of the SynRM to improve the saliency is presented in [60]. In this topology each rotor lamination is divided into four sections (depending on the number of rotor poles), each section made of a cold rolled grain-oriented steel sheet. In each of the four sections, the steel orientation is placed in favor of the *d*-axis flux path. Therefore in addition to the flux barrier effect in creating rotor saliency, the material characteristic is also influential. This section initially presents the segmented-pole SynRM briefly. The analytical model is modified to take into account the effect of steel characteristic on the saliency ratio and output

performance of the SynRM. Finally the results of the analytical model are compared with FEA and measurement results. This section also presents a comparison between the SynRM and the segmented-pole SynRM.

2.5.1. The Cold Rolled Grain Oriented Steel and Segmented-Pole SynRM

The steel type used in the SynRM presented earlier in this chapter is made of non-grain-oriented (CRNGO) steel laminations, M15 G29. CRNGO steel materials possess uniform magnetic and electric characteristics throughout their surface. Therefore the steel placement regarding the applied magnetic field direction, does not affect the magnitude of the magnetic flux density passing through the steel lamination. The grain oriented steel on the other hand has magnetic domains oriented in the rolling direction of the steel, so called the CRGO steel. Such steel material shows superior magnetic characteristics along the rolling direction while the magnetic permeability of the steel when the field is perpendicular to the rolling direction is even less than the magnetic permeability of the CRNGO steel. Fig. 2-19 compares the magnetic permeability of two different steel types; M15 G29, and M5 (a CRGO steel material) obtained from measurement using the DONART test setup. The CRGO steel is tested under two conditions, once with a field parallel to the steel orientation direction, and the other time with a perpendicular field. This figure shows the difference in magnetic permeability of the two steel types. However the superior magnetic characteristic of the CRGO steel reduces at high flux density magnitudes. Thus when exposed to strong magnetic fields resulting in high magnetic flux density values (above 1.4 T) the magnetic permeability of the CRGO and CRNGO steel is not significantly different.
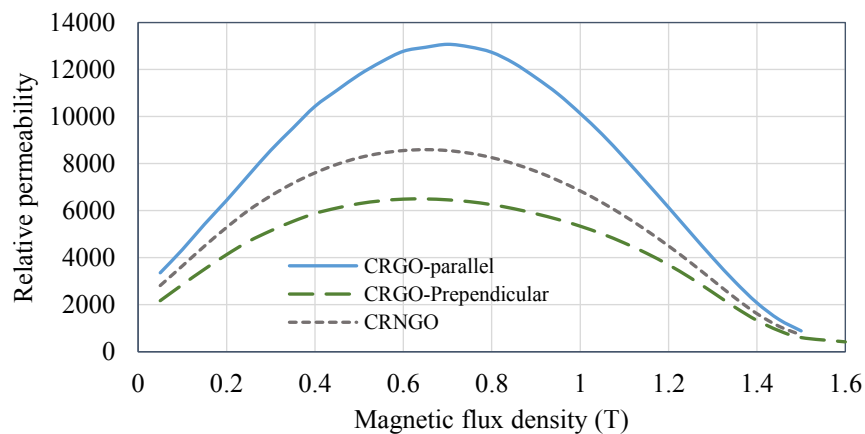
Fig. 2-19 Relative permeability of CRGO and CRNGO steels

Using the CRGO steel with the magnetic permeability presented in Fig. 2-19 a segmented-pole SynRM is designed and prototyped [67]. Each rotor lamination is made of four separate pieces of CRGO steel with the rolling direction of each parallel to the d-axis flux path of the rotor. The rotor dimensions are the same as the rotor of the SynRM introduced earlier in this chapter (Table. 2-1). Therefore the segmented-pole SynRM and the regular SynRM share the same stator. Fig. 2-20 (a) shows the rotor and stator laminations of the segmented-pole SynRM. Fig. 2-20 (b) shows the simulation model of the segmented-pole SynRM. In this figure green arrows show the rolling direction of each rotor section, while the red arrows present the path with lower permeability (the perpendicular path). In the following section the analytical model which was presented earlier in this chapter is modified to account for the effect of CRGO steel on the output characteristics of the segmented-pole SynRM.

(a)   (b)
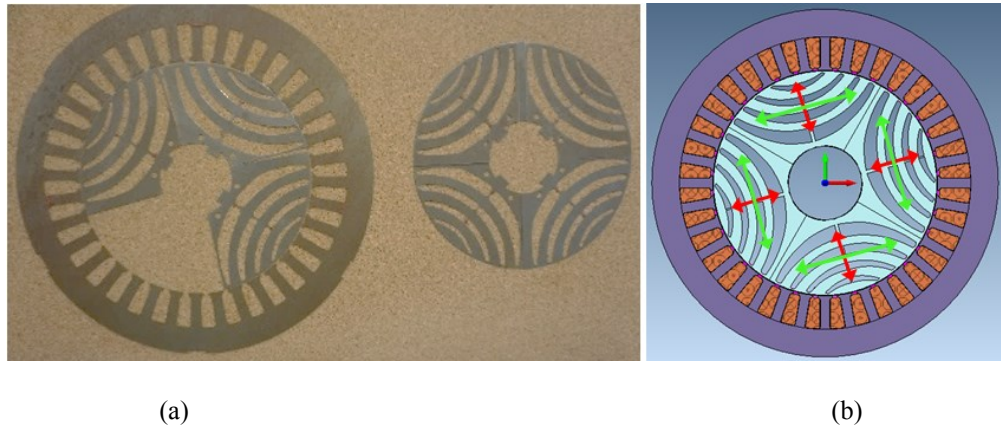
Fig. 2-20 (a) Stator and rotor laminations of the segmented-pole SynRM; (b) The simulation model of the segmented-pole SynRM

2.5.2. The Analytical Model of the Segmented-Pole SynRM

The analytical model which was presented in this chapter is also used for modeling the segmented-pole SynRM. The model is modified to incorporate the effect of steel permeability in the performance of the segmented-pole SynRM.

In the magnetic circuit of the SynRM with constant MMF produced by the stator winding, the increased reluctance of the flux path due to the presence of the flux barrier, results in magnetic flux reduction. In a SynRM the flux barrier reduces the available area for the magnetic flux, thus resulting in a higher reluctance of the flux path. Earlier in this chapter equations (2.23) and (2.24) are presented for air gap function calculation. However in (2.24)

the effect of steel permeability is removed to obtain the final equation in (2.23) which calculates the equivalent air gap length representing the air gap function. To model the CRGO steel in SynRM the effect of steel permeability must be reflected in the air gap function. Therefore (2.24) is written and this time the magnetic permeability of the steel is also considered:

$$\begin{aligned}(\mathcal{R}_{iron1} + R_{ag1})\varphi_1 = (\mathcal{R}_{iron2} + R_{ag2})\varphi_2 &\rightarrow \left(\frac{l_{iron}}{\mu_0\mu_{R1}A_1} + \frac{l_g}{\mu_0 A_1}\right)\varphi_1 \\ = \left(\frac{l_{iron}}{\mu_0\mu_{R2}A_2} + \frac{l_g}{\mu_0 A_2}\right)\varphi_2 &\rightarrow \frac{\varphi_1}{\varphi_2} = \frac{\mu_{R1}A_1(\mu_{R2}l_g + l_{iron})}{\mu_{R2}A_2(\mu_{R1}l_g + l_{iron})}\end{aligned}$$

(2.34)

where $\mathcal{R}_{iron1}, \mathcal{R}_{iron2}, R_{ag1}, R_{ag2}, A_1, A_2,$ and l_{iron} are the reluctances of the rotor sections without the flux barrier, the reluctance of the same section in the presence of the flux barrier, the reluctance of the air gap above the section without the flux barrier, the reluctance of the air gap above the section with the flux barrier, the area of the section without the flux barrier, the area of the section with the flux barrier ($A_2 < A_1$), and the length of the flux path in the rotor which is equal to the equivalent length of the section. The air gap function of the segmented-pole SynRM is obtained by updating the air gap function of the regular SynRM. μ_{R1} and μ_{R2} are the relative permeability of the CRNGO steel and the CRGO steel, respectively.

In this case the difference between the air gap function of the regular SynRM, and the air gap function of the segmented-pole SynRM is obtained assuming a similar steel area for the two machines. The difference between the steel relative permeability of CRGO (used in the segmented-pole SynRM) and CRNGO (used in the regular SynRM) steels is used to update the air gap function of the segmented-pole SynRM relative to the regular SynRM. Therefore (2.34) is rewritten as:

$$\frac{\varphi_{CRGO-SynRM}}{\varphi_{SynRM}} = \frac{\mu_{RCRGO-SynRM}(\mu_{RSynRM}l_g + l_{iron})}{\mu_{RSynRM}(\mu_{RCRGO-SynRM}l_g + l_{iron})}$$

(2.35)

where $\varphi_{CRGO-SynRM}, \varphi_{SynRM}, \mu_{RCRGO-SynRM},$ and μ_{RSynRM} are the magnetic flux of the segmented-pole SynRM, the magnetic flux of the regular SynRM, the relative magnetic permeability of the CRGO steel, and the relative magnetic permeability of the CRNGO steel.

(2.35) is then utilized to include the effect of the CRGO steel in the air gap function of the segmented-pole SynRM. Since the permeability of the steel is a function of the magnetic flux (see Fig. 2-19), the ratio in equation (2.35), changes with the phase current of the machine. Therefore the air gap function of the segmented-pole SynRM is current dependant. Finally to calculate the additional air gap length, $l_{fb-CRGO}$, (2.36) is added to (2.23) to incorporate the CRGO steel properties in the air gap function of the segmented-pole SynRM:

$$l_{fb-CRGO} = \left[\left(\frac{\varphi_{SynRM}}{\varphi_{CRGO-SynRM}}\right) - 1\right] \times l_g + \left[\left(\frac{\varphi_{SynRM}}{\varphi_{CRGO-SynRM}}\right) - 1\right] \times l_{fb} \qquad (2.36)$$

Fig. 2-21 shows the air gap function of the segmented-pole SynRM in comparison with the air gap function of the SynRM presented earlier in this chapter for 12 A phase current magnitude.

The lower permeability of the CRGO steel under perpendicular field excitation reduces the q-axis flux which is shown as a higher air gap function along the q-axis of the rotor. Thus the value of $\varphi_{CRGO-SynRM}$ is chosen based on the permeability curve of the CRGO steel when it is exposed to a magnetic field perpendicular to its rolling direction (bottom curve in Fig. 2-19). In Fig. 2-21 the air gap function of the segmented-pole SynRM with CRGO steel is compared with the air gap function of the regular SynRM made of CRNGO steel when the magnetic flux density value in both steels is 1.4 T. The higher value of the air gap function of the segmented-pole SynRM shows its capability in reducing the q-axis air gap flux, resulting in an improved saliency ratio value.
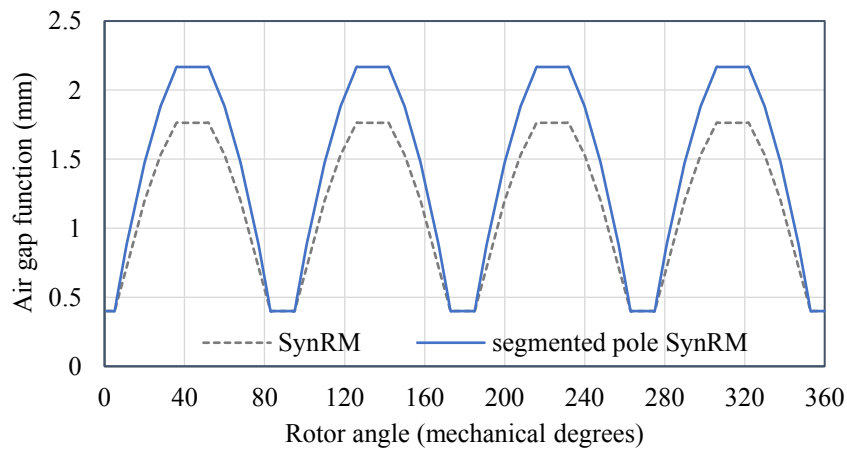
Fig. 2-21 The air gap function of the conventional SynRM, and the segmented-pole SynRM with CRGO steel

2.5.3. The FEA Model

Each rotor lamination of the segmented-pole SynRM is divided into four pieces as shown in Fig. 2-20, each section with the rolling direction parallel to the d-axis flux path of the machine. In the FEA model also the rotor is divided into four sections as shown in Fig. 2-22 (a). Two BH curves, one representing the steel characteristics with a field parallel to the rolling direction of the steel and the other depicting the steel characteristics under perpendicular field excitation, obtained from the DONART test bench are assigned to a new material defined in the material database of the software. These two curves are presented in Fig. 2-22 (b). As seen in Fig. 2-22 (b) to achieve the same magnetic flux density in the steel with a field perpendicular to the rolling direction, a larger magnetic field is required when compared to the case where the field is parallel to the rolling direction of the steel. Therefore along the q-axis of the machine a larger stator field is required in order to create the q-axis flux component.

Using the steel material imported to the software database, the torque-angle curves and the torque waveform of the segmented-pole SynRM are obtained. Fig. 2-23 (a) compares the torque waveform of the segmented-pole SynRM and the SynRM for the same operating condition of the curves in Fig. 2-14 obtained from FEA simulation. Fig. 2-23 (b) shows the same results obtained from the analytical model.

(a)   (b)
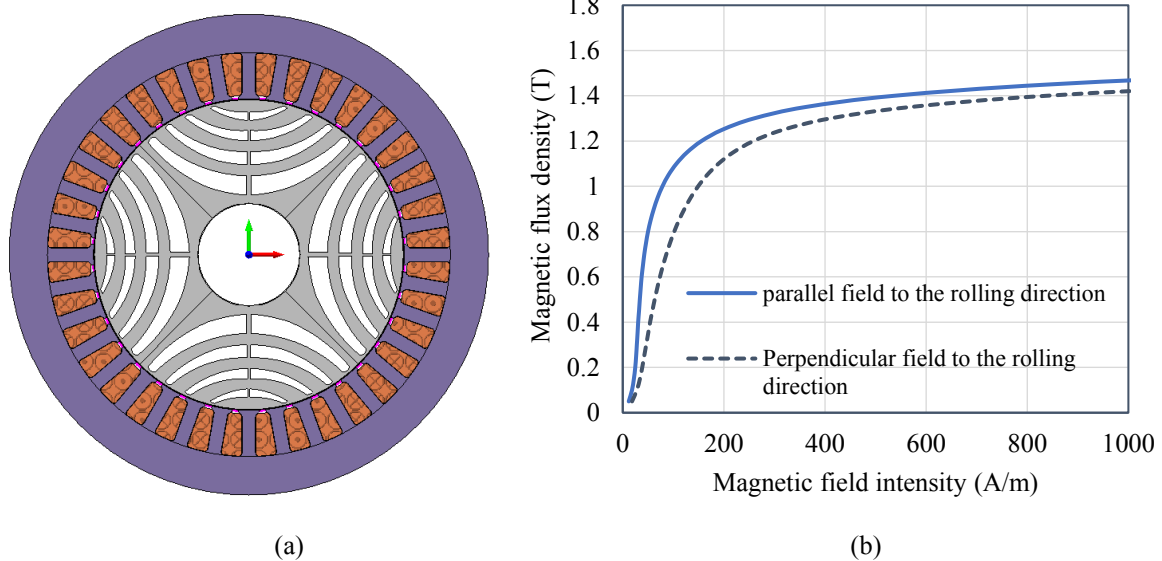
Fig. 2-22 (a) The FEA model of the segmented-pole SynRM implemented in MagNet FEA software; (b) The BH curve of the CRGO steel when the field is parallel to the rolling direction of the steel (soft axis) and when the field is perpendicular to the rolling direction

The average value of the torque waveform of the SynRM from FEA simulation is 27.6 Nm while the average value of the torque of the segmented-pole SynRM is 27.7 Nm. The torque ripple of the segmented-pole SynRM and the SynRM are 46 percent and 34 percent, respectively. The average value of the torque waveform obtained from the analytical model for the segmented-pole SynRM is 28.1 Nm with 26 percent ripple, while the average torque of the regular SynRM is 27.8 Nm with 19 percent torque ripple.
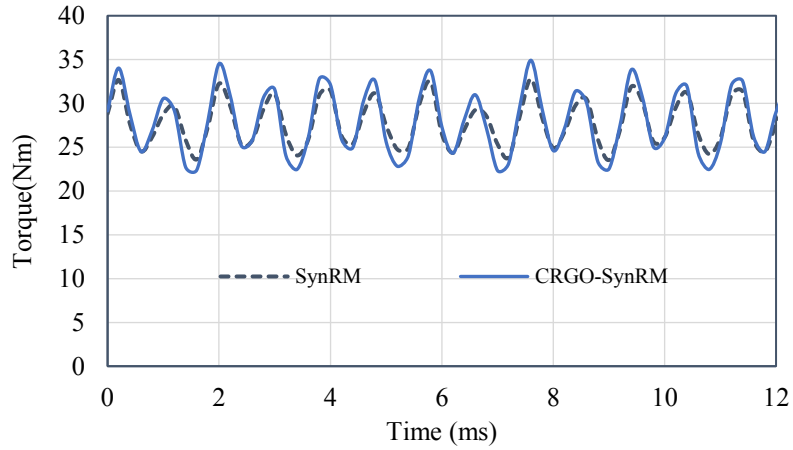
(a)
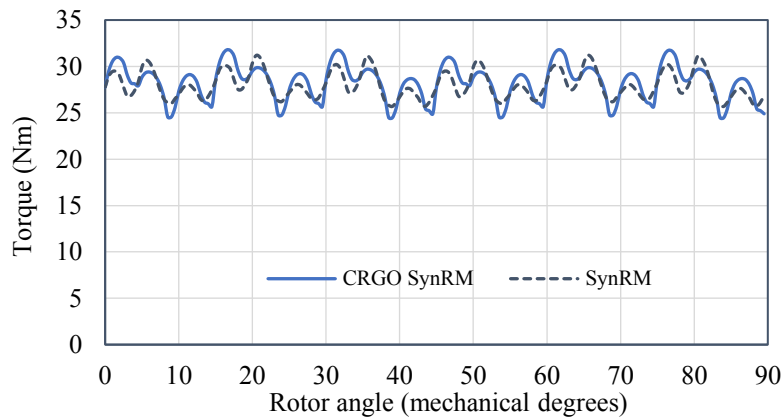
(b)

Fig. 2-23 Torque waveform comparison of the SynRM and the segmented-pole SynRM for 12 A line rms current and load angle of 23 degrees; (a) FEA simulation results; (b) analytical model results

2.5.4. Results and Comparison

Using the proposed air gap function in Fig. 2-24 and based on the coenergy equation for electromagnetic torque calculation (equation (2.27)), the torque-angle curves of the segmented-pole SynRM are obtained and compared with the obtained results from FEA

simulation and measurement. The torque-angle curves of the segmented-pole SynRM are also compared with the torque-angle curves of the regular SynRM made of CRNGO steel sheets. Fig. 2-24 (a) shows the torque-angle curve of the segmented-pole SynRM and the regular SynRM obtained from measurements for 8 A, 12 A, and 16 A phase current. Fig. 2-24 (b) compares the FEA analytical model results with FEA simulation results using MagNet®, and experimental results for the segmented-pole SynRM for 16 A phase current.
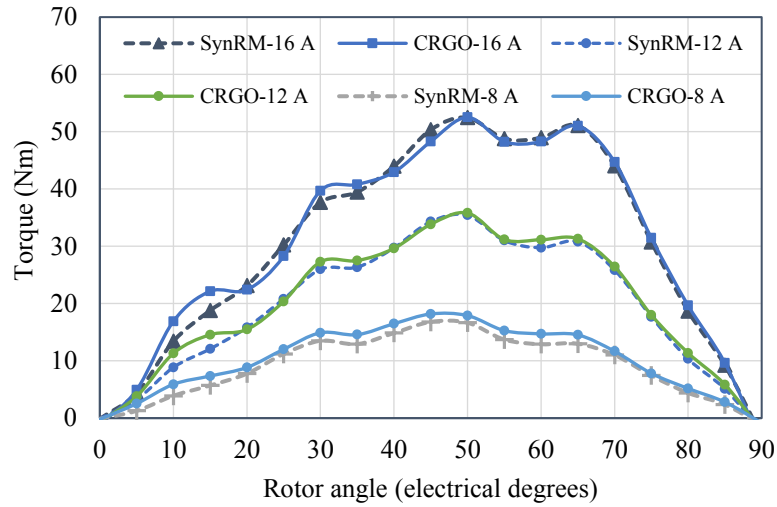
(a)
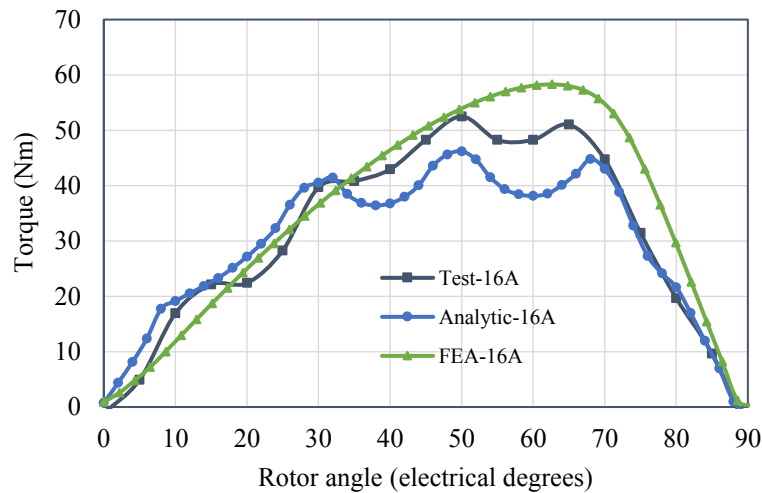
(b)

Fig. 2-24 (a) The torque-angle curves of the regular SynRM and the segmented-pole SynRM obtained from measurement; (b) FEA, analytical model, and measurement results comparison

In the FEA simulation the values of magnetic flux density and magnetic field intensity obtained from DONART test bench for the CRGO steel is used to define the steel type M5. Fig. 2-25 Shows the magnetic flux density distribution through steel lamination for the regular and segmented-pole SynRM in the same loading condition (12 A line rms current). It can be seen that despite the similar loading and operating condition, the segmented-pole SynRM made of CRGO steel is capable of operating at a higher magnetic flux density value.

(a)   (b)
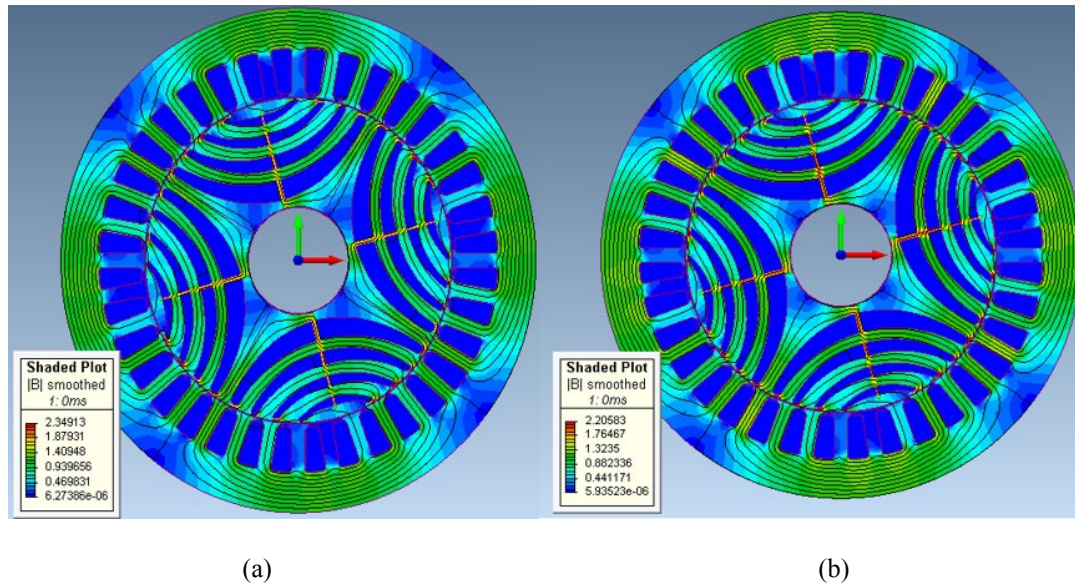
Fig. 2-25 Magnetic flux density distribution (a) segmented-pole SynRM; (b) regular SynRM

Although the segmented-pole SynRM made of CRGO steel sheets shows a relatively higher magnetic flux density in comparison with the regular SynRM made of CRNGO steel sheets (see Fig. 2-19), the observed improvement in torque production capability of the segmented-pole SynRM is not significant. This observation can be explained from two aspects:

- The permeability of steel at high magnetic flux densities
- The direction of flux path in rotor segments

Since the operating point of the steel lamination in both regular SynRM and segmented-pole SynRM is at high magnetic flux densities (above 1.4 T for rated condition and even below rated condition for most sections of the rotor lamination), the difference between the permeability values of CRGO and CRNGO steel is negligible. For example at 1.4 T the permeability of the CRNGO steel is 1619, while the permeability of the CRGO steel in rolling direction and perpendicular to the rolling direction are 2080 and 1332, respectively. This

difference further reduces as the magnetic flux density in the steel increases. Therefore it is not possible to fully utilize the high permeability of CRGO in the rolling direction, and its reduced permeability perpendicular to the rolling direction for q-axis flux reduction, at high magnetic flux density values. To avoid this problem the rotor design must be modified in a manner to avoid core saturation under rated operating condition.

The other issue as stated originates from the direction of the flux path in each segment. The application of CRGO steel in each rotor section with the rolling direction parallel to the d-axis flux path aides the saliency ratio of the SynRM if the d-axis flux is in the same direction as the rolling direction of the steel. However if the flux path is observed carefully in each rotor pole, it can be seen that the assumption is not true (see Fig. 2-25). Therefore in some parts of the rotor pole closer to the outer diameter of the rotor lamination, the flux is not parallel to the rolling direction of the steel which means that the capability of the CRGO steel cannot be fully utilized.

To fully use the advantages of the CRGO steel in a SynRM, the geometric design parameters of the SynRM must be modified. This includes both the value of the magnetic flux density in the rotor and the shape of the flux barriers. A modified segmented-pole SynRM is presented in the following section to address the limitations of the segmented-pole SynRM.

2.5.5. Modified Design of the Segmented-Pole SynRM

The proposed analytical approach for modeling and analysis of the segmented-pole SynRM provides an insight to the magnetic performance of the machine. Based on the proposed analysis it is observed that the application of the CRGO steel in the segmented-pole SynRM limits the q-axis flux, resulting in a low q-axis inductance, and a higher saliency ratio. Fig. 2-26 compares the d-axis and q-axis inductances of the regular SynRM and the segmented-pole SynRM obtained from measurements.

However CRGO steel laminations have better performance at lower current magnitudes and thus lower flux density values, since as the current magnitude increases, the difference between the relative permeability of the CRGO steel and the CRNGO steel reduces significantly (see Fig. 2-19). Therefore to fully utilize the capability of the CRGO steel in the segmented-pole SynRM, the operating point of the steel core must be maintained between 0.6 T to 1 T (see Fig. 2-19).
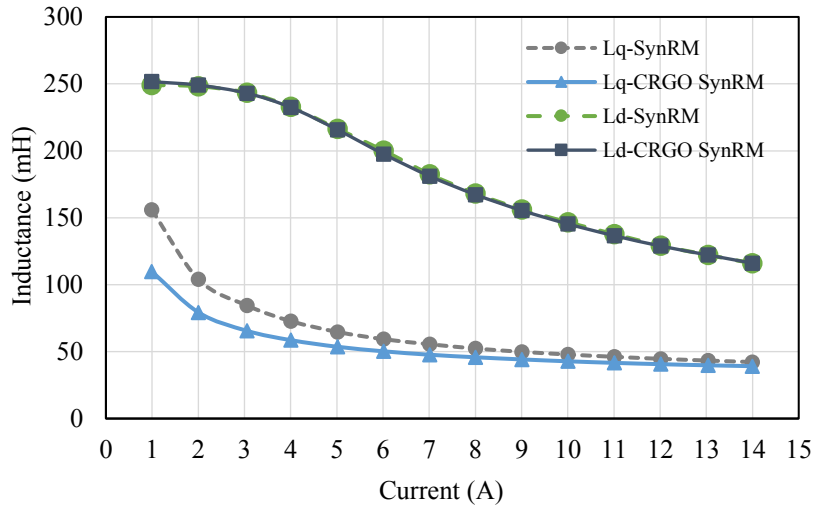
Fig. 2-26 d-axis and q-axis inductances of the regular SynRM and the segmented-pole SynRM obtained from measurements

The influence of the CRGO steel on saliency ratio improvement of the SynRM can be enhanced through design modifications using the proposed analytical model. In the analyzed segmented-pole SynRM in this chapter, the effect of the flux barriers are dominant when compared to the effect of the CRGO steel. Thus the steel permeability does not have a significant impact on the torque produced by the machine. Therefore specifically at higher current magnitudes due to the rotor core saturation, the effectiveness of the CRGO steel in saliency ratio improvement of the SynRM reduces significantly. Fig. 2-27 shows the torque-angle curve of the SynRM, and the segmented-pole SynRM at 20 A phase rms current obtained from the FEA simulation. As observed from this figure, and previously shown in Fig. 2-24, the peak torque of the SynRM and the segmented-pole SynRM are almost the same.
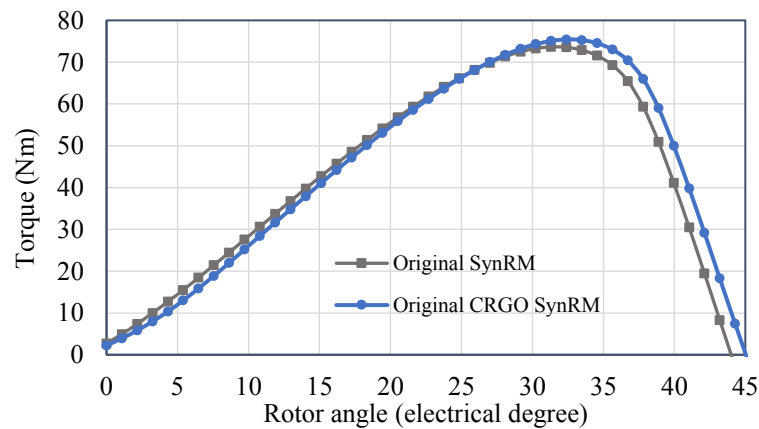
Fig. 2-27 Torque-angle curve of the original SynRM and the original segmented-pole SynRM

To benefit from the superior magnetic properties of the CRGO steel, the rotor topology must be changed. The aim of this rotor modification is to mitigate the core saturation at rated current and to provide a *d*-axis flux path parallel to the rolling direction of the steel for most rotor sections. Thus considering the same rotor outer diameter as the original SynRM, the widths of the flux barriers should reduce. However as the flux barriers' widths reduce the torque production capability of the machine reduces due to saliency reduction.

In order to avoid the rotor core saturation, the number of flux barriers is reduced to three. Their shapes are also modified in a manner to provide a path for the stator flux, parallel to the steel rolling direction. Fig. 2-28 (a) shows the modified rotor structure. Fig. 2-28 (b) compares the torque-angle curve of the modified SynRM, and the Modified segmented-pole SynRM. The reduced torque due to the smaller overall flux barrier width is compensated with the magnetic properties of the CRGO steel. However when compared to the original SynRM topology, the modified design of the SynRM does not provide a significant improvement in torque.

(a)

(b)
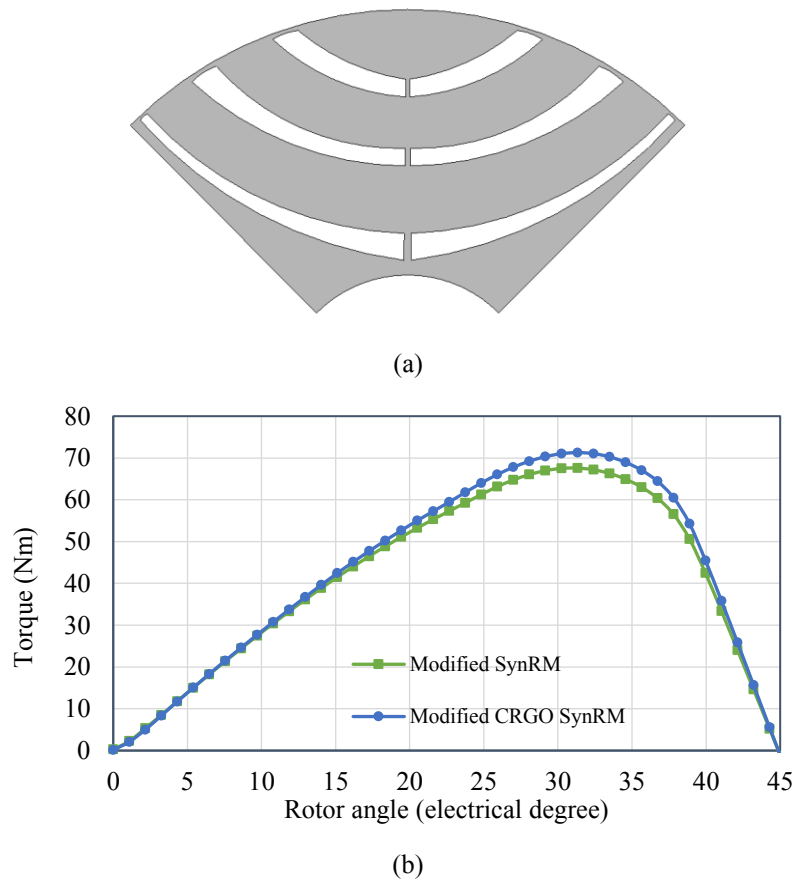
Fig. 2-28 Torque-angle curve of the modified SynRM and the modified segmented-pole SynRM

Although the effectiveness of the CRGO steel on the torque production capability of the modified segmented-pole SynRM is evident, the peak torque of the modified SynRM (with CRGO steel and with CRNGO steel) is less than the original segmented-pole SynRM. This is due to dominant impact of the flux barriers in comparison with the steel permeability. Therefore the effectiveness of the CRGO property comes at the cost of peak torque reduction.

2.6. Summary of the Chapter

In this chapter an analytical method based on the parameters of a previously designed and prototyped SynRM was developed. This analytical method usually known as the winding function method, has been used for analysis, and design of various types of electrical machines. However due to the complexity of the magnetic properties of the SynRM rotor, this model has not been used for design and analysis of this type of electrical machine. In this chapter a mathematical method to model the effect of the flux barriers in a TLA SynRM rotor was proposed. Using this mathematical approach, the main features of the flux barriers; that is, their widths, and their coverage span can be modeled. Once the air gap function of the machine based on the flux barriers' structures, and the winding function of the machine based on the winding distribution are obtained, the inductances of the machine's phases can be calculated. Using the mutual and self-inductances of the phases, the electromagnetic torque of the machine is calculated from the coenergy torque equation.

Using the proposed analytical model, the torque-angle curves of the SynRM, for various phase currents were calculated and compared with the results obtained from FEA, and measurement. The acceptable agreement of the results of the analytical model with the results of measurements, reveals the capability of the analytical model as a modeling and design tool. This model was also extended for analysis of a segmented-pole SynRM made with CRGO steel. The special magnetic features of the CRGO steel as discussed in the final section of this chapter, is incorporated in the analytical model, which results in a slight variation in the air gap function of the segmented-pole SynRM compared to the SynRM. The results of the analytical model for the segmented-pole SynRM was also compared with measurement and FEA results. It was observed that despite the superior magnetic properties of the CRGO steel, the improvement in the performance of the segmented-pole SynRM is not significant. This can

be explained by considering the flux paths in each rotor pole, and the magnetic permeability of the CRGO steel at high magnetic flux values.

The proposed analytical model which is solved in MATLAB, can be modified into a general design tool for initial sizing and performance estimation of various types of SynRMs.

Chapter 3   Design of a Permanent Magnet Assisted Synchronous Reluctance Machine

Permanent magnet assisted SynRMs (PM Assisted SynRMs) were proposed to overcome the issues and limitations of the conventional SynRMs, mainly the poor power factor and the low torque density [68]. However the fluctuating cost of the rare-earth PMs has resulted in a growing interest towards PM assisted SynRMs which utilize non-rare earth permanent magnets such as Ferrite or AlNiCo magnets. A design example of a PM assisted SynRMs with non-rare earth magnets are presented in [68, 69]. Usually the PMs are inserted in the flux barriers to saturate the iron bridges and increase the power factor [70]. Several design variations of the PM assisted SynRM are presented in this chapter. Later the design procedure is presented based on a modified version of the proposed analytical method in Chapter 2. The proposed topology is then further analyzed using FEA simulations.

3.1.   Literature Survey on Permanent Magnet Assisted Synchronous Reluctance Machines

3.1.1. Basic Operation

The presence of the permanent magnets adds another term to the electromagnetic torque equation of the SynRM, as:

$$T = \frac{3}{2}\frac{P}{2}(L_d - L_q)i_d i_q + \frac{3}{2}\frac{P}{2}\lambda_{pm}i_q \qquad (3.1)$$

Where L_d, L_q, i_d, i_q, P, and λ_{pm} are the d-axis inductance, q-axis inductance, d-axis current, q-axis current, number of poles, and the flux linkage produced by the magnets, respectively.

It also changes the dq equations of the SynRM by adding an additional term to the previously introduced equation (1.2), as:

$$v_d = R_s i_d + \frac{d\lambda_d}{dt} - \frac{P}{2}\omega_r\lambda_q + \frac{P}{2}\omega_r\lambda_{pm} \qquad (3.2)$$

The q-axis equation remains unchanged.

Design variations of PM assisted SynRMs are presented in the literature using different types of permanent magnets, with various placements, and magnetization directions. The permanent magnet contribution in torque production can also vary depending on the type and volume of the permanent magnet used in the design. Therefore the PM assisted SynRM can be designed with various ratios between the reluctance torque and the permanent magnet torque, resulting in numerous topologies.

3.1.2. Design Variations of the Permanent Magnet Assisted SynRM

The strength and the volume of the permanent magnet used in the PM assisted SynRM affects the performance of the machine significantly. Thus the permanent magnet is usually chosen and designed based on the expected magnet torque. If the permanent magnet torque contribution to the overall torque of the machine is higher than the reluctance torque contribution, the PM assisted SynRM is usually developed from an inset PM machine (IPM) or buried PM design [70], while a higher reluctance torque contribution results in a PM assisted SynRM topology. Usually the main goal behind using permanent magnet materials in a SynRM, is power factor improvement. Therefore to minimize the manufacturing cost and maintain the fault tolerant property of the SynRM while achieving an improved power factor and torque production capability, the amount of the permanent magnet material is less than a typical IPM. This section presents some of the design topologies proposed in the literature.

Permanent magnets can be arranged in different ways. The placement and orientation of permanent magnets define the role of the permanent magnets in the magnetic pole flux distribution.
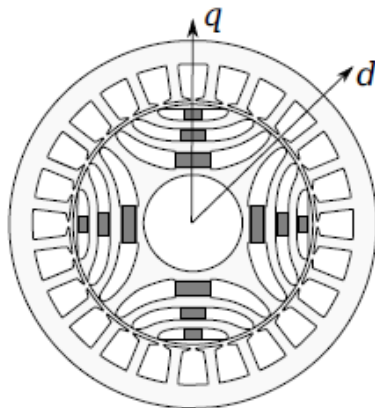
Fig. 3-1 PM assisted SynRM with PMs along the q-axis [63]

Usually permanent magnets are placed in V-shape configurations or along the *q*-axis of the SynRM. The former provides the *d*-axis flux while the latter opposes the *q*-axis flux of the stator winding with the aim of improving the saliency ratio, and the power factor of the SynRM [17]. Fig. 3-1 shows a schematic of a PM assisted SynRM, in which the magnets are placed in the *q*-axis with the aim of *q*-axis flux reduction [63].

Fig. 3-2 (a) and Fig. 3-2 (b) compare the vector diagram of a PM assisted SynRM, shown in Fig. 3-1 and a typical SynRM. It is clear from the two vector diagrams that the presence of the permanent magnets reduces the angle between the phase current and the phase voltage, thus increasing the power factor of the PM assisted SynRM, in comparison with the conventional SynRM.

<div align="center">(a)   (b)</div>
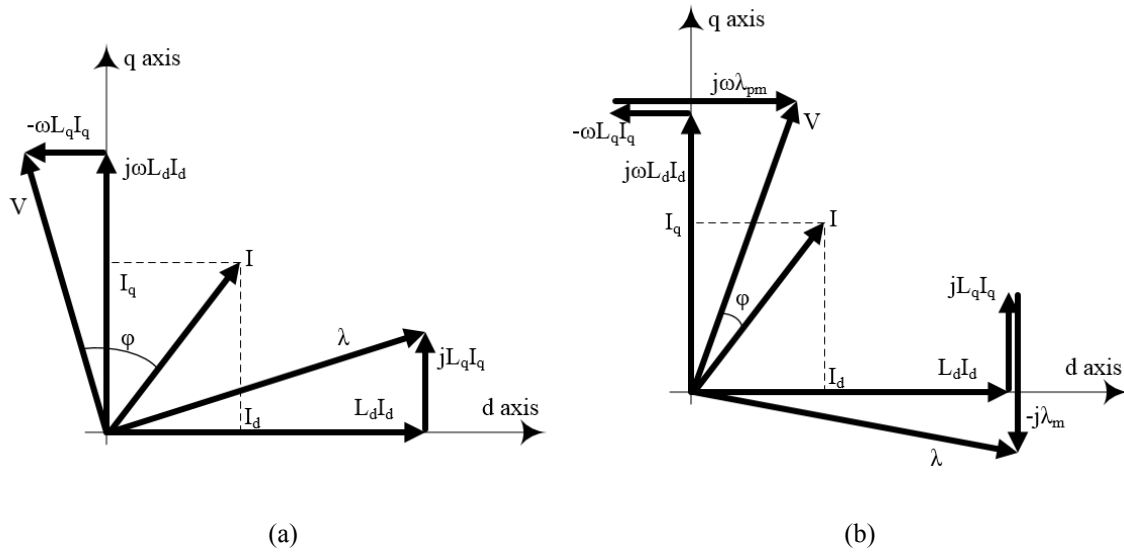
<div align="center">Fig. 3-2 (a) Vector diagram of the SynRM, (b) Vector diagram of the PM assisted SynRM</div>

The vector diagram depicted in Fig. 3-3 (b) represents a PM assisted SynRM in which the PMs are added along the *q*-axis of the machine, as shown in Fig. 3-1. The produced flux by the magnets compensates the flux linkage of the *q*-axis, $L_q i_q$. The magnet's volume affects the amount of flux compensation and must be chosen carefully.

Another variation of PM assisted SynRMs with Ferrite magnets are presented in [68] and shown in Fig. 3-3. Design optimization is performed on a benchmark interior permanent magnet machine (IPM), with rare-earth magnets, to achieve the same performance at lower cost.
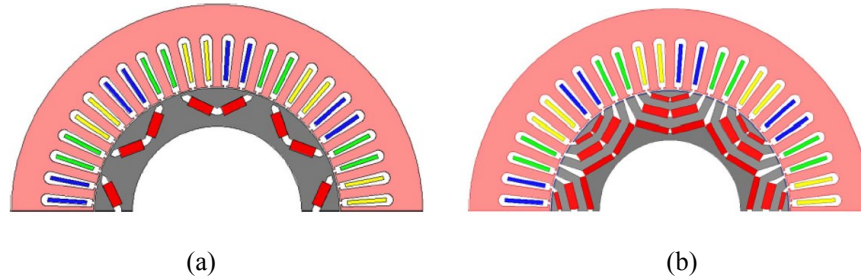
Fig. 3-3 (a) IPM with rare-earth magnets, (b) PM assisted SynRM with ferrite magnets [68]

The reluctance torque contribution to the overall torque of the IPM with rare-earth magnets is evaluated and based on the rotor geometry is modified to generate the remaining torque which is provided by the rare-earth magnets. The torque evaluation of the IPM shows that the reluctance torque is almost 50% of the overall torque of the machine. Thus to substitute the rare-earth magnets with low cost magnets such as ferrite, a larger volume of magnets and a higher saliency ratio is required, which is achieved using the rotor geometry shown in Fig. 3-3 (b). The optimized design is achieved using FEA.

Four design variations of a PM assisted SynRM similar to Fig. 3-1 are compared in [71] with the aim to maximize the back-EMF while reducing the torque ripple. In all four design topologies rectangular flux barriers are used, and the permanent magnets are placed inside the flux barriers. These four topologies are only different in the location and size of the magnets. The FEA results are analyzed and based on that the optimal design is chosen and prototyped. [72] presents a comparative study of PM assisted SynRMs and interior permanent magnet synchronous machines (IPMSM) on constant power speed range operation. Three design variations of each machine (six designs overall) are analyzed with different proportions of reluctance torque and permanent magnet torque. The paper mainly discusses the performance of these six design variations in the high speed region (beyond the base speed of the machine). This rotor topology is also classified in the same category as the one shown in Fig. 3-1. An analytical model for design and analysis of the flux barriers in a SynRM and a PM assisted SynRM is presented in [17]. A topology similar to the one shown in Fig. 3-1 is proposed which has two different adjacent poles in terms of the pole arc to pole pitch ratio, with the aim to reduce the torque ripple. Similar rotor topologies are also discussed in [73, 74, 75]. [76] proposes a new design topology for the PM assisted SynRM and compares it with a conventional design topology. It is shown that the magnet flux utilization in the conventional

topology of PM assisted SynRMs where the magnets are placed in flux barriers, is low. The proposed design incorporates the advantages of the surface mounted PM machine and the SynRM to fully utilize the magnet capacity. [77] compares the results obtained from various experiments carried out on different SynRMs with different rotor geometries. The comparison is also done amongst various SynRMs and PM assisted SynRMs using ferrite magnets. The ferrite magnets are placed in the rotor flux barriers and magnetized in the direction of the q-axis of the SynRM with the aim to oppose the q-axis flux of the SynRM. [78] studies the possibility of substituting conventional rare-earth permanent magnets in interior PM machines (IPM) with ferrite magnets, magnetized in the q-axis direction of the SynRM. Different combinations of stator tooth number and poles are also studied. An analytical design of a ferrite PM assisted SynRM is presented in [69] with the aim to reduce the torque ripple of the machine. Two machines with different numbers of flux barriers with and without permanent magnets are studied using an analytical model. The magnetization direction of the permanent magnets in both designs, opposes the q-axis flux of the SynRM. The design of a low cost PM assisted SynRM using ferrite magnets is presented in [79]. In all the above mentioned papers the magnetization direction of the PMs is in a manner to oppose the q-axis flux produced by the stator. Other PM assisted rotor topologies with V-shape magnet arrangements similar to the ones shown in Fig. 3-3 are also presented in [80, 81].

The two main topologies (Fig. 3-1 and Fig. 3-3) presented in this section show the application of permanent magnets to enhance output torque and power factor of the SynRM. A design variation of PM assisted SynRM with AlNiCo magnets is proposed in this thesis. Initially the magnet sizing is performed using the proposed analytical model presented in Chapter 2. The FEA simulation is performed on the proposed topology and the results are presented.

3.2. The Analytical Model of the Permanent Magnet Assisted SynRM

The PM assisted SynRM is designed based on the benchmark SynRM presented in [67], and the previous chapter. Therefore the stator of the SynRM is also used for the PM assisted SynRM, while the rotor is slightly modified. The main rotor dimensions such as the outer diameter, shaft diameter, as well as the core material are unchanged, however the rotor laminations are modified to provide the required space for inserting the permanent magnets.

The machine's performance is highly dependent on the type and volume of the permanent magnet used. However to minimize the manufacturing cost in the designed PM assisted SynRM, low cost permanent magnets are used. In this section the proposed rotor topology is presented first, then different permanent magnet material characteristics are introduced, and based on that the magnet type is chosen. Magnet sizing is done using the modified analytical model which is originally developed for modeling and characterization of the base SynRM and presented in Chapter 2.

3.2.1. Rotor Topology

In a PM assisted SynRM permanent magnet materials are inserted in the rotor flux barriers to enhance the performance of the machine. The output characteristic improvement depends on the type and volume of the magnets and can vary depending on the application requirements. The magnetization direction of the PMs and their placement can be done in several ways as shown in the previous section.

A design variation of PM assisted SynRMs is proposed here. The rotor magnets are placed radially with magnetization direction along the *d*-axis flux of the SynRM (shown in Fig. 3-4). Therefore the flux produced by the magnets contributes to the SynRM *d*-axis flux. The magnetic field generated by the magnets also suppresses the *q*-axis flux, which in turn contributes to saliency ratio improvement. Fig. 3-4 shows the schematic structure of the rotor of the PM assisted SynRM. In this figure only the possible magnet location is shown. Magnet dimensions and the final placement along the *q*-axis of the machine is decided based on the analytical design procedure which is presented in this section.
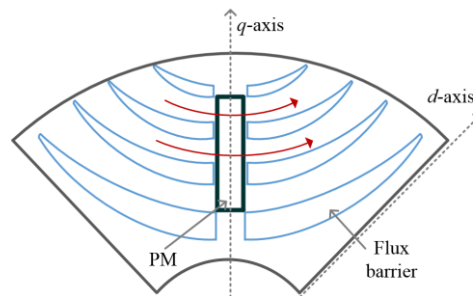
Fig. 3-4 The proposed schematic topology of the PM assisted SynRM, arrows show the magnet flux direction

The type and the magnet dimensions determine the magnitude of the PM torque, and thus the shape of the torque-angle curve of the PM assisted SynRM. The design goal is to obtain a

PM assisted SynRM in which the main component of the electromagnetic torque is provided due to the rotor saliency.

Fig. 3-5 (a), and Fig. 3-5 (b) show the torque-angle curves of a PM assisted SynRM with different values of electromagnetic torque components. In a PM assisted SynRM with a torque-angle curve similar to Fig. 3-5 (a), the second term in equation (3.1) is smaller than the first term, while in a PM assisted SynRM with a torque-angle curve depicted in Fig. 3-5 (b), the second term in equation(3.1) is larger than the first term. The ratio between the strength of the permanent magnet material and its volume, to the rotor saliency defines the shape of the torque-angle curve of the machine as shown in Fig. 3-5. Therefore it is important to study magnetic features of different permanent magnets.

(a)   (b)
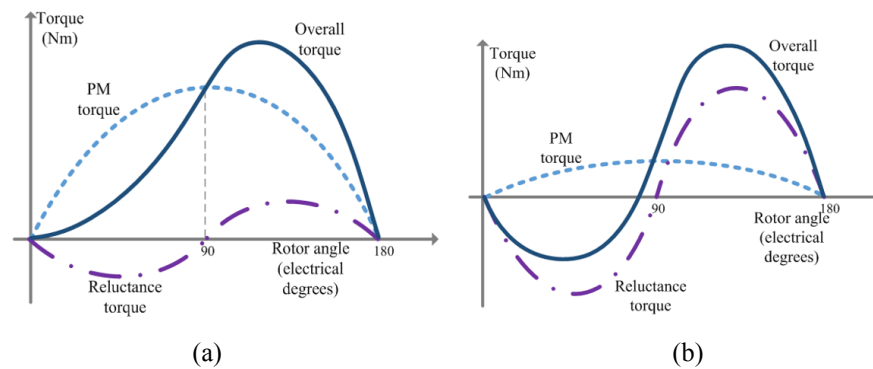
Fig. 3-5 (a) Torque components in PM assisted SynRMs, (a). High PM torque component, (b). High reluctance torque component

3.2.2. Permanent Magnet Materials

Permanent magnet materials are usually categorized based on the elements used in their chemical structure. The main groups of permanent magnet materials are:

- Rare-earth magnets (Neodymium Iron Boron (NdFeB) magnets and Samarium Cobalt (SmCo) magnets)
- AlNiCo magnets
- Ceramic magnets (Ferrites)

Permanent magnet materials are usually compared using their BH curves in the second quadrant. These curves provide the remnant magnetic flux density, and the coercive force of the permanent magnet at different operating temperatures. The operating point of the magnet, and

the maximum energy product of the magnet $(BH)_{max}$ can also be obtained using the BH curves in the second quadrant. NdFeB magnets and Samarium Cobalt magnets (SmCo) possess high remnant flux densities (B_r), and high coercive force (H_c). The high coercivity of the rare-earth magnets shows their capability in withstanding strong magnet fields. NdFeB magnets usually have a B_r value that vary between 1.06 T to 1.45 T at 20ºC, and an H_c value varying between 835.5 kA/m and 1082.2 kA/m. The $(BH)_{max}$ value of different grades of NdFeB magnets vary between 222.8 kJ/m^3 to 413.8 kJ/m^3. The remnant flux density of sintered SmCo magnets is normally between 0.82 T to 1.15 T, while the H_c varies between 565.0 kA/m to 819.6 kA/m. Despite high remnant flux density and coercivity values, the fluctuating price of rare earth magnets, and their accessibility is an important issue that reveals the necessity of searching for a substituting PM material for electrical machine applications. Another category of permanent magnet materials known as AlNiCo magnets have relatively high remnant flux similar to NdFeB magnets. However AlNiCo magnets can easily lose their magnetic capability due to their low coercivity. The B_r and H_c values for various types of AlNiCo magnets ranges between 0.72 T to 1.3 T, and 47.7 kA/m to 131.3 kA/m, respectively. Although the remnant flux density of AlNiCo magnets are comparable to rare-earth magnets, the low coercive force values is the challenging factor if AlNiCo magnets are to be used in electrical machines. The $(BH)_{max}$ value of AlNiCo magnets vary between 30.2 kJ/m^3 to 71.6 kJ/m^3. Amongst AlNiCo magnets, AlNiCo 9 magnet possess higher values of coercive force. Therefore it is a more suitable choice for electrical machines. The design of electrical machines based on AlNiCo magnets requires special care to ensure the safe operation of the permanent magnet avoiding the unwanted loss of the permanent magnet capability. The possibility of magnetizing the magnet in a case when the magnet is demagnetized must also be considered. In this design procedure AlNiCo 9 magnets is chosen for the PM assisted SynRM. Table. 3-1 compares several AlNiCo magnets.

Table. 3-1 Various AlNiCo magnets

Material	B_r (T)	H_c (kA/m)	$(BH)_{max}$ (kJ/m^3)
AlNiCo 5 (AlNiCo5-LNG34)	1.1	50	34
AlNiCo 5 (AlNiCo5-LNG40)	1.2	50	40
AlNiCo 6 (AlNiCo6-LNG28)	1.15	58	28
AlNiCo 8 (AlNiCo8-LNGT44)	0.9	115	44
AlNiCo 9 (AlNiCo9-LNGT72)	1.05	115	72
AlNiCo 9 (AlNiCo9-LNGT80)	1.08	120	80

Equation (3.3) is a linear demonstration of the possible operating points of a permanent magnet based on its B_r value, and relative permeability:

$$B_m = B_r + \mu_R \mu_0 H_m \tag{3.3}$$

where B_m, B_r, μ_R, μ_0, H_m are the magnetic flux density at the operating point, remnant magnet flux density of the magnet, relative permeability of the magnet, magnetic permeability of the free space, and the magnetic field intensity at the operating point. Although this equation can be applicable to rare-earth magnets since their BH characteristics is linear to a good approximation, for AlNiCo magnets this equation is only applicable to the right of the knee region of the magnet as shown in Fig. 3-6 (b).

The operating point of the magnet is obtained using (3.4) [82] which is defined based on the machine's dimensions:

$$P_c = \frac{-B_m}{\mu_0 H_m} = \frac{l_m A_g}{l_g A_m} = \frac{l_m}{l_g} C_\emptyset^{-1} \tag{3.4}$$

where P_c, l_m, l_g, A_g, A_m, and $C_\emptyset^{-1}$ are the permeance coefficient, magnet width, air gap length, air gap area, magnet area, and the flux concentration factor, as:

$$C_\emptyset = \frac{A_m}{A_g} \tag{3.5}$$

In a permanent magnet machine the magnet sizing is done in a manner to fully utilize the magnet capability. Therefore the operating point of the magnet is usually chosen at the point of maximum energy product (BH)$_{max}$ [82, 83]. However for permanent magnet material such as AlNiCo the nonlinear properties of the material must also be considered. If the operating point of the AlNiCo magnet is pushed beyond the knee point as a result of a strong external field, the material will lose its magnetic capability. Therefore the P_c value is chosen in a manner to ensure the operating point of the magnet to the right of the knee region as shown in Fig. 3-6 (b). Once the value of P_c is decided, the operating point of the magnet can be calculated using (3.3) for magnets with linear characteristics such as NdFeB or by referring to the magnet BH curve shown in Fig. 3-6 (a).

The BH curve of several magnet types in the second quadrant are depicted in Fig. 3-6 (a). Fig. 3-6 (b) shows the BH curve of AlNiCo 9 with different P_c lines showing various operating points. For safe operation of the magnet with low risk of demagnetization, the P_c line must intersect with the BH curve of the magnet to the right of the knee point. Therefore for the type of the magnet used in this design (AlNiCo 9) a P_c line of higher than 10 is required.

(a)   (b)
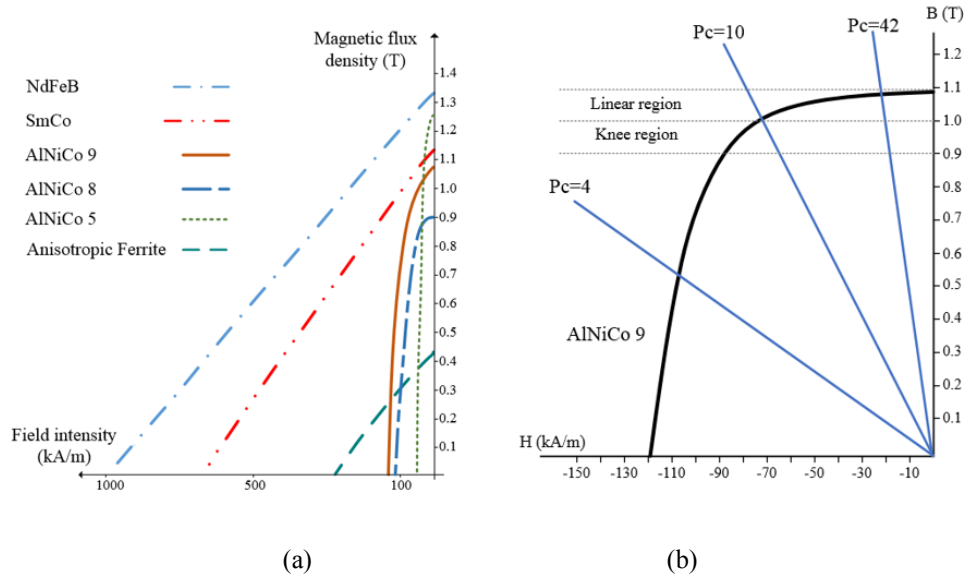
Fig. 3-6 (a) BH curve of some of the PM materials; (b) BH curve of AlNiCo 9 with different Pc lines indicating different operating points

The length of the permanent magnet (in the radial direction), is decided using the analytical model and is discussed in the next section. The width of the magnet is chosen considering the safe operation of the magnet before the knee point of the curve shown in Fig. 3-6 (b), and using (3.4).

3.2.3. The Analytical Modeling Procedure of the Permanent Magnet Assisted SynRM

The modeling procedure of the PM assisted SynRM is divided into two sections similar to the procedure used for the SynRM; the winding function of the stator, and the air gap function of the rotor. The SynRM and the PM assisted SynRM share the same stator. Thus the winding function of the two machines are similar. The air gap function is also similar. However an additional source of magnetic field is added which is the permanent magnet inside the rotor core. To model the effect of the permanent magnets the BH curve of AlNiCo 9 is considered.

70

The magnetic field intensity value at the desired operating point is selected, and used in the analytical model to calculate the magnetic flux produced by the permanent magnet. The obtained value of the magnetic flux is added to the air gap flux produced by the stator winding (considering radial and tangential components of the air gap flux). Due to the rotor geometry and placement of the magnets (Fig. 3-4), the magnetic flux produced by the permanent magnets is highly influenced by the flux barriers. Three different magnet lengths with a similar rotor topology are modeled using the proposed analytical model. The variation in the magnet length alters the air gap flux density distribution and hence affects the output performance of the machine.
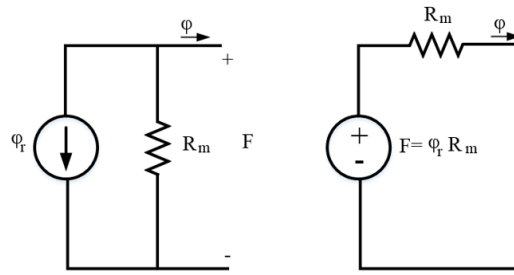
Fig. 3-7 The equivalent circuits of a permanent magnet

The permanent magnet is considered as a winding with a DC current of 1 A. Therefore the number of winding turns defines the strength of the magnet and the MMF produced by the magnet. Using the Thevinin equivalent circuit of permanent magnets [82], as shown in Fig. 3-7, the MMF produced by the magnet is calculated and used in the inductance matrix to obtain the static torque value. In this figure the R_m represents the reluctance of the permanent magnet and is calculated based on the magnet dimensions and using (2.22). φ is the portion of flux, once the leakage flux is deducted from the total permanent magnet flux φ_r. The obtained MMF value, F is used to calculate the air gap flux produced by the permanent magnet, considering the SynRM's topology. The obtained MMF which represents the number of the winding turns replacing the permanent magnet in the analytical model is used in the modified torque equation of the SynRM. Equation (3.6) shows the torque equation of a PM assisted SynRM obtained from the coenergy method:

$$T = \frac{1}{2}[I_{abc}]^T \left[\frac{\partial L_{abc}(\theta)}{\partial \theta}\right][I_{abc}] + \frac{1}{2}[I_{abc}]^T \left[\frac{\partial L_{abc-PM}(\theta)}{\partial \theta}\right][I_{PM}] \tag{3.6}$$

where L_{abc-PM}, and I_{PM} show the mutual inductance between the DC winding replacing the permanent magnet in the rotor, and the stator winding, and the current in the DC winding which is considered equal to 1 A. The first term in equation (3.6) is previously explained in equation (2.19) for a SynRM and produces the reluctance torque of the machine. The second term in equation (3.6) is the torque produced by the permanent magnets as shown in Fig. 3-5. The summation of the two terms in equation (3.6) generates the total torque of the PM assisted SynRM, T.

To calculate the mutual inductance between the DC winding of the rotor (representing the permanent magnet) and the stator winding, equation (2.25) is used. However the relative position of the two windings vary for different rotor positions and must be considered in (2.25). Three design variations with three different permanent magnet lengths are considered. These three design variations are shown in Fig. 3-8.

(a)   (b)

(c)
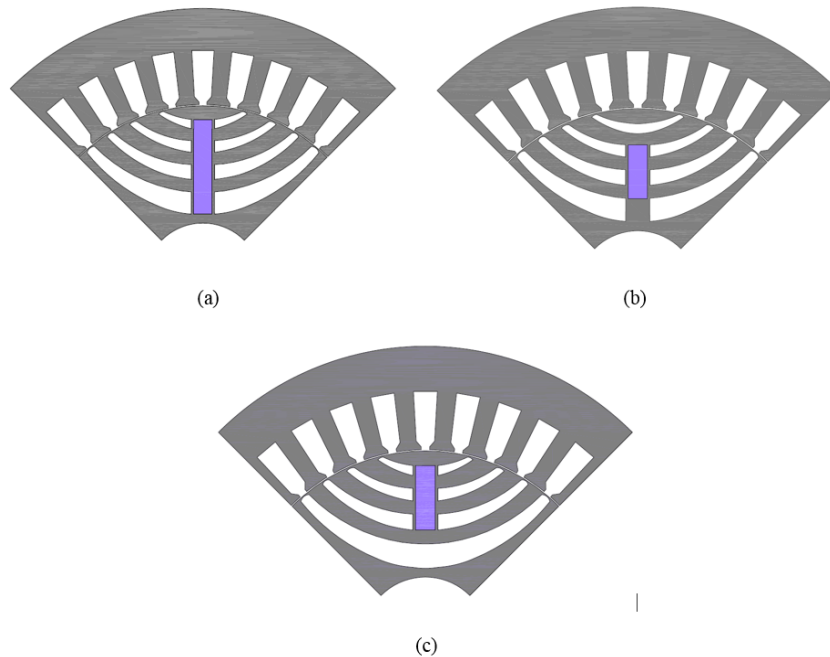
Fig. 3-8 Design variations of the PM assisted SynRM, (a) Magnet length = 36 mm (b) Magnet length = 20 mm, (c) Magnet length = 23 mm

The placement of the permanent magnet in the middle of the flux barriers distorts the magnetic field of the permanent magnet. To estimate the uneven field of the permanent magnet, an air gap function is defined based on the air gap function of the SynRM and is shown Fig. 3-9 (a).
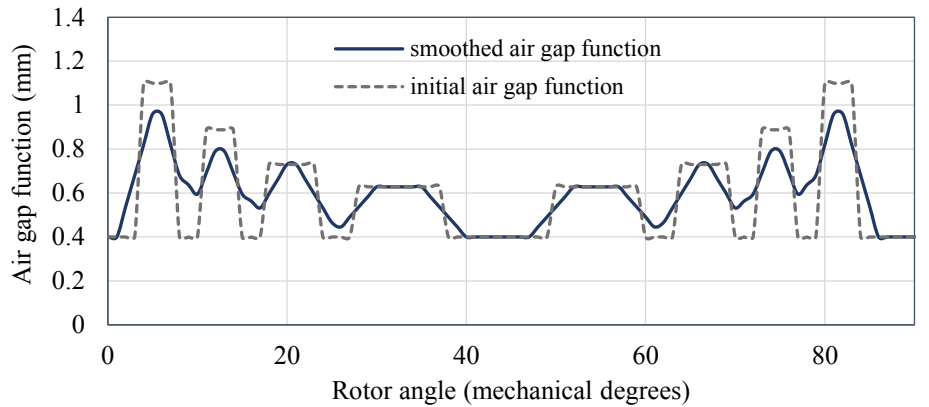
(a)
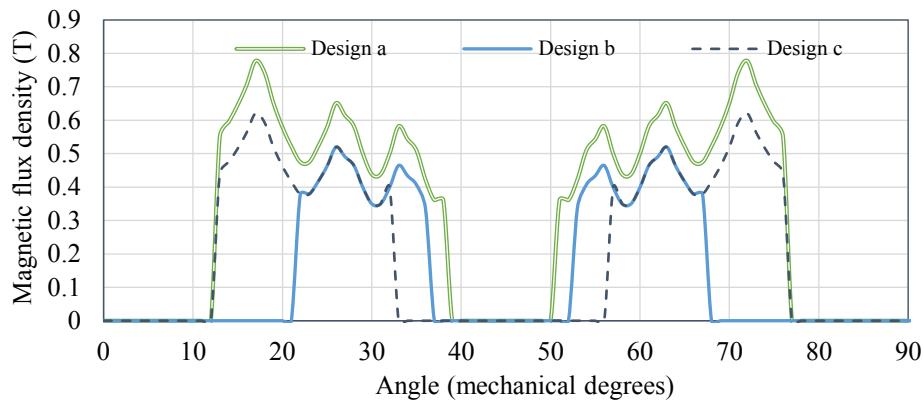
(b)

Fig. 3-9 (a) Air gap function used to model the effect of permanent magnets on the air gap magnetic flux density; (b) Air gap magnetic flux density for the three magnet lengths shown in Fig. 3-8

This air gap function is used to calculate the magnetic flux density produced by the magnet based on its operating point (H_m), and the variation in the reluctance of the rotor along the magnet length (due to the alternate air and rotor core placement). In this air gap function which is later smoothed using the smooth function in MATLAB, the transition between the flux barriers is not modeled using a straight line, unlike the air gap function used for the SynRM (Chapter 2). For the rotor angles where the flux barrier doesn't exist, the actual value of the air gap thickness is considered, and at angles with the flux barrier the additional air gap length as shown in Fig. 2-8 (a) is added to the physical air gap of the machine. Knowing H_m at the operating point of the permanent magnet and its thickness, the MMF produced by the permanent magnet is calculated using $\mathcal{F} = H_m l_m$, with l_m being the magnet thickness. Using the relationship between reluctance, and MMF, the air gap flux is obtained using the air gap function shown in Fig. 3-9 (a). Fig. 3-9 (b) shows the air gap flux density waveform produced

73

by the permanent magnet with three different lengths. The obtained waveform is for a permanent magnet with 7 mm thickness.

To obtain Fig. 3-9 (b) the length of the permanent magnet is used as an approximation for magnetic flux distribution in the air gap of the machine. Hence in the areas which are not covered by the magnet, the value of the magnetic field is assumed to be equal to zero. Therefore the estimated flux value is zero. As an example for Design c where the magnet only covers from the second bottom flux barrier to the upper most flux barrier, the magnetic flux density is equal to zero from 0 degrees up to almost 20 degrees as shown Fig. 3-9 (b). The same approximation is also applied for areas near the q-axis of the PM assisted SynRM. Due to the magnetization direction of the permanent magnet, the field intensity on the q-axis of the machine is almost zero. Thus the magnetic flux due to the permanent magnet is also assumed zero for this region.

The torque waveform of the three design variations shown in Fig. 3-8 can also be calculated similar to the torque waveform of the SynRM presented in Chapter 2. However for a PM assisted SynRM the magnetic flux of the permanent magnet is also added to the air gap flux produced by the stator winding. Once the radial and tangential components of the air gap magnetic flux is obtained equation (2.32) is used to calculate the torque. Fig. 3-10 shows the torque waveform of the three design variations shown in Fig. 3-8 for 12 A line rms current (similar to Fig. 2-14). The average value of the torque waveforms shown in Fig. 3-10 are 37.17 Nm for design a, 34.83 Nm for design b, and 33.55 Nm for design c. The obtained values are for a load angle equal to 25 degress. The improvement in the average torque value is different for different load angles amongst the three design variations.
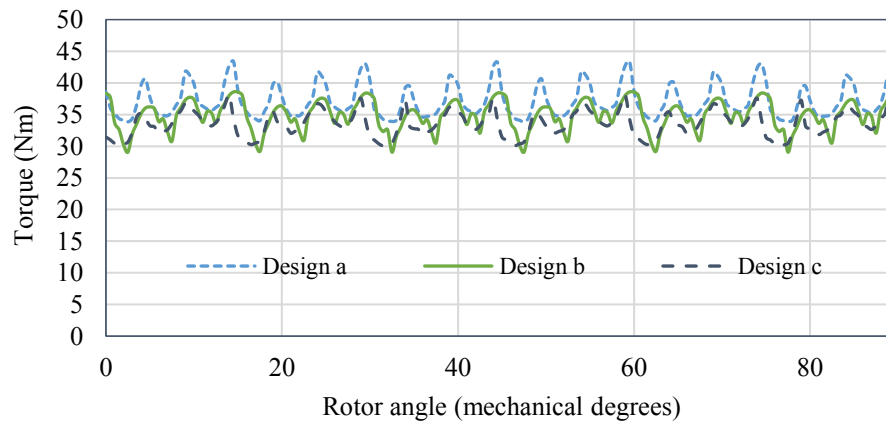
Fig. 3-10 Torque waveform comparison of Design a, Design b, and Design c

The torque-angle curves of the three design variations shown Fig. 3-8 are also compared for phase current values of 10 A and 20 A, ranging from 0 to 90 degrees electrical. Fig. 3-11 (a) shows the torque produced by the permanent magnets of the PM assisted SynRM for 20 A and 10 A for the three design variations shown in Fig. 3-8. Fig. 3-11 (b) shows the total torque of the PM assisted SynRM for 10 A and 20 A current values of the three design variations shown in Fig. 3-8.
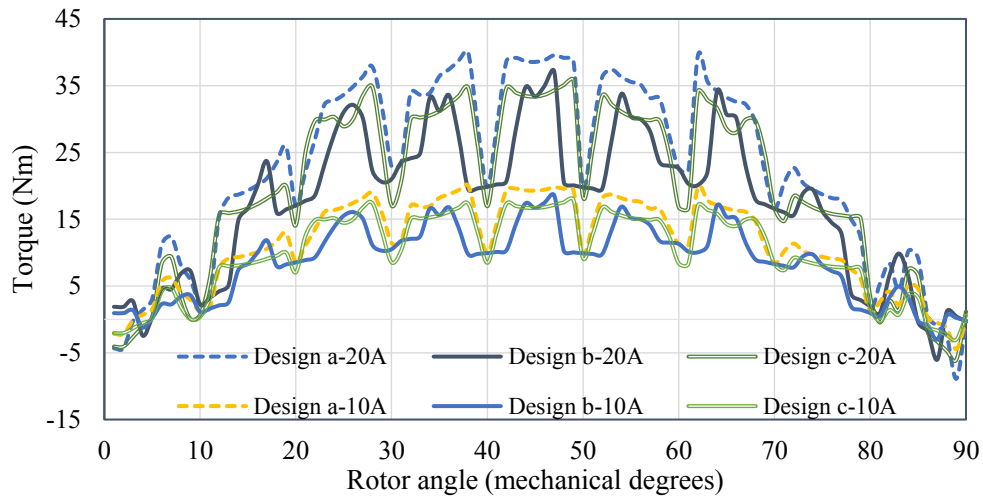
(a)
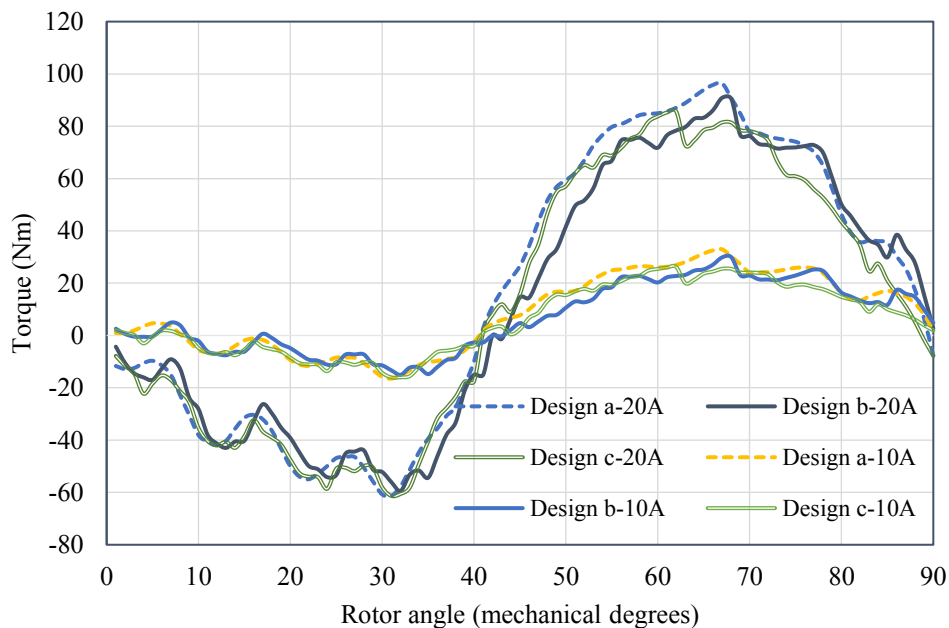
(b)

Fig. 3-11 Results of the analytical model for Design a, b, and c (a) PM torque component, (b) the overall torque

To further compare the performance of the three design variations shown in Fig. 3-8 their torque-angle curves are compared in a similar manner as discussed for the SynRM, using the coenergy method. The results of the analytical model of the PM assisted SynRM are compared with the FEA results in the following section.

3.3. Finite Element Analysis Results and Comparison

The results obtained from the analytical model for the three design variations of the PM assisted SynRM based on the previously prototyped SynRM was presented in the previous section. In that section the torque waveform of the machines for a specific loading condition was compared and the improvement in the average torque value was compared to the average value of the SynRM torque waveform. To further investigate the performance of the PM assisted SynRM, the torque-angle curves of the three PM assisted SynRM were calculated using the proposed analytical model. The results of the FEA simulations of the PM assisted SynRM are presented in this section. Initially the implementation of the machine's geometry and the utilized modeling strategies are presented. The operating point of the permanent magnet, the air gap flux density waveforms in no load condition, torque-angle curves, and the torque waveform of the machine are presented later in this section.

3.3.1. Finite Element Model and Magneto Static Analysis

To perform the FEA simulation of the PM assisted SynRM, Flux2D 11.1 is used. In this software the machine's geometry is created by defining points, and connecting these points using arcs and lines. Fig. 3-12 shows the implemented geometry in Flux for Design b (see Fig. 3-8). Each color group in the stator slots represent a different phase winding.
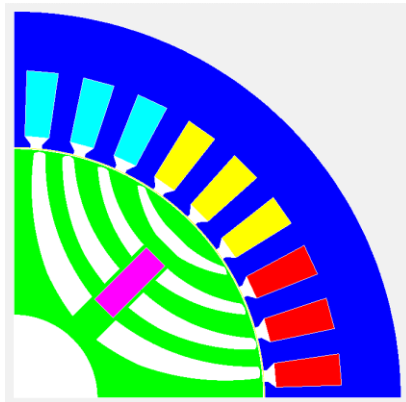
Fig. 3-12 The FEA model of Design b

In the magneto-static analysis procedure as discussed for the SynRM, a DC current is supplied to machine's phases as shown in Fig. 2-15. Therefore one of the phases is supplied with the full current magnitude while half the current passes through the other two phases. While the supply is maintained constant the rotor is rotated in steps of 1 degree, until one complete cycle (90 degrees mechanical for PM assisted SynRM) is covered.
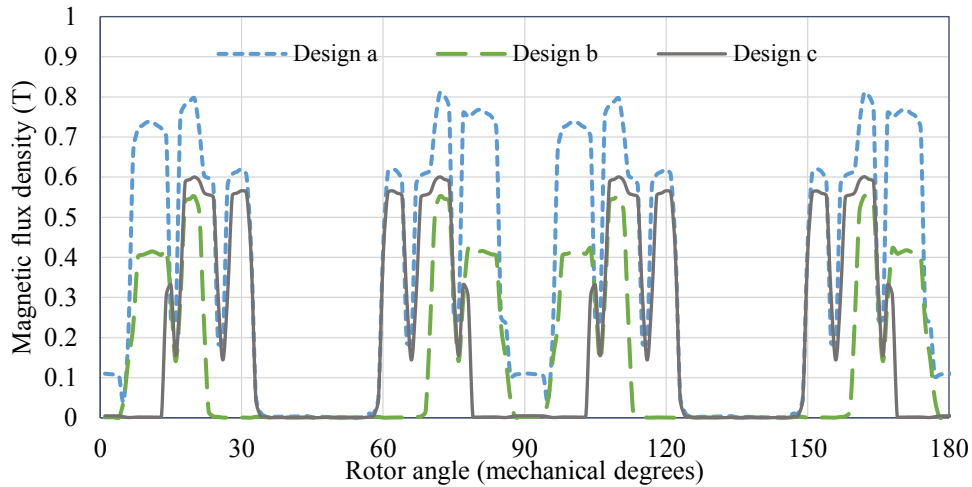
(a)
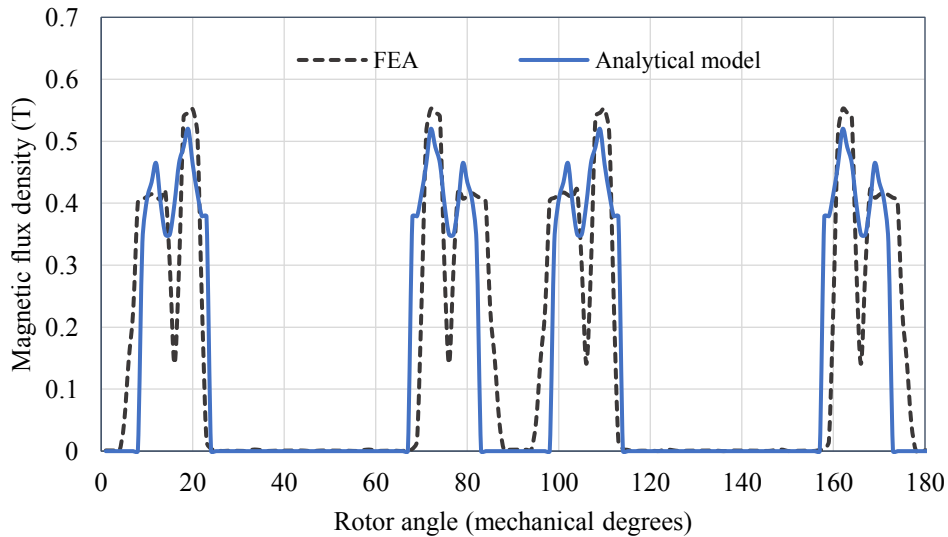
(b)

Fig. 3-13 Air gap flux density distribution of the three design variations with different magnet lengths obtained from FEA; (b) the air gap magnetic flux density comparison of Design b obtained from FEA and the analytical model

Initially the rotor is rotated at no load condition (zero stator current), and the magnetic flux density in the air gap of the machine is calculated to investigate the effect of the magnet size

on the air gap flux density distribution of the PM assisted SynRM. Fig. 3-13 (a) shows the results obtained from FEA simulations. Fig. 3-13 (b) compares the no-load air gap magnetic flux density curves obtained from FEA and the analytical model for Design b. This comparison shows the proper accuracy of the analytical model as a modeling and design tool.

The torque-angle curves of the PM assisted SynRM is also obtained using the FEA simulation for current values ranging for 4 A to 20 A in steps of 2 A, and for 90 degrees mechanical. To perform this simulation the same procedure as stated for the SynRM in the second chapter is repeated. Fig. 3-14 shows the torque-angle curves of the three design variations of the PM assisted SynRM with different magnet lengths, and magnet thickness equal to 7 mm. The effect of magnet thickness is further investigated in this section.

(a)

(b)
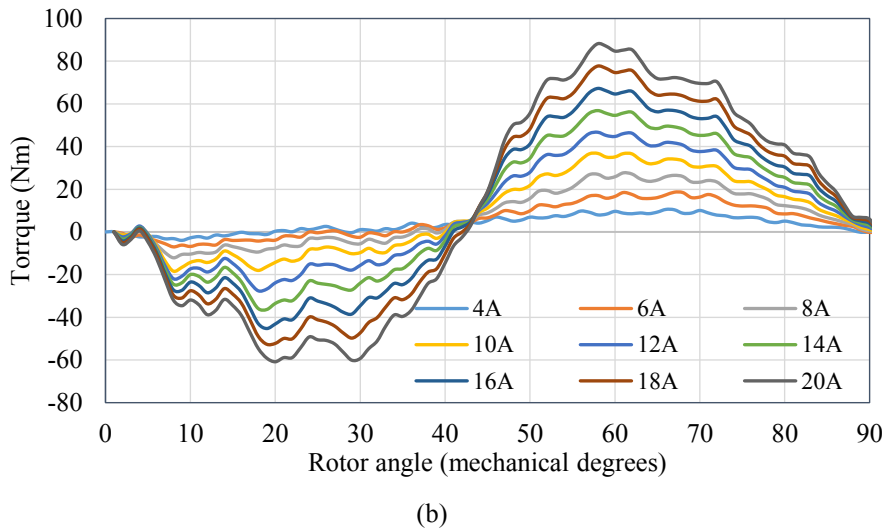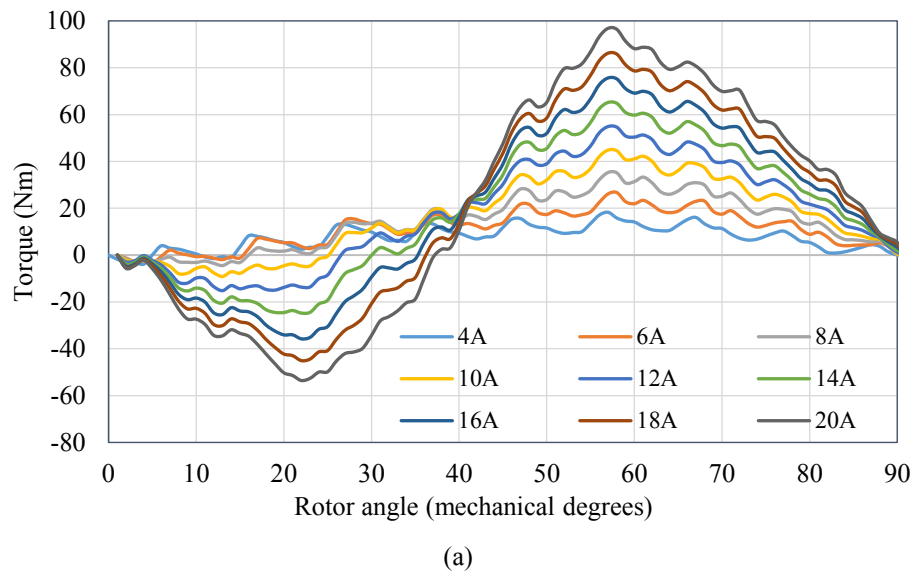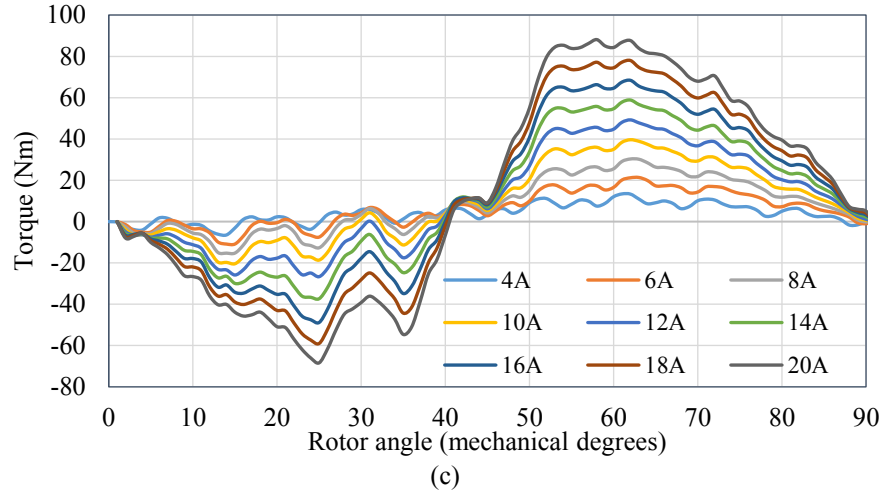
Fig. 3-14 ; (a) Design a; (b) Design b; (c) Design c

3.3.2. The Effect of Magnet Thickness on the Performance of the PM Assisted SynRM

It was shown in section 3.2.2 that the operating point of the permanent magnet is highly affected by its dimensions. It was also discussed that for an AlNiCo magnet with the nonlinear BH curve in the second quadrant, the magnet dimensions must be chosen in a manner to ensure the safe operation of the permanent magnet before the knee point. Shifting the magnet operating point beyond the knee point results in irreversible demagnetization. Since the length of the permanent magnet is limited by the machine's dimensions (rotor radius), and affects the output characteristics of the machine (as shown in Fig. 3-14), the operating point of the permanent magnet is adjusted by varying its thickness. A small permanent magnet thickness increases the risk of magnet demagnetization in large stator fields, while a large magnet thickness decreases the d-axis inductance of the machine, thus resulting in reluctance torque reduction. Therefore it is of great importance to choose the proper magnet dimensions.

To examine the effect of magnet thickness on the performance of the PM assisted SynRM, and study the operating point of the permanent magnet with respect to its dimensions, five values for magnet thickness are assigned to each of the design variations shown in Fig. 3-8. Table. 3-2 shows the obtained operating point of the magnet for Design a, b, and c, and for magnet thicknesses varying from 4 mm to 8 mm calculated using equations (3.3) to (3.5).

It was shown in the previous section that a safe operation of the AlNiCo 9 magnet, with a BH curve as depicted in Fig. 3-6 (b) requires a Pc line of 10 or higher. Although all the

operating points listed in Table. 3-2 satisfy the above-mentioned condition, a higher Pc line is necessary to avoid the unwanted demagnetization of the permanent magnet. Therefore higher values of P_c are preferred. However a high P_c line value results in an operating point with a smaller energy density which means that the capability of the permanent magnet will not be fully utilized. Thus a thickness of 8 mm for Design a, 7 mm or 8 mm for Design b, and 7 mm or 8 mm for Design c, will be proper choices regarding each design to ensure a magnet operating point before the knee point of the BH curve. To study the effect of the magnet thickness on the output characteristics of the PM assisted SynRM, the torque-angle curves of the three design variations for 16 A are calculated with various magnet thicknesses and compared with the torque-angle of the SynRM for the same current value.

Table. 3-2 The operating point of the permanent magnet for different magnet thicknesses

	Magnet thickness (mm)	P_c	B_m(T)	H_m(A/m)
Design a	4	12.99	0.97	-59600
	5	16.24	0.98	-48350
	6	19.49	0.98	-40400
	7	22.74	0.99	-34850
	8	25.99	1.01	-31100
Design b	4	23.89	1.00	-33400
	5	29.86	1.01	-27150
	6	35.84	1.02	-22750
	7	41.81	1.03	-19600
	8	47.78	1.04	-17350
Design c	4	20.62	0.99	-38350
	5	25.77	1.01	-31050
	6	30.93	1.02	-26250
	7	36.09	1.02	-21450
	8	41.24	1.03	-20050
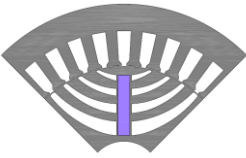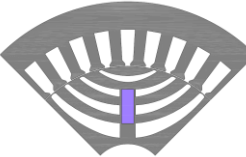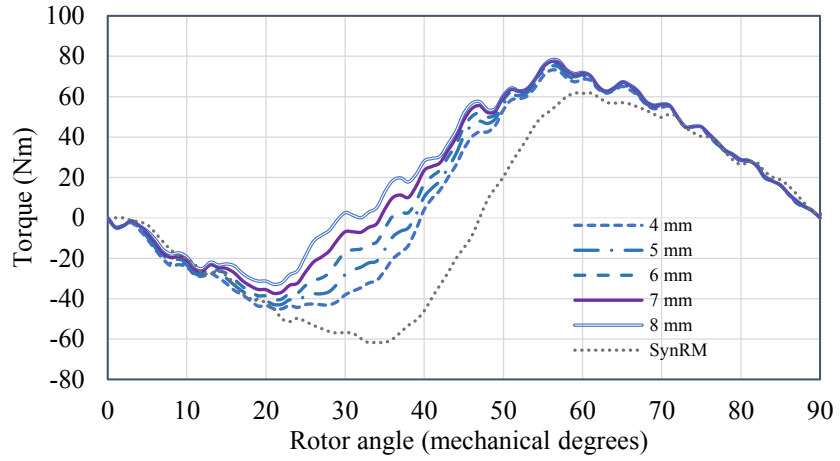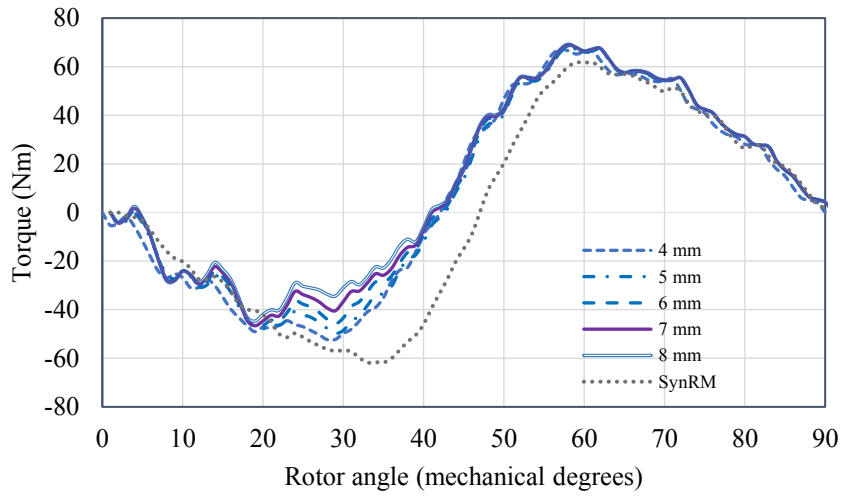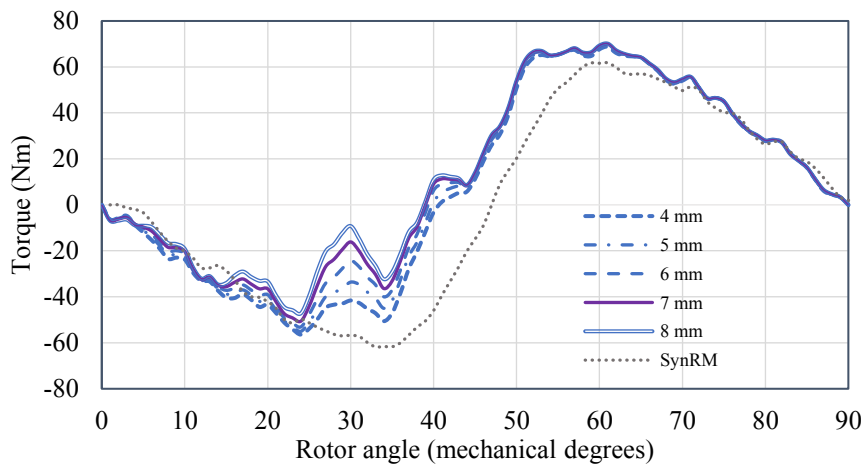
Fig. 3-15 Torque-angle curves of the PM assisted SynRM design variations for different magnet thicknesses;

(a) Design a; (b) Design b; (c) Design c

These curves are shown in Fig. 3-15. It is observed that the magnet thickness does not affect the torque production capability of the machine, significantly. All three design variations show improvement when compared to the SynRM, with Design a possessing the highest value of the produced torque.

The field distribution on the magnet in no-load, and full load conditions are also studied using FEA. The importance of this analysis is in identifying the exact operating point of the magnet in different loading conditions, and studying the possibility of magnet demagnetization. A hypothetical line is considered along the magnet length. The tangential and normal components of the magnetic field intensity, and magnetic flux density are calculated in no-load and full-load conditions. The effect of the q-axis flux produced by the stator winding in full-load condition on the magnet operating point is studied using the perpendicular component of the magnetic flux density and magnetic field intensity to the magnetization direction of the permanent magnet. In no-load condition (zero stator current) the field intensity and magnetic flux density are obtained along the magnet length. This study reveals the operating point of the magnet on the BH curve shown in Fig. 3-6 (b). Fig. 3-16 shows the field distribution of Design b in full-load condition. The white line shown along the magnet length in this figure represents the location of the points used for calculation of the field components.
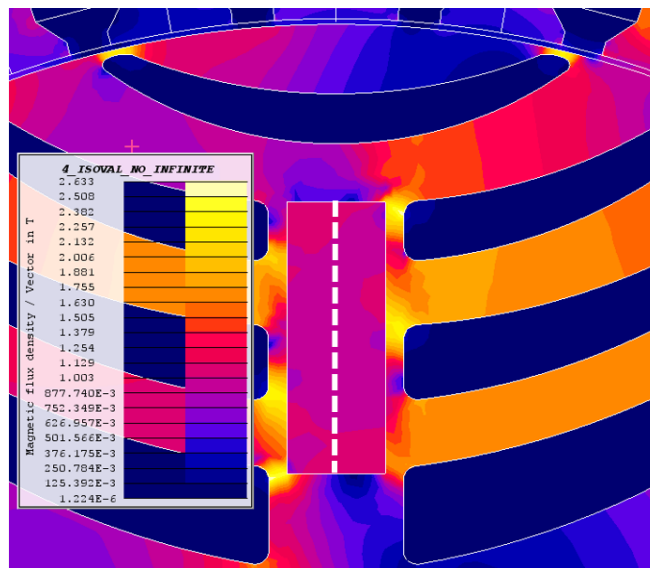
Fig. 3-16 Magnetic flux density distribution in full-load condition
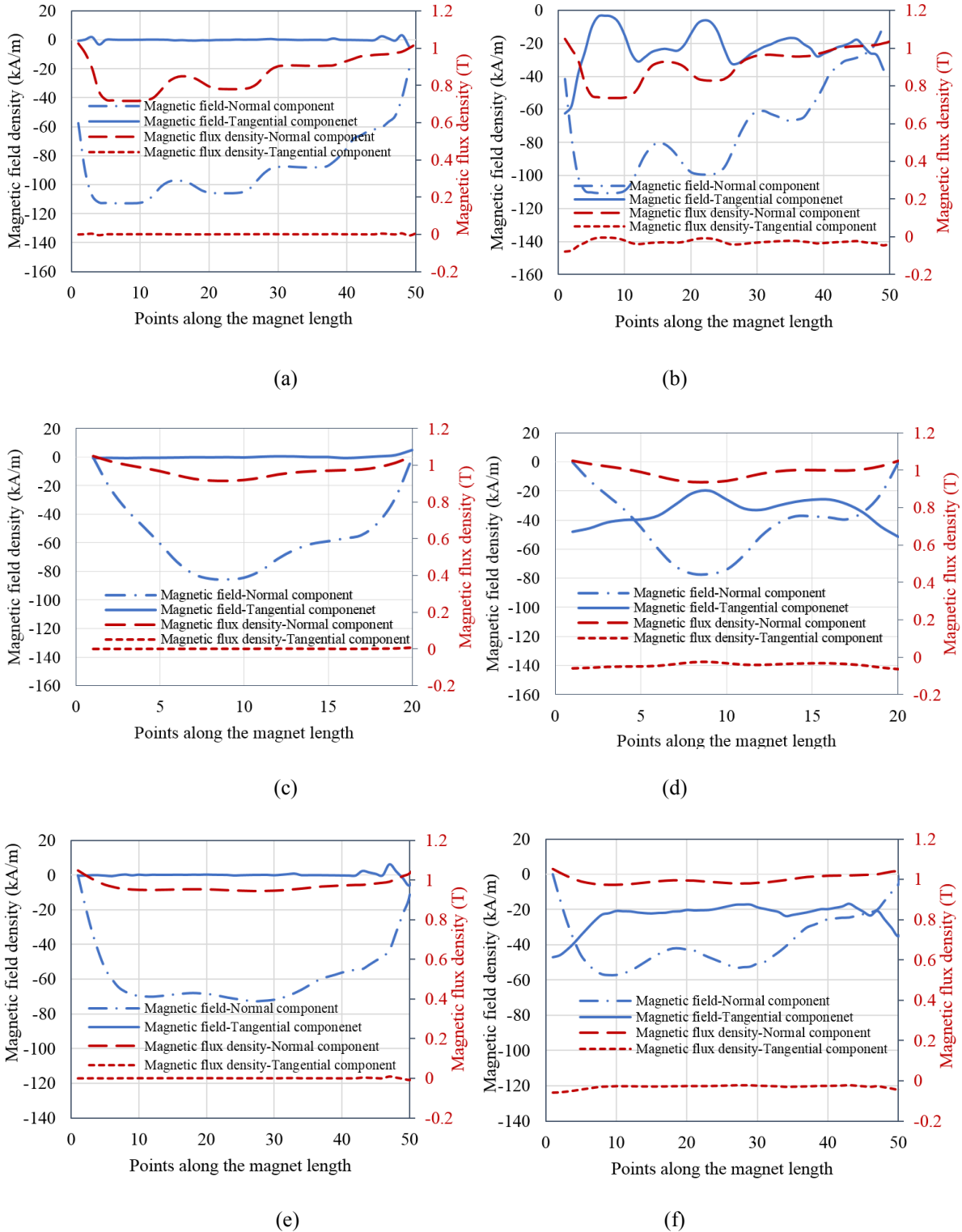
Fig. 3-17 Magnetic flux density and magnetic field intensity along the magnet length; (a) Design a no-load; (b) Design a full-load; (c) Design b no-load; (d) Design b full-load; (e) Design c no-load; (f) Design c full-load

The *q*-axis flux of the stator is parallel to the hypothetical line along the permanent magnet shown in Fig. 3-16 line while the *d*-axis component of the stator field is perpendicular to this line and in line with the magnetization direction of the permanent magnet. These curves for the three design variations of the PM assisted SynRM are presented in Fig. 3-17. The normal component of the magnetic field intensity does not vary from no-load to full-load condition, significantly. However the tangential component of the magnetic field intensity increases from no-load to full-load condition. The normal and the tangential components are defined with respective to the hypothetical dashed line as shown in Fig. 3-16. This component which represent the possibility of the irreversible demagnetization of the permanent magnet must remain well below the knee point of the BH curve of the AlNiCo 9 magnet.

To further study the effect of the magnet thickness on the operating point of the magnet, Design b is simulated with two magnet width values in full-load condition. The operating point of the magnet along the demonstrated line in Fig. 3-16 is calculated and compared with the BH curve of AlNiCo 9 magnet. Fig. 3-18 shows this comparison. In Fig. 3-18 (a) the operating point of the permanent magnet in Design b for different values of magnet thickness is shown. It is observed that the operating point of the magnet with smaller thickness (3 mm) moves beyond the knee point for some sections along the magnet length, while the magnet with 7 mm thickness remains in the linear region of the BH curve (The magnetic field intensity remains above -80 kA/m for the larger magnet). The same conclusion can be drawn for Design c with two different magnet thickness as shown in Fig. 3-18 (b).
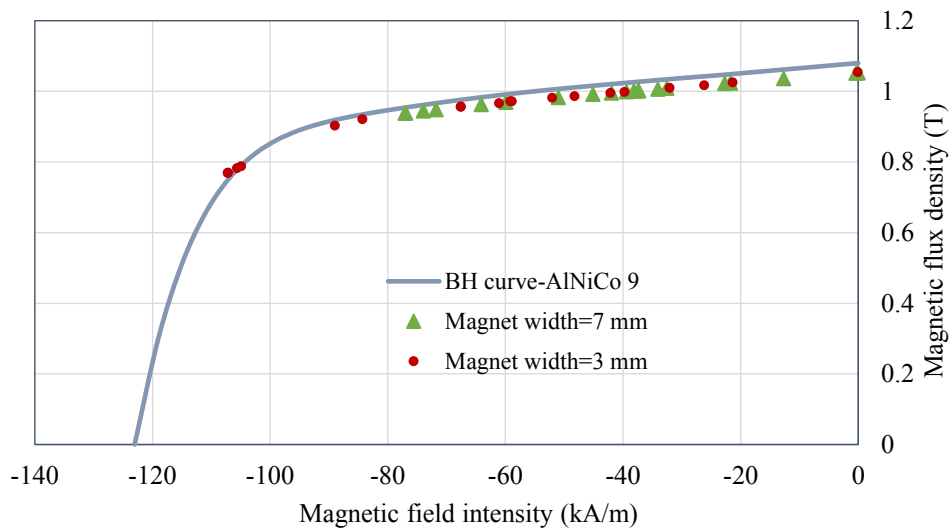
(a)
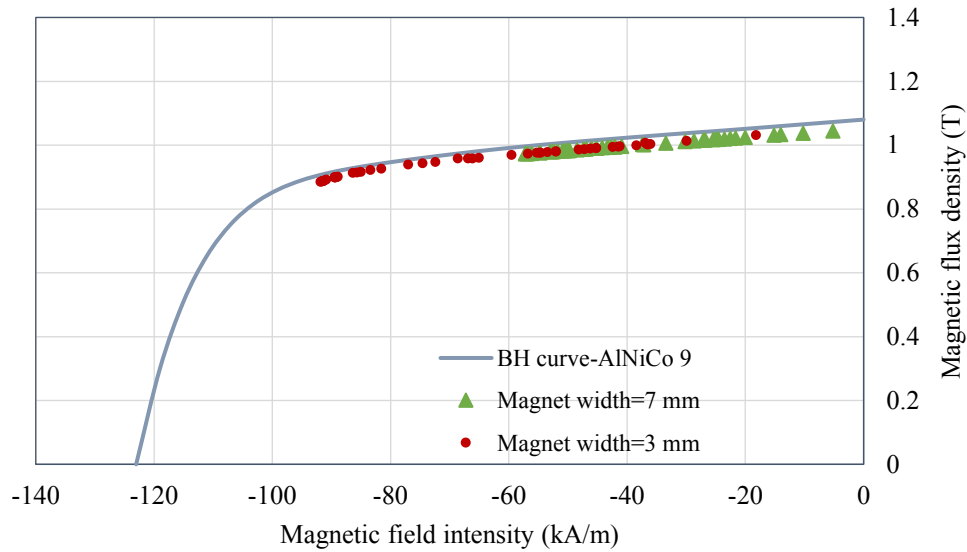
(b)

Fig. 3-18 The operating point of the permanent magnet in full-load condition; (a) Design b; (b) Design c

These curves reveal the impact of the permanent magnet thickness on the operating point of the permanent magnet and the risk of magnet demagnetization. However since the FEA software is not capable of multiple input BH curves for demagnetization purposes it is not possible to observe the effect of the magnet operating point on the possible demagnetization of the permanent magnet.

Based on the results obtained earlier regarding the operating point of the permanent magnet in the three design variations of the PM assisted SynRM, dynamic FEA simulation is performed for PM assisted SynRMs with 7 mm magnet thickness. Fig. 3-19 (a) compares the torque waveform of Design a, Design b, and Design c for rated condition. For comparison purposes the performance of these design variations are also tested with a rare-earth magnet type (N 48- B_r=1.37 T, H_c=1035 kA/m).

Fig. 3-19 (b) compares the torque waveform obtained from Design b with N 48, and AlNiCo 9, and the SynRM for rated current. Table. 3-3 summarizes the performance of Design a, Design b, and Design c using AlNiCo 9, and N 48, and the SynRM in terms of electromagnetic torque, torque ripple, power factor, and the utilized permanent magnet weight. The required weight of the permanent magnet is calculated based on the mass density of AlNiCo 9, and N 48 and using the utilized volume in the design ((mass density)$_{AlNiCo}$= 7000 kg/m^3, (mass density)$_{NdFeB}$=7500 kg/m^3).
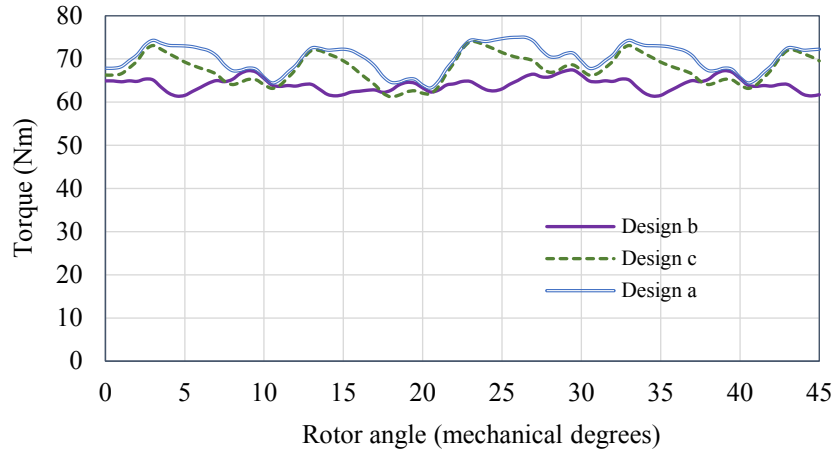
(a)
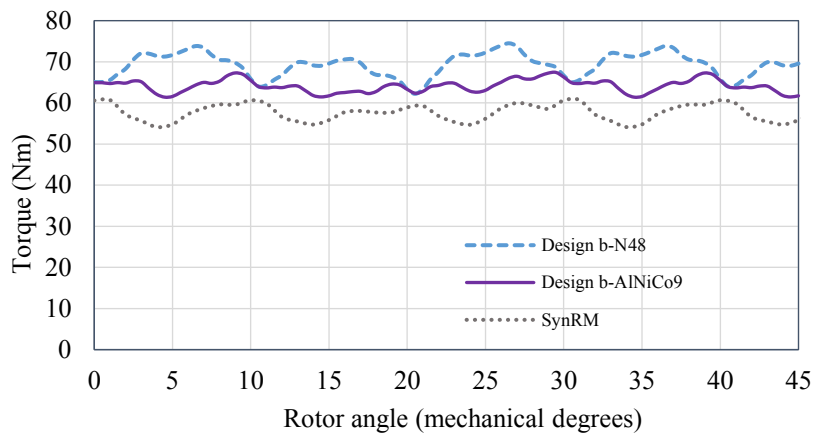
(b)

Fig. 3-19 (a) Torque waveform of three design variations using AlNiCo 9 (b) Torque waveform comparison of the SynRM, design b with AlNiCo 9, and design b with N 48

Table. 3-3 Design variation comparison of the PM assisted SynRM

	Peak torque (Nm)	Torque ripple (%)	Power factor	Required PM mass (kg) per pole
SynRM	57.77	11.3	0.65	0
Design a- AlNiCo 9	71.17	14.8	0.71	0.340
Design b- AlNiCo 9	64.42	9.3	0.70	0.192
Design c- AlNiCo 9	68.75	15.7	0.71	0.220
Design a- N48	84.03	29.3	0.75	0.364
Design b- N48	70.01	14.9	0.72	0.206
Design c- N48	72.91	21.3	0.75	0.236

3.3.3. Torque-Speed Envelopes, Efficiency Map, and Saliency Ratio Comparison

The torque-speed curves are essential for a proper comparison of electrical machines under similar supply conditions. The torque-speed curves are usually characterized by rated torque, rated power, and base speed of the machine, and they depict the torque production capability of the machine, and the maximum speed (base speed) that can be achieved before the point where the output torque needs to be reduced (field weakening operation) in order to maintain a constant output power. Under similar supply conditions (DC bus voltage) the PM assisted SynRM is expected to have a lower base speed when compared to a similar size SynRM. However the torque production capability of a PM assisted SynRM is expected to be higher in constant torque region (before the base speed).

The torque-speed curves of Design b is compared with the torque-speed of the SynRM under similar supply condition with two DC bus voltage magnitudes and 20 A line rms current. These curves which are obtained from MotorSolve® are shown in Fig. 3-20. In Fig. 3-20 (a) with a higher DC bus voltage, the base speed of both PM assisted SynRM, and SynRM are higher than Fig. 3-20 (b) with a lower DC bus voltage. As expected the base speed of the SynRM is higher than the base speed of the PM assisted SynRM. However the PM assisted SynRM has a higher torque per ampere value before the base speed.

(a)   (b)
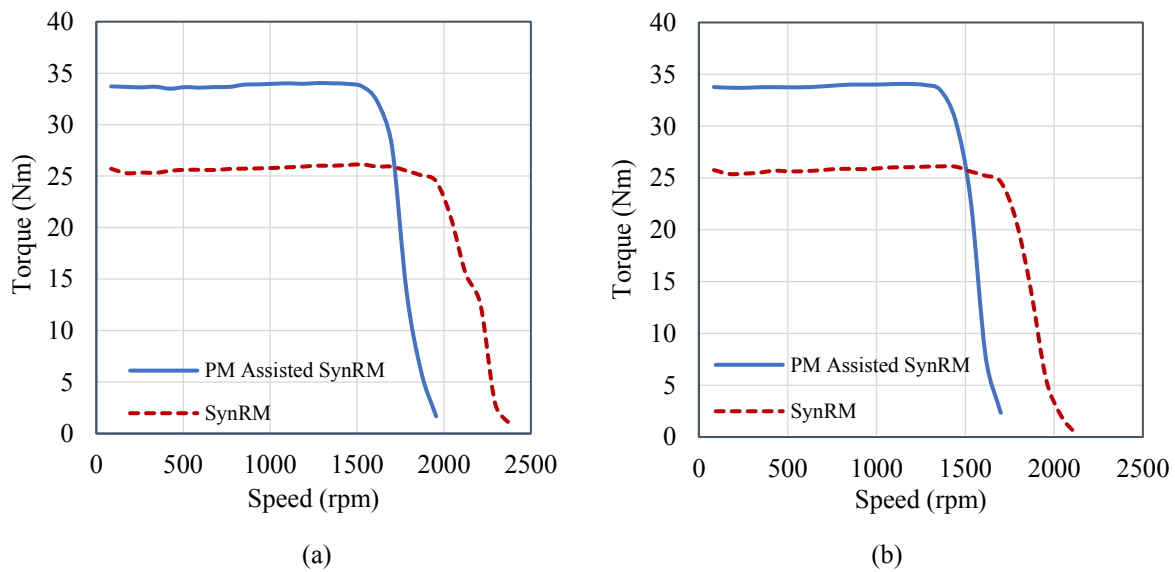
Fig. 3-20 Torque-speed curves of the PM assisted SynRM and SynRM; (a) 400 V DC bus voltage; (b) 350 V DC bus voltage

The efficiency map of the PM assisted SynRM (Design b) and the SynRM are compared in Fig. 3-21. The two efficiency maps obtained from MotorSolve® compare the torque production capability and the efficiency of the PM assisted SynRM and SynRM with the same supply condition (400 V DC bus voltage, and 20 A line rms current).
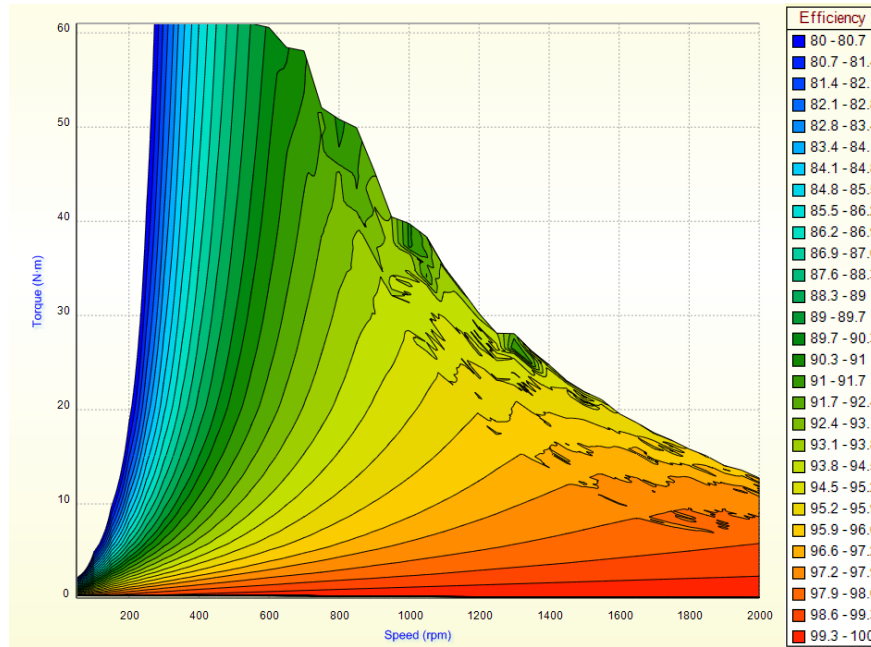
(a)
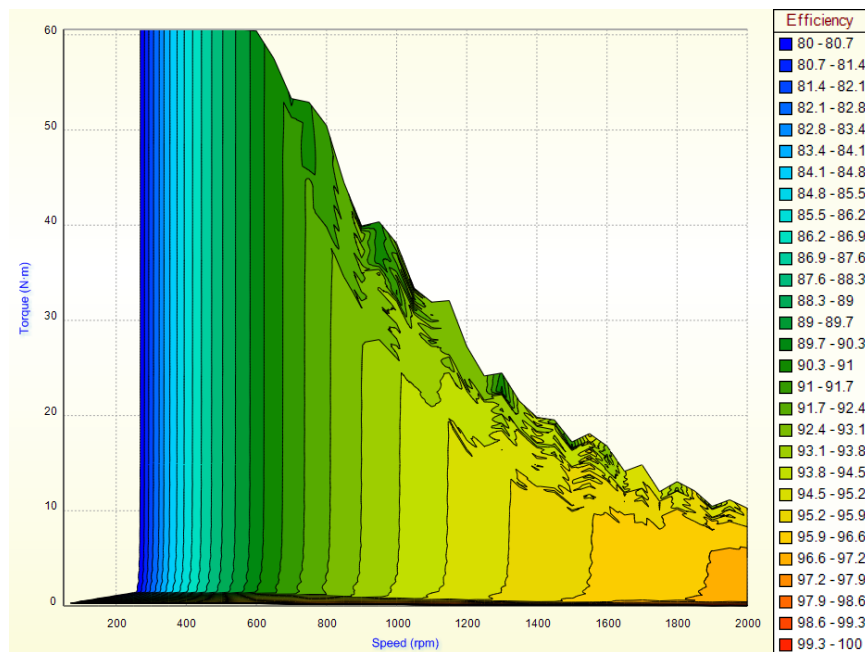
(b)

Fig. 3-21 Efficiency map; (a) The PM assisted SynRM (Design b); (b) SynRM

It is observed that the efficiency of the PM assisted SynRM is higher than the efficiency of the SynRM for most parts of the map. For example, at 1000 rpm, and 35.1 Nm, the efficiency of the PM assisted SynRM is 93.7%, while at the same operating point the efficiency of the SynRM is 91.4%. The PM assisted SynRM also shows a higher efficiency value when compared to the SynRM beyond the base speed. However the base speed of the PM assisted SynRM is less than the base speed of the SynRM (as it was also shown in Fig. 3-20). Therefore the constant power region (field weakening operation) with the same DC bus voltage, starts at a lower speed for the PM assisted SynRM.

Another important characteristic of SynRMs and PM assisted SynRMs is d-axis and q-axis inductance values at different current magnitudes, and thereby the saliency ratio of the machines. These parameters are compared in Fig. 3-22. Due to the location of the permanent magnet in the rotor (on the d-axis flux path of the machine), the d-axis inductance of the PM assisted SynRM is less than the d-axis inductance of the SynRM. However the q-axis inductance of the PM assisted SynRM is less than the q-axis inductance of the SynRM below 8 A. This results in an improved saliency ratio of the PM assisted SynRM for current values below 7 A, as can be seen in Fig. 3-22 (b). On the other hand when the current value is above 8 A the saliency ratio of the PM assisted SynRM is less than the saliency ratio of the SynRM.

(a)   (b)
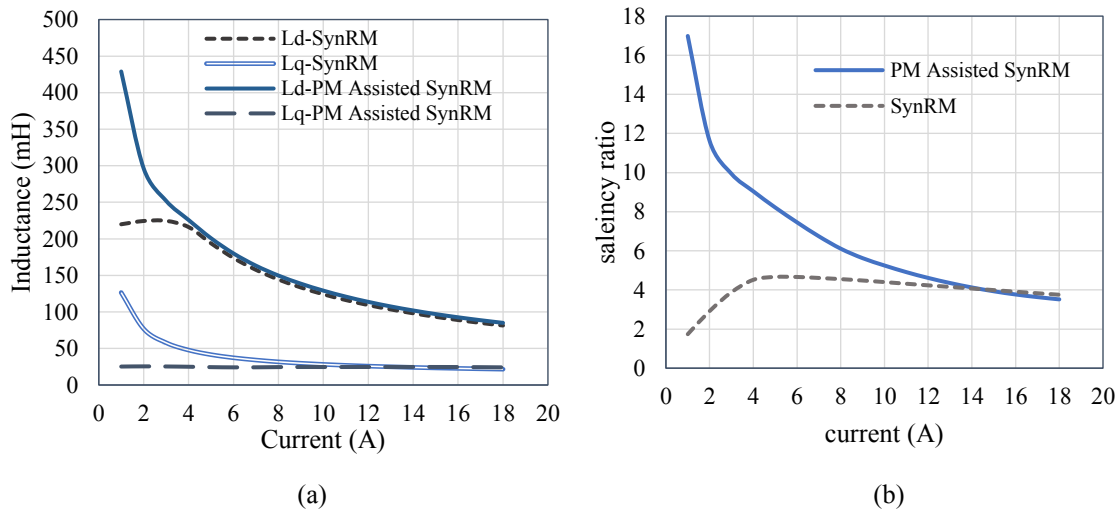
Fig. 3-22 (a) d-axis and q-axis inductances of the PM assisted SynRM and SynRM; (b) Saliency ratio of the PM assisted SynRM and SynRM

Fig. 3-22 shows one of the main challenges of the design of a PM assisted SynRM, or in general any PM machine with buried magnets in the rotor core. If the permanent magnets are placed on the same path as the d-axis flux path, the reduction in the d-axis inductance is an

inevitable consequence, due to the low relative permeability of the permanent magnet. However in the proposed design topology in this chapter, the existing flux barriers limit the q-axis flux, thus resulting in a low q-axis inductance. Therefore the PM assisted SynRM loses its saliency only partially. In other design variations of the permanent magnet assisted SynRM such as the ones shown in Fig. 3-3, the added permanent magnets alter the d-axis and q-axis placement of the machine. Such topologies usually provide a smaller saliency ratio values when compared to the proposed topology in this chapter.

3.4. Final Design of the Permanent Magnet Assisted Synchronous Reluctance Machine

Based on the FEA results presented in section 3.3 and the analytical modeling procedure presented in section 3.2 the PM assisted SynRM topology is finalized for prototyping. The choice of the permanent magnet type is done based on the availability and the price of AlNiCo magnets when compared to various types of rare-earth magnets. Due to the nonlinear characteristics of the BH curve of AlNiCo magnets as shown in Fig. 3-6, the choice of the machine's topology and magnet placement must be done carefully. It is of great importance to choose the magnet location in a manner to minimize the risk of unwanted demagnetization from the stator field. Therefore apart from magnet placement, its sizing (especially magnet thickness) must be done carefully. Another important feature is maintaining the saliency ratio of the machine. In that regard the magnet thickness plays an important role. A thick permanent magnet reduces the d-axis inductance of the PM assisted SynRM topology shown in Fig. 3-4, while a thin magnet may easily demagnetize under strong stator fields, as shown in Fig. 3-18 for two different magnet thicknesses used for two of the design variations.

Once the proper width of the magnet is chosen the other geometrical features such as length and placement must be decided. Based on Fig. 3-19 and Table. 3-3 Design a provides the highest torque enhancement when compared to Design b, and Design c. It also results in a higher power factor. Amongst the three design variations, Design b shows the lowest torque ripple value as it is also observed from Fig. 3-19. Design b also demands a smaller quantity of permanent magnet material when compared to Design a, and Design c. Moreover the placement of the smallest flux barrier on the top of the permanent magnet in Design b, limits the amount of q-axis flux (perpendicular to the magnetization direction of the permanent

magnet) passing through the magnet, while in Design a and Design b this feature does not exist. This feature protects the permanent magnet from the *q*-axis flux of the stator, thus reducing the risk of magnet demagnetization. Comparing the torque-angle curves of the three design variations also reveals that, Design b provides a smooth torque characteristic along the positive portion of the operating rotor angle when compared to the other two design variations. This feature makes the control procedure simpler. Based on the abovementioned points, Design b is chosen for the final prototyping procedure.

3.5. The Prototyped PM Assisted SynRM

Based on the selected design topology presented in the previous section (Design b), the rotor of the PM assisted SynRM is prototyped according to the stator dimensions of the existing SynRM. In this section the test results performed on the prototyped PM assisted SynRM are presented and compared with the test results of the SynRM under similar operating conditions.

The experiments include static torque measurement (as demonstrated in Chapter 2 for the SynRM), *d*-axis and *q*-axis inductance measurement, and dynamic test under load.

3.5.1. Static Torque Measurement

The rotor lamination of the PM assisted SynRM is shown in Fig. 3-23 (a). Fig. 3-23 (b) shows the final rotor assembly. The rotor laminations are cut with a larger radius than the designed rotor. This additional radius is removed after all the laminations are stacked to obtain the desired outer radius of the rotor that can fit in the existing stator prototype.

| (a) | (b) |
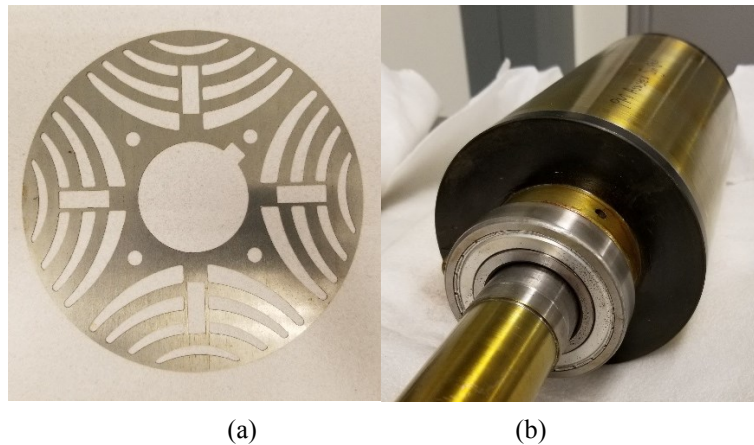
Fig. 3-23 (a) rotor lamination of the PM assisted SynRM; (b) Final rotor assembly of the PM assisted SynRM

The final prototype is placed inside the stator and held in place using the ball-bearings on the two ends of the rotor shaft (as shown in Fig. 3-23 (b)).

The static test procedure is explained in Chapter 2 for the SynRM. The rotor position is determined using the encoder, while the torque exerted on the shaft is measured using the torque transducer. The static torque produced by the PM assisted SynRM is measured for three current magnitudes: 8 A, 12 A, and 16 A. For each current magnitude the rotor angle is varied from 0 degrees to 100 degrees electrical. Fig. 3-24 compares the torque–angle curves of the SynRM and the PM assisted SynRM for these three current magnitudes when the permanent magnets are 50 percent magnetized.

(a)

(b)

(c)
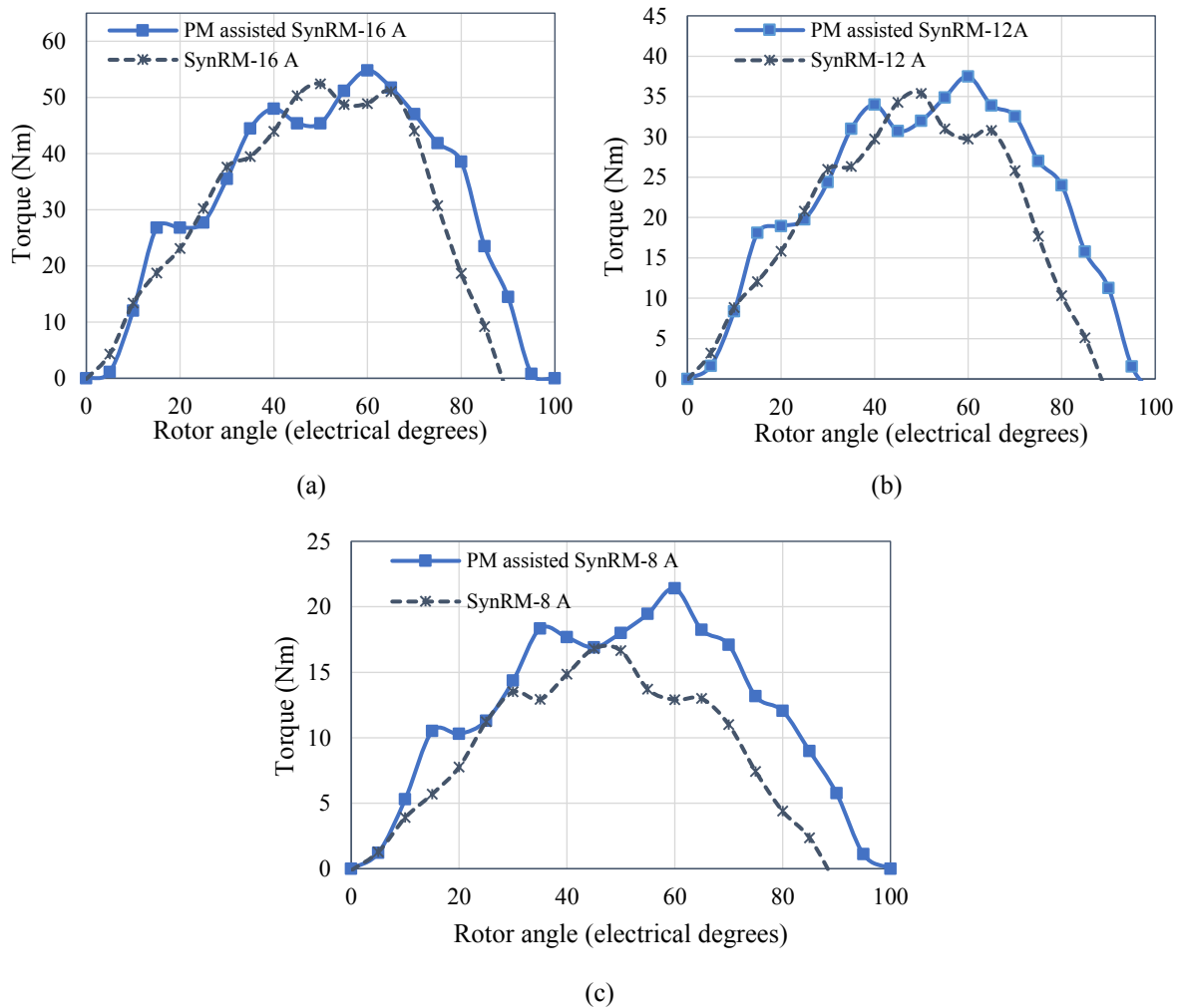
Fig. 3-24 Torque-angle curves of the SynRM and the PM assisted SynRM; (a) 16 A; (b) 12 A; (c) 8 A

The peak torque of the PM assisted SynRM for 16 A is 55 Nm while the peak torque of the SynRM is 52 Nm. The largest improvement in the output torque of the PM assisted SynRM when compared to the SynRM takes place at the lower current magnitude (8 A). When the

machine is supplied with 8 A the peak torque of the PM assisted SynRM is 22 Nm which is 29 percent higher than the torque produced by the SynRM at the same phase current (17 Nm). The effect of permanent magnets is also observed in Fig. 3-24. The torque-angle curve of the SynRM reaches its zero value at 90 degrees electrical. However the PM assisted SynRM provides 14.5 Nm torque at 90 degrees which originates from the permanent magnets.

3.5.2. *d*-axis and *q*-axis Inductance Measurement

The *d*-axis and *q*-axis inductances of the PM assisted SynRM and the SynRM are measured using the DC test. In this test a DC current with the desired magnitude is supplied through the phase winding of the machine while the rotor is locked at *d*-axis or *q*-axis (for *d*-axis or *q*-axis inductance measurement). The voltage and current curves of the winding are captured as the supply voltage is switched to zero. The voltage and current curves of the PM assisted SynRM are shown in Fig. 3-25. In this figure the supply current is set to 16 A and then switched off.
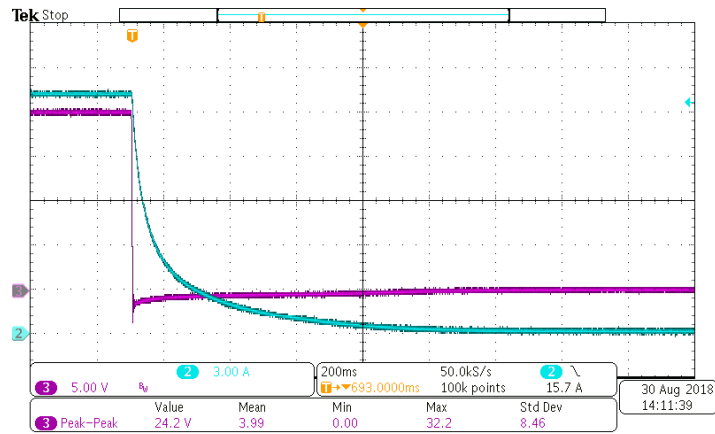
Fig. 3-25 Phase voltage and current curves of the PM assisted SynRM for inductance measurement

Using equation (3.7) the flux linkage, λ is calculated based on the voltage and current curves.

$$\lambda = -\int_0^t (v - Ri)d\zeta \tag{3.7}$$

where v, R, i, and ζ is the voltage, resistance, current, and the dummy variable of integration. t shows the time period of integration. Using the demonstrated approach, the *d*-axis and *q*-axis inductances of the PM assisted SynRM and the SynRM are obtained. Fig. 3-26 compares the *d*-axis and *q*-axis inductances of the two machines.
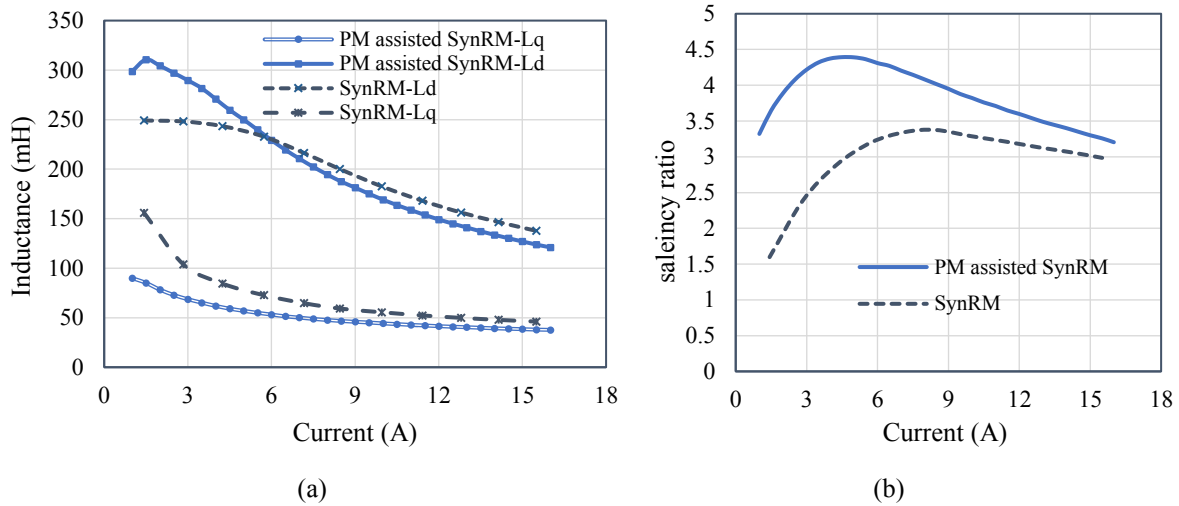
Fig. 3-26 (a) *d*-axis and *q*-axis inductrance of the SynRM and the PM assisted SynRM; (b) Saliency ratio of the SynRM and the PM assisted SynRM

The presence of the permanent magnets in the PM assisted SynRM has reduced the *q*-axis inductance of the machine in comparison with the SynRM which in turn results in a higher saliency ratio as shown in Fig. 3-26. The *d*-axis inductance of the PM assisted SynRM is higher than the *d*-axis inductance of the SynRM for current magnitudes below 6 A. However at higher current magnitudes the *d*-axis inductance of the PM assisted SynRM drops faster than that of the SynRM due to the saturation of the rotor core.

3.5.3. Dynamic Torque and Power Factor Measurements

To further investigate the effect of the permanent magnets on the performance of the PM assisted SynRM the machine is tested under loaded condition. The SynRM and the PM assisted SynRM are tested in the same loading condition of 5 A current vector magnitude and for three different current vector angles: 31, 51, and 71 degrees. Table. 3-4 summarizes the torque mean value, and the power factor obtained from the two machines.

Table. 3-4 Performance comparison of the SynRM and the PM assisted SynRM in loaded condition

	Current magnitude (A)	Current angle (degrees)	Torque (Nm)	Power factor
SynRM	5.65	31	6	0.35
	4.95	51	6	0.53
	5.93	71	6	0.61
PM assisted SynRM	5.65	31	11.2	0.55
	4.95	51	8.1	0.62
	5.93	71	8.0	0.63

94

It is observed that the presence of the permanent magnets has resulted in a higher torque production (from 6 Nm to 11.2 Nm for 31 degrees current angle) and a power factor improvement.

The back-EMF voltage of the PM assisted SynRM is also measured by running the DC machine coupled to the shaft of the PM assisted SynRM on the dynamometer bench. The phase voltage of the PM assisted SynRM for 50 percent magnetization of the permanent magnets is shown in Fig. 3-27.
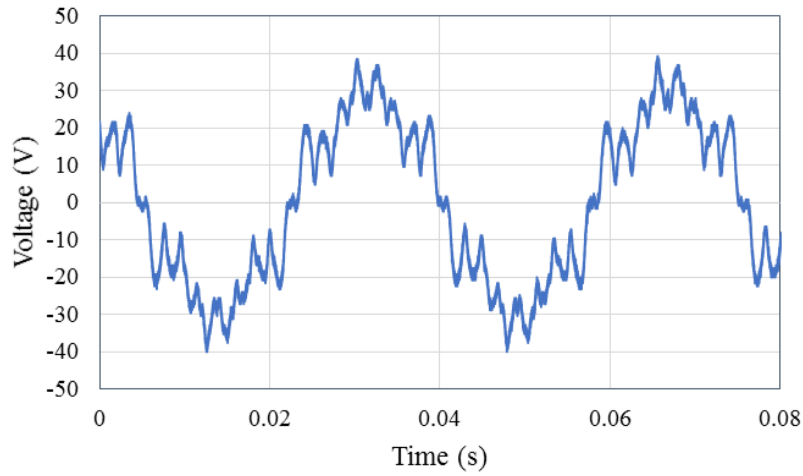
Fig. 3-27 The back-EMF voltage of the PM assisted SynRM at 850 rpm

3.6. Summary of the Chapter

In this chapter initially the permanent magnet assisted SynRM and its possible design variations were presented. Different permanent magnet materials were briefly discussed and their features were shown. Based on the available permanent magnet type a topology for PM assisted SynRM was proposed with the idea of maintaining a high reluctance torque to magnet torque ratio. Based on this desired characteristic three design variations of the PM assisted SynRM were initially examined based on the developed analytical modeling method. Further analysis was carried out using two FEA packages. The FEA simulation results depicted the requirements to achieve a proper performance while minimizing the risk of an unwanted demagnetization of the permanent magnet. Based on the obtained results the final topology and dimensions of the PM assisted SynRM was eventually selected.

A PM assisted rotor was prototyped based on the selected design and tested under various loading conditions.

Chapter 4 Stand-Alone Operation of the Synchronous Reluctance Generator

4.1. Introduction

SynRM as a robust [33], simple, and comparatively less expensive generator initially gained interests in 1990s. Through the past three decades, different aspects of the generator operation of the SynRM have been discussed in various research works. As an example the performance and output characteristics of synchronous reluctance generators (SynRGs) are discussed in [34, 35, 36]; the operating limits of the SynRG are presented in [37, 38]; and control strategies of the SynRG are explained in [39, 40, 41, 42]. [84] studies the transient, dynamic, and steady state performance of self-excited reluctance generator through computer simulations, and the effect of load resistance on the voltage collapse are shown. Due to the absence of field excitation (such as permanent magnets or field winding similar to a wound field synchronous machine) in SynRMs, the generator operation is more challenging when compared to a typical permanent magnet synchronous machine (PMSM). Therefore in some studies the absence of field excitation on the rotor is compensated by adding a DC winding to the stator [85]. This DC winding enables the machine to operate either in the synchronous, sub synchronous or super synchronous modes, at a relatively high manufacturing and operation cost. A stand-alone SynRG is not capable of producing the required electromotive force to supply the load, unless it is connected to a properly sized capacitor bank. Although the capacitor bank is necessary for stand-alone generator operation of the SynRG, it is not adequate. The generator operation of SynRM requires maintaining certain criteria [86], somehow the same as induction generators [43, 44]. Despite the importance of the start-up procedure in SynRG only a few number of studies have focused on the requirements which assure the build-up procedure of the terminal voltage of the SynRG.

The build-up procedure of the terminal voltage in stand-alone SynRGs and induction machines is usually referred to as self-excitation and it depends on the nonlinear characteristic of the ferromagnetic core material [39], presence of a sufficient initial condition in the system [43], a properly sized capacitor bank, and maintaining a minimum speed. The required initial condition can either be an initial voltage on the capacitor bank or a residual magnetism in the

machine's core. The studies of self-excitation phenomenon in induction generators can be found in [44, 45, 46]. However fewer studies of this phenomenon in SynRMs are performed. Most of the available research focus on the output characteristics of the SynRG as mentioned earlier. In [47] the steady-state performance of the SynRG is studied and it is shown that the air gap flux linkage and core saturation affect the generator performance significantly. Control strategies of the SynRG such as extended speed range operation while decreasing the conduction loss are discussed in [34]. Voltage control for a super high-speed SynRG system with a pulse width modulation (PWM) voltage source converter is presented in [42]. Testing the SynRG at different loading conditions, obtaining the efficiency and power factor of the machine, and identifying the maximum power-conversion capability of the SynRG are covered in [48]. However none of the mentioned studies, investigate the criteria for self-excitation of the SynRG in stand-alone operation. Although it is observed in experiments that the occurrence of self-excitation requires certain criteria to be met [86, 87].

To ensure the occurrence of self-excitation, pre-charging of the capacitors is suggested generally as a method for providing the required initial condition [43, 88] and the core characteristic analysis is usually neglected in the available literature. The main reason for this choice (pre-charging the capacitors) is that the presence of the residual flux is considered to be unreliable and difficult to investigate. However it is shown in this chapter that the residual flux as an initial condition can be reliable, if certain criteria are met. Besides once the magnetic core is magnetized, the obtained residual flux will remain, unless the core is demagnetized by some external source (due to a fault for instance).

The required criteria to ensure a successful self-excitation in a stand-alone SynRG are investigated in this chapter. It is shown in section 5.2 that despite the mathematical prediction, only the presence of the initial condition in the system does not always result in the successful voltage build-up process. In other words the initial condition of the system must be above a certain value which is shown in this chapter. This initial value must be provided prior to the start-up of the SynRG and can be either a voltage in the capacitor bank or a residual magnetism in the core. This study considers the minimum required residual magnetism. To obtain the minimum residual flux, the machine's characteristics, ferromagnetic core material of the machine, and the size of the capacitor bank must be identified. It is also observed in simulations that the start-up acceleration of the SynRG to achieve the nominal speed required for self-

excitation may create transients in the *q*-axis flux linkage that can demagnetize the machine's core and lead to voltage collapse. This effect is also investigated through several experiments. In this chapter the self-excitation criteria of the SynRG in stand-alone operation is discussed based on simulation and experimental results on a 5 hp SynRM.

4.2. Stand-Alone Operation of the Synchronous Reluctance Generator

In order to study the self-excitation procedure in stand-alone SynRGs the machine's parameters must be initially identified. In this section the SynRM used in the simulations and experiments is introduced. Based on the machine's parameters the *dq* model of the stand-alone SynRG connected to a capacitor bank is developed in MATLAB Simulink, and used for analysis.

4.2.1 The Synchronous Reluctance Machine

In this study the analysis of the SynRG-capacitor system is performed using the *dq* model. The *dq* model is also widely used to simulate SynRM in the literature [34, 37, 48, 47]. The results of the *dq* model is then used in the Energetic Model to analyze the machine's core behavior and calculate the residual flux in the core as a result of the core magnetization at a certain amount of current. Thus a deeper understanding of the machine's behavior is achieved prior to generator operation, and during terminal voltage build-up. This study commences with measuring the machine's parameters; that is, L_d, L_q and the phase winding resistance. Fig. 4-1 (a) shows the rotor of the machine. Fig. 4-1 (b) shows the *d*-axis and the *q*-axis inductances of the machine as a function of the current. The same data is also used for simulation. The two curves shown in Fig. 4-1(b) are obtained through experiments by locking the machine at the *d*-axis (or *q*-axis for the *q*-axis inductance measurement) using a mechanical lock. The phases are arranged in star connection, and two of the phase are shorted. By applying an AC voltage across the phases the desired current magnitude in the phase is achieved. A power meter is used to measure the reactive power of the machine. Thus the reactance and in turn the inductance can be calculated. Since the rotor is locked at the *d*-axis, the current that flows in the winding is the *d*-axis current. By doing the same procedure while locking the rotor at the *q*-axis, the inductance of *q*-axis is obtained for various current values. In this case the current represents the *q*-axis current. Therefore the term "current" which is used in the Fig. 4-1(b) represents the *d*-axis or *q*-axis current depending on the curve. Fig. 4-1 (c) shows the *dq* equivalent circuit of the

machine representing the operation of a SynRM connected to a capacitor bank in no-load condition. The d-axis current which is the magnetizing current in no-load condition is provided by the capacitors to keep the machine's core magnetized. If the machine is in a loaded condition, the q-axis current will be supplied to the load. Table. 4-1 summarizes some information of the machine.

(a)

(b)

d-axis circuit

q-axis circuit

(c)
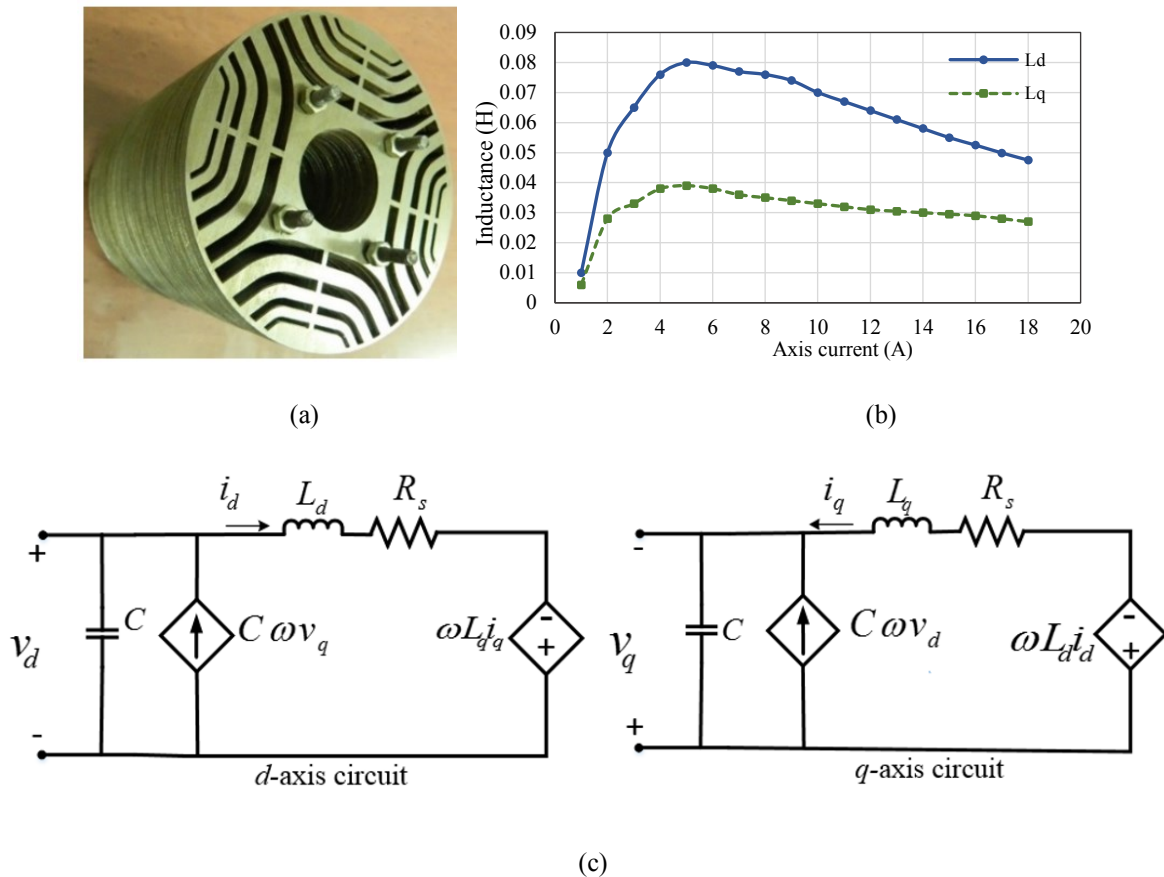
Fig. 4-1(a) Rotor of the SynRM used in the experiments; (b) d-axis and q-axis inductances of the SynRM; (c) d and q-axis equivalent circuits

Table. 4-1 The parameters of the 5 hp SynRM

Parameter	Value
Rated voltage	220 V-delta
Rated current	16.5 A
Rated power	5 hp
Number of poles	4
Number of stator slots	36
Magnetic steel material	M45 G29

99

Equations (4.1) to (4.4) represent the *dq* model of a SynRG connected in parallel to a capacitor bank, neglecting the core loss resistance.

$$\frac{d\lambda_q}{dt} = v_q - R_s i_q - \omega\lambda_d \tag{4.1}$$

$$\frac{d\lambda_d}{dt} = v_d - R_s i_d + \omega\lambda_q \tag{4.2}$$

$$\frac{dv_d}{dt} = -\frac{i_d}{C} + \omega v_q \tag{4.3}$$

$$\frac{dv_q}{dt} = -\frac{i_q}{C} - \omega v_d \tag{4.4}$$

where, i_q, i_d, v_q, v_d, R_s, ω λ_d, λ_q, and C are the *q*-axis current, *d*-axis current, *q*-axis voltage, *d*-axis voltage, phase resistance, speed of the frame, *d*-axis flux linkage, *q*-axis flux linkage, and capacitance, respectively. These equations are used for analysis of the machine's operating point and the criteria for a successful self-excitation.

To perform the *dq* simulation of the machine, equations (4.1) to (4.4) are implemented in MATLAB Simulink. The flux linkage-current curves (*d*-axis and *q*-axis) are used as lookup tables in the Simulink. These curves are obtained from the *d*-axis and *q*-axis inductance curves shown in Fig. 4 (b).

4.3. Self-Excitation Criteria of the Stand-Alone Synchronous Reluctance Generator

To analyze the stand-alone operation of the SynRG the *dq* equations of the machine connected in parallel to a capacitor bank is used. Fig. 4-2 shows the schematic of the system.
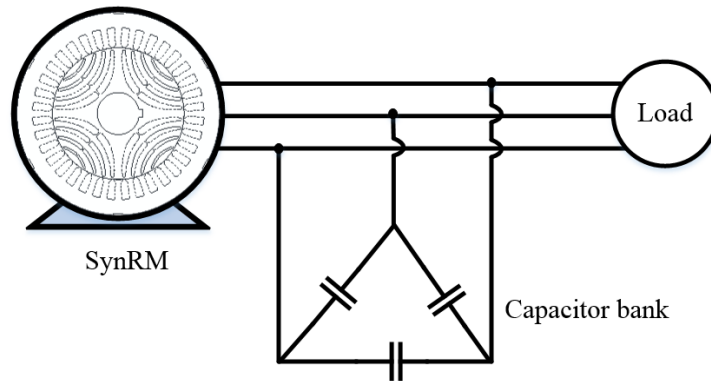
Fig. 4-2 The schematic structure of the stand-alone SynRG

The capacitors provide the required magnetizing current of the SynRM while supplying the possible requirement of the load reactive power. The SynRM provides the active power of the load. Therefore the minimum size of the capacitor bank is decided based on the machine's characteristics which is discussed in this section. If the load demands reactive power, the load requirement must also be considered in capacitor sizing. However this study mainly focuses on the criteria for self-excitation and the start-up procedure of the SynRG, and operation of the SynRG under load is not considered.

4.3.1. The Minimum Residual Flux Requirement

Equations (4.1) to (4.4) predict the occurrence of a successful self-excitation irrespective of the amount of the initial condition (capacitor initial voltage or residual magnetism in the core) in the system. This observation is also made in the simulations using MATLAB Simulink. Therefore in the look-up tables used in the Simulink file for *d*-axis and *q*-axis flux linkages of the machine, any non-zero *d*-axis flux linkage for zero current in the *d*-axis can result in a successful voltage build-up of the SynRG model. However it is observed through experiments that although the presence of the initial condition in the system is necessary, not any amount of initial condition can be satisfactory for a successful voltage build-up. This observation is also reported in the research works performed on stand-alone induction generators [44]. However the minimum required residual flux in stand-alone SynRGs had not been studied to the date of the research presented here. This section presents the minimum required residual flux to initiate the triggered self-excitation [44] in SynRGs operating in stand-alone condition by analyzing the machine's system of equation.

The minimum required residual flux is obtained by arranging the system equations ((4.1) to (4.4)) in the form of implicit nonlinear equation as:

$$A\dot{X} = BX \tag{4.5}$$

Where

$$A = \begin{bmatrix} L_q & 0 & 0 & 0 \\ 0 & L_d & 0 & 0 \\ 0 & 0 & C & 0 \\ 0 & 0 & 0 & C \end{bmatrix} \tag{4.6}$$

$$B = \begin{bmatrix} -R_s & -\omega L_d & 0 & 0 \\ \omega L_q & -R_s & 0 & 0 \\ -1 & 0 & 0 & -C\omega \\ 0 & -1 & C\omega & 0 \end{bmatrix} \tag{4.7}$$

$$X = \begin{bmatrix} i_q & i_d & v_q & v_d \end{bmatrix} \tag{4.8}$$

where, L_d and L_q are the d-axis and q-axis inductances of the machine, obtained from the experiment (Fig. 4-1 (b)), and are functions of the respective current.

The operating modes of the SynRG are identified by finding a frequency ω^* for which, a constant solution in a rotating reference frame exists. In such a situation, d-axis and q-axis voltages and currents are constant and one can write (4.5) as:

$$BX = 0 \tag{4.9}$$

For (4.9) to have a non-zero solution, the determinant of the matrix B must be equal to zero.

$$C^2 L_q L_d \omega^{*4} + (C^2 R_s^2 - C L_d - C L_q)\omega^{*2} + 1 = 0 \tag{4.10}$$

Using the inductance values for the d-axis from Fig. 4-1 (b), and considering 100 μF capacitors, the possible range of operating speed is obtained for this system by solving the 4th order polynomial of (4.10). Fig. 4-3 (a) shows the obtained sets of solutions of (4.10) considering the current dependent d-axis inductance of the machine and the no-load q-axis inductance of the machine (39 mH).

Equation (4.10) is solved for a constant q-axis inductance, and by varying the d-axis inductance of the machine as a function of the current.

The curves shown in Fig. 4-3 (a) demonstrate the operating speeds of the SynRG at various magnetizing (d-axis) current magnitudes. Since these curves are obtained for no-load operation of the SynRG, the current axis represents the d-axis current of the machine (magnetizing current). Polynomial (4.10) has at most four solutions for any value of the d-axis current, depending on the coefficients (L_d and L_q) which are current dependant. Due to the system parameters in this case, (4.10) has four sets of solutions, of which two sets fall in the negative side of the speed axis (vertical axis) and do not have a practical importance. These two sets of solutions are labeled as curves 3, and 4 in Fig. 4-3 (a). The other two sets located in the first quadrant of the speed-current graph, are the mirrored image of curves 3, and 4. The upper curve,

labeled as curve 1 in Fig. 4-3 (a) does not demonstrate a practical solution either, since the bottom curve (curve 2) presents a lower speed with the same value of the *d*-axid current. Therefore the SynRG will self-excite upon the moment of reaching the corresponding point of the lower speed on curves 2. Curve 2 shown in Fig. 4-3 (a) is the practical solution of the polynomial (4.10) identifying the corresponding current at each rotor speed. The current axis in Fig. 4-3 represents the no-load current of the SynRG with the main component being the *d*-axis current. The *d*-axis current in no-load condition shows the required magnetizing current of the SynRG to maintain the core magnetization. This curve also demonstrates the criteria for self-excitation of the SynRG.
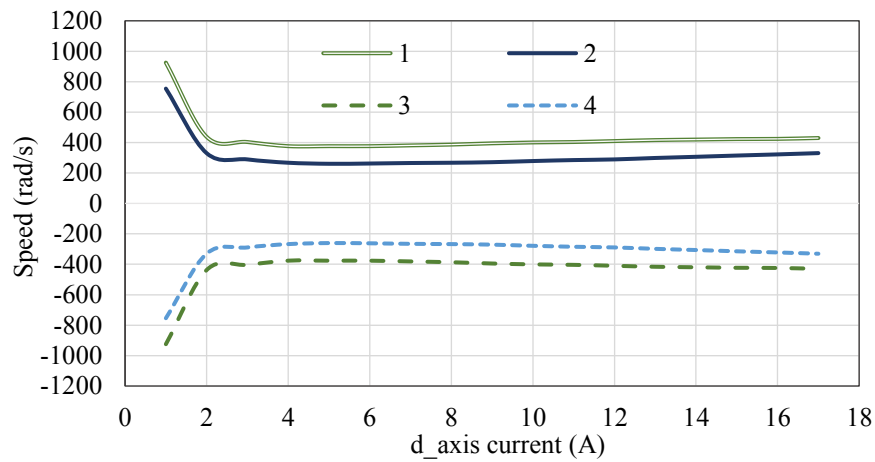
(a)
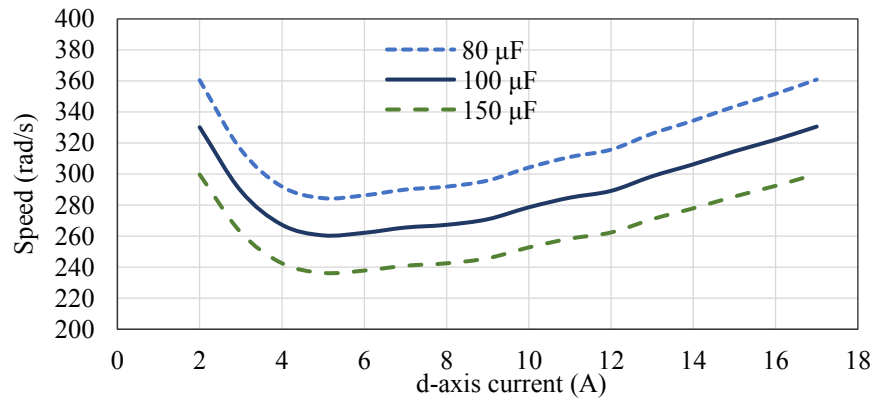
(b)

Fig. 4-3 (a) Possible operating speeds and solutions of the polynomial (10); (b) The operating points for three different values of the capacitor bank (curve 2 from (a))

It can be seen in Fig. 4-3 (a) that at 5 A, the self-excitation takes place at around 260 rad/s. This is the minimum speed which ensures the generator operation of this system. The minimum

speed and the shape of the solution curves are defined by the system parameters such as the machine's characteristics and the size of the capacitor bank. Increasing the speed after this point (5 A), will result in a linear increase in the d-axis current. Curve 2 also shows that for d- axis currents below 5 A, the required speed to achieve self-excitation is much higher than the speed for above 5 A, and it also grows rapidly, making the operation for such d-axis currents impractical. Therefore the required magnetizing current and the imposed speed to the shaft by the prime mover defines the operational limit of the generator in no-load condition.

This curve can also be used to estimate the minimum required residual flux to ensure the self-excitation. Pre-magnetizing the core by 5 A or higher, results in a remaining magnetism value in the material which will be sufficient to trigger the self-excitation as the rotor speed reaches 260 rad/s. In other words, the initial magnetism generated by magnetizing the core with 5 A or more, produces enough magnetizing current when the rotor speed reaches 260 rad/s, thus triggering the self-excitation. If less than 5 A is used for magnetizing the machine's core, the theoretical speed to achieve self-excitation increases infinitely as the utilized magnetizing current reduces, making the practical procedure impossible. Therefore the minimum required magnetizing current to ensure the occurrence of the self-excitation, obtained from the analytical model of the SynRG used in this study is 5 A. The shape of the curve is only dependent on the machine's inductance characteristic. Thus the value of the capacitor bank connected to the phase windings only affects the value of the speed, and shifts the curves up or down as shown in Fig. 4-3 (b) for three different values of the capacitor bank. This figure shows three different curves which belong to three different capacitor bank values. These curves are the corresponding curves for curve 2 in Fig. 4-3 (a). It can be seen in Fig. 4-3 (b) that a bigger capacitor bank results in self-excitation at a lower speed value, while a smaller capacitor bank demands a higher speed to achieve voltage build-up. However the minimum required magnetizing current remains the same for all the cases of capacitor bank size. The choice of the capacitor bank size in the dq simulation and the experiment is done based on the base speed of the machine. Later the magnetic core analysis is performed based on the obtained value, to calculate the residual flux in the machine's core.

The Energetic Model is used to obtain an estimation of the behavior of the core material. This model provides a proper estimation of the magnetic steel performance under various

excitation conditions. In the Energetic Model, the magnetic field intensity $H(t)$ is calculated using the relative magnetization [89, 90], as:

$$H(t) = H_d + \text{sgn}[m]H_R + \text{sgn}[m - m_0]H_l \tag{4.11}$$

where m is the relative magnetization. The first term in (4.11) represents the linear behavior of the material with H_d being the demagnetization field, and is defined as:

$$H_d = N_d M \tag{4.12}$$

where N_d is the demagnetization factor, and M is the total magnetization.

The nonlinear characteristics of the material such as saturation are presented using the second term in (4.11). In (4.11) H_R is the reversible field, and is defined as [89]:

$$H_R = h[[(1+m)^{(1+m)}(1-m)^{(1-m)}]^{\frac{g}{2}} - 1] \tag{4.13}$$

where h is a characteristic of the saturation field, and g defines the anisotropy.

The last term in (4.11) shows the hysteresis effects of the material such as remanence, coactivity, and static losses [90]. H_l is the irreversible field, and defined as [89, 90]:

$$H_l = (\frac{k}{\mu_0 M_s} + C_r H_r)(1 - \kappa \exp(-\frac{q}{\kappa}|m - m_0|)) \tag{4.14}$$

where k is related to hysteresis losses, and q is the ratio between the magnetic domain width and magnetic domain wall thickness [90]. μ_0, M_s, and m_0 are the relative permeability of the free space, saturation magnetization, and the initial state of the m. C_r is a factor which shows the dependency of the losses on the velocity of the displacement of the domain wall. κ defines the effect of the total magnetic state at the point of magnetization reversal.

Using the Energetic Model a BH loop corresponding to a specific level of field excitation is obtained which can predict the behavior of the core material. Therefore it enables us to estimate the remaining magnetism or the residual magnetic flux density in the core material as a result of a previous excitation with a given current magnitude. Fig. 4-4 (a) shows the estimated BH loop of the core material (M45 G29) using the Energetic Model for the maximum flux density of 1.22 T. It can be seen that a residual magnetism value of 0.9 T remains in the

core once the core material is magnetized up to 1.22 T. For the SynRM made of the same steel type, the value of the magnetic field intensity is calculated based on the winding configuration of the machine.

The magnetic field intensity of the machine is obtained according to the number of winding turns and the current flowing in the phase winding. As mentioned earlier the minimum required magnetizing current to ensure the occurrence of self-excitation is 5 A. The number of winding turns for the SynRM is 32. Thus 5 A phase current generates a magnetic field intensity equal to 160 A/m. According to the Energetic Model and the BH loop shown in Fig. 4-4 (a), The magnetic flux density produced in the steel material when exposed to 160 A/m field intensity, will be 1.22 T. Once the field is removed, the magnetic material will recoil to its residual flux density value (the magnetic flux density at zero field intensity) which is around 0.9 T, and is obtained using the Energetic Model, as shown in Fig. 4-4 (a). Thus the selected magnetizing current provides a residual flux density in the core with a magnitude of 0.9 T. The obtained residual flux density value from the Energetic Model is also validated with experimental results performed on the available steel sheets using the DONART test bench. In this experiment the steel type M45 G29 is tested and the dynamic BH loop of the steel is obtained for different field intensities.

The BH loop of M45 G29 steel is obtained from experiment using a DONART system, and shown in Fig. 4-4 (b). In this figure the BH loops of the steel for four different magnetization levels: 1 T, 1.3 T, 1.5 T, and 1.7 T are shown. According to Fig. 4-4 (b) if the steel is magnetized with a field intensity value that provides 1.3 T, the remnant magnetic flux density in the steel is 1.0375 T, when the field is removed.

(a)

0 60 Hz		06/18/2009			
Tesla	Area Under	W/Lb	HC	BR	Perm
1.000	2.902	0.816	0.8363	0.8218	7093
1.300	4.754	1.337	0.9769	1.0375	4174
1.500	6.637	1.866	1.0606	1.1301	1375
1.700	9.258	2.603	1.1414	1.1748	281
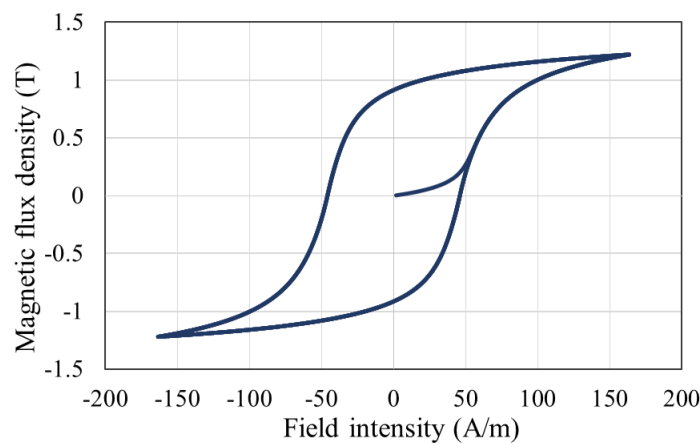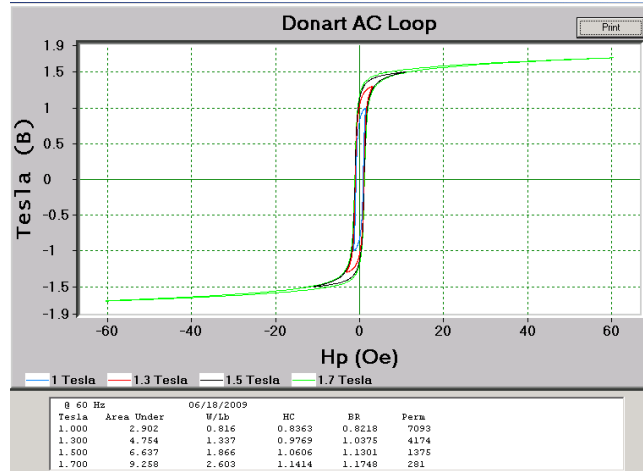
(b)

Fig. 4-4 (a) The BH loop of M45 G29 using the Energetic Model; (b) BH loops of M45 G29 obtained from the measurement

The value of the remnant magnetic flux density in the core depends on the steel material characteristics and reflects its features and possible appropriate applications. The core of electric machines is usually made of soft magnetic steels usually have low coercive force when compared to hard magnetic materials. This feature reduces the hysteresis loss in the core which is directly proportional to the surface area enclosed by the BH loop of the steel. Despite low coercivity values some soft magnetic steels can provide remnant magnetic flux densities similar to some permanent magnet materials, as it is shown here for M45 G29.

4.3.2. The Maximum Acceptable Acceleration

The effect of the residual magnetism in the core and the required current to provide it, was discussed in the previous section. However it is observed experimentally that although the presence of the residual flux in the machine's core is necessary for a successful self-excitation, it does not guarantee a successful voltage build-up. In other words, the occurrence of self-excitation depends not only on the presence of sufficient residual flux, but is also influenced by the start-up procedure of the SynRG, and more specifically the acceleration through which the rotor is driven to the rated speed (the value of speed is obtained in the previous section).

The effect of start-up acceleration can also be studied using the *dq* model of the SynRG and by analyzing the system parameters such as flux linkages, voltages, and currents. After examining various system parameters it is observed that the effect of start-up acceleration can be effectively demonstrated based on the *q*-axis flux linkage waveform. Therefore to identify

the influence of the speed on the occurrence of the successful voltage build-up using the *dq* model, the *q*-axis flux linkage is analyzed at different start-up acceleration values. Different start-up acceleration values are generated by ramp function in MATLAB Simulink®. Various slopes of the ramp function imposed on the SynRG create the effect of start-up acceleration from zero to the rated speed. In the experiments on the other hand, the DC machine which is used as the prime mover is controlled using a DC drive. The programmable DC drive enables us to control the rate of change of speed from zero to the rated speed. In order to identify the possible relation between the level of core pre-magnetization and the start-up acceleration, or their independency, each acceleration value is repeated for different magnetization current levels. Therefore the maximum acceleration which guaranties that the voltage build-up process takes place and the terminal voltage reaches its steady-state value is determined. After several experiments (presented in the next section) it is observed that the value of the pre-magnetization current and the consequent core residual magnetism and the start-up acceleration are decoupled; that is, for any value of the residual flux above the minimum value (calculated in the previous section), the same acceleration or less must be used so that self-excitation fully happens.

In this section the simulation results using MATLAB Simulink are presented. The *dq* model is used to identify the effect of start-up acceleration on the self-excitation process. Using equations (4.1) to (4.4) and based on the flux linkage-current curve of the machine that was used in the Simulink file as lookup tables, the effect of start-up acceleration on system parameters is studied. Using the ramp function with different slopes the effect of the prime mover acceleration value on the SynRG start-up transients is simulated. The waveform of *q*-axis*,* and *d*-axis, currents, flux linkages, and voltages for each simulation case are analyzed. Amongst the available parameters the effect of start-up acceleration on the *q*-axis flux linkage curve is more significant. The *q*-axis flux linkage curve represents the location of the flux linkage phasor of the SynRG during the start-up procedure and later in the steady-state condition. If the flux linkage phasor of the SynRG is located in the fourth quadrant (positive *d*-axis flux linkage and negative *q*-axis flux linkage), the machine is operating as a generator. This indicates that the rotor *d*-axis is leading the stator field and thus the machine is supplying active power (*q*-axis current to the load). On the other hand in motoring mode the *q*-axis flux linkage and *d*-axis flux linkage are both positive and the flux linkage phasor is located in the first quadrant. Thus the machine is receiving active and reactive power from the supply. Therefore

the sign of the q-axis flux linkage can indicate motoring or generating operation of the SynRM. The corresponding phasor diagrams of motor and generator operation of the SynRM are shown in Fig. 4-5. In this figure λ_s is the flux linkage vector of the stator.
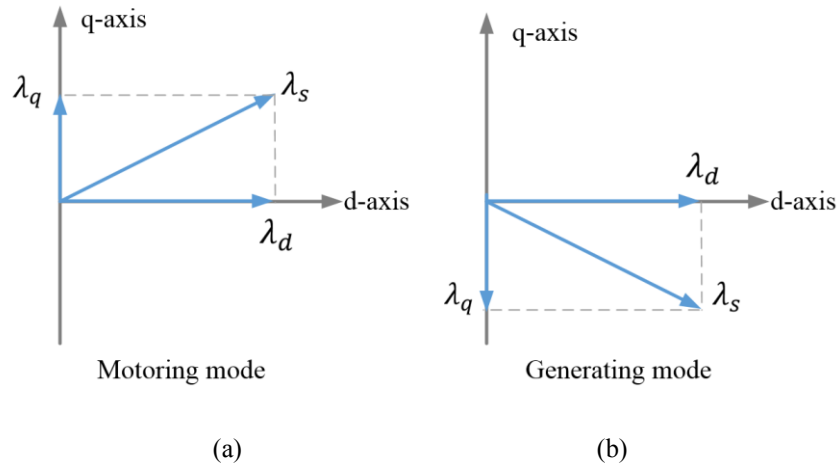
Fig. 4-5 Phasor diagram of the SynRM in motoring and generating modes

The effect of start-up acceleration on the q-axis flux linkage waveform of the SynRG is shown in Fig. 4-6. It is observed that a high acceleration value results in q-axis flux linkage and therefore current transients that will lead to demagnetization of the core material. Fig. 4-6 compares the q-axis flux linkage waveforms with two different acceleration values. Fig. 4-6 (a) shows the simulation result of the q-axis flux linkage during the self-excitation procedure for an acceleration value equal to 13 rad/s^2 (mechanical acceleration). With this acceleration value the rated speed is achieved in 10 seconds (from zero speed). It is observed that upon the moment of self-excitation the q-axis flux curve goes above zero. Therefore the SynRG starts operating as a motor for a short period of time. This sudden change in the operating mode results in core demagnetization and the loss of voltage build-up procedure. On the other hand in Fig. 4-6 (b) where the acceleration value is 4 rad/s^2, the rated speed is achieved in 32.5 seconds and the overshoot value of the q-axis flux linkage curve remains limited below zero (the fourth quadrant of the phasor diagram). This comparison shows the impact of the mechanical acceleration and the procedure through which the rated speed is achieved, on the occurrence of a successful self-excitation.

Fig. 4-6 (c) and (d) compare the effect of acceleration on the d-axis flux linkage curve of the SynRG. Although the effect of acceleration on the overshoot value of the d-axis flux linkage

is evident by comparing the two curves, since this overshoot does not result in a change in the sign of the *d*-axis flux linkage, no significant interpretation can be made by analyzing the *d*-axis flux linkage curve of the machine for different acceleration values.

The overshoot value of the *q*-axis flux linkage curve results in core demagnetization and a consequent voltage collapse. The effect of the acceleration on successful cases of self-excitation with different acceleration values is also significant both in experiments and simulations.

(a)

(b)

(c)

(d)
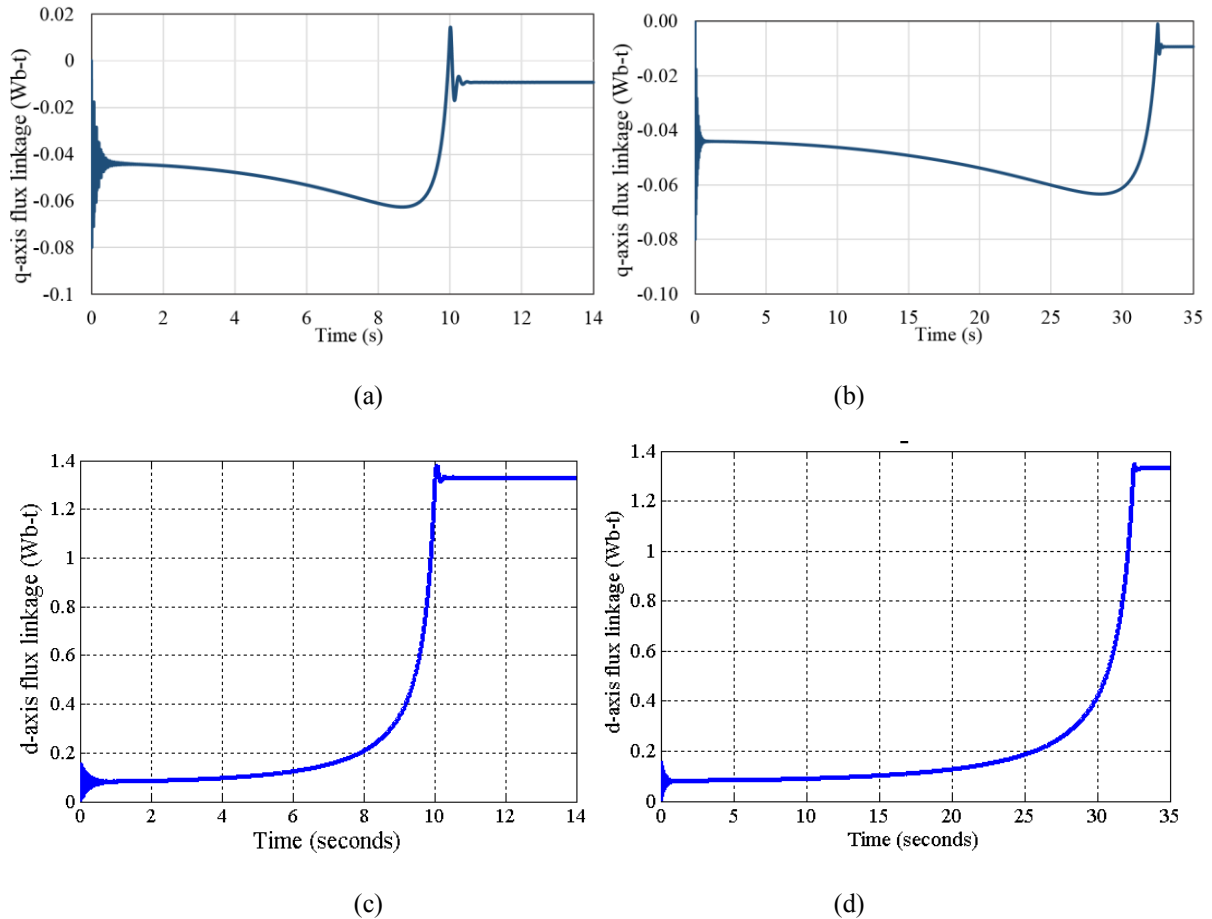
Fig. 4-6 The q-axis and d-axis flux linkages of the SynRG during the self-excitation process; (a) q-axis flux linkage, acceleration=13 rad/s²; (b) q-axis flux linkage, acceleration=4 rad/s² (mechanical acceleration), (c) d-axis flux linkage, acceleration=13 rad/s² (mechanical acceleration), (d) d-axis flux linkage, acceleration=4 rad/s² (mechanical acceleration)

Fig. 4-7 compares two cases of successful self-excitation. In Fig. 4-7 (a) with the acceleration equal to 6.5 rad/s², the overshoot of the phase voltage is 238.4 V, while in Fig. 4-7 (b) with an acceleration value equal to 5 rad/s², the overshoot value of the phase voltage is 237.5 V. Further increasing the acceleration results in higher overshoot values. For example with an acceleration

value of 100 rad/s² the overshoot value of the phase voltage is 256 V (more than 10 percent of the steady state peak voltage value). However this value of the acceleration is not experimentally tested. All system parameters such as phase winding resistance and capacitor are similar in the two cases. This reveals the effect of mechanical acceleration on the q-axis flux linkage as well as the phase voltage.
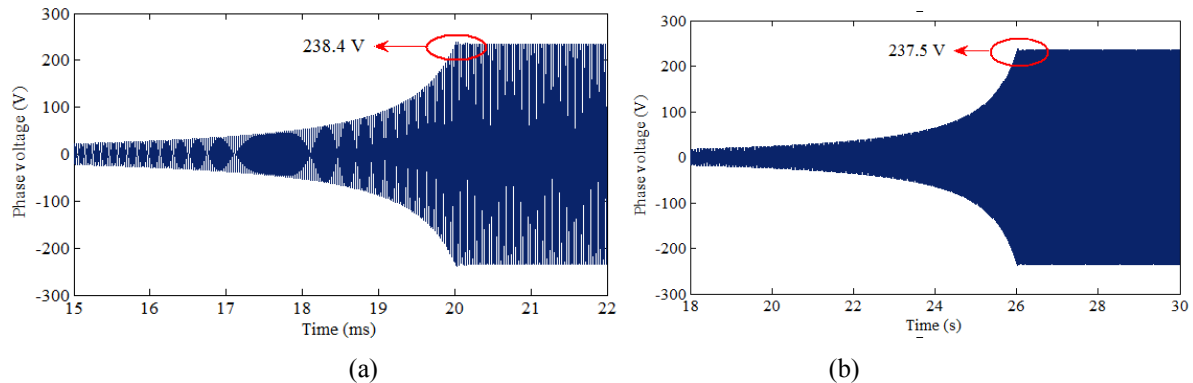
Fig. 4-7 The effect of mechanical acceleration on the overshoot value of the phase voltage; (a) 6.5 rad/s²; (b) 5 rad/s²

In the same manner the effect of system parameters such as phase winding resistance on the overshoot value of the q-axis flux linkage and the possible voltage build-up can be studied. During the experiments and normal operation of the SynRG the resistance of the winding changes due to temperature variations. The resistance variation affects the overshoot value of the q-axis flux linkage curve under similar acceleration values.

Fig. 4-8 (a) compares the q-axis flux linkage curves obtained for various phase resistance values. The mechanical acceleration and other system parameters are similar in all the cases. In this figure three resistance values; 1.3 Ω, 1.4 Ω, and 1.5 Ω are tested for an acceleration value of 4 rad/s². Although the phase winding resistance variation does not affect the magnitude of the overshoot value (see Fig. 4-8), it changes the steady state value of the q-axis flux linkage curve. It is observed in Fig. 4-8 that the variation in phase winding resistance shifts the q-axis flux linkage curve up or down. Thus it may result in a condition where despite the low acceleration value, the terminal voltage collapse due to the increased phase winding resistance. Therefore while operating the SynRM as a stand-alone generator the system parameters such as winding resistance must be considered in start-up procedure to ensure a successful voltage build-up.

Fig. 4-8 (b) and Fig. 4-8 (c) compare the effect of phase winding resistance on the *d*-axis flux linkage of the SynRG upon the moment of self-excitation for two value of the phase winding resistance; 1.4 Ohms and 1.5 Ohms, respectively. Although the overshoot value is different for the two cases, as explained earlier the occurrence of self-excitation cannot be predicted based on the *d*-axis flux linkage curve since the curve does not represent any changes in the sign of the flux linkage.
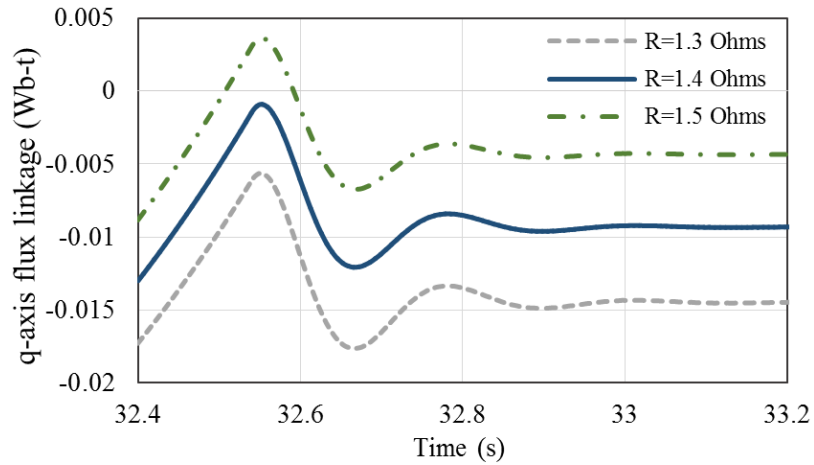
(a)
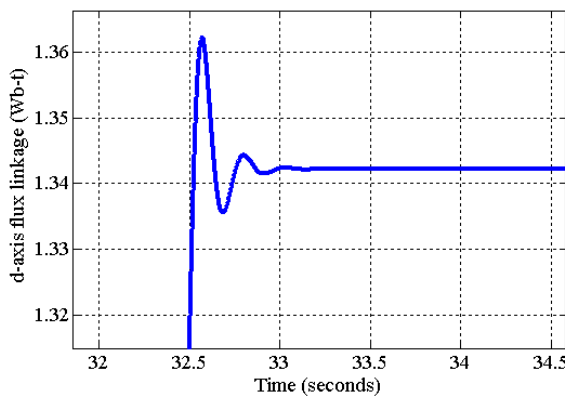
(b)
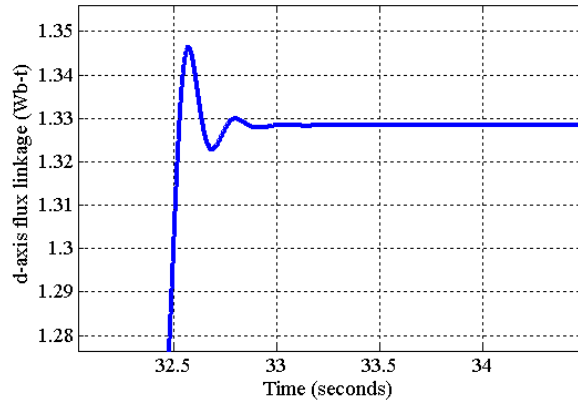
(c)

Fig. 4-8 (a) Effect of the phase winding resistance on the q-axis flux linkage waveform upon the self-excitation; (b) *d*-axis flux linkage for phase winding resistance of 1.4 ohms; (c) *d*-axis flux linkage for phase winding resistance of 1.5 ohms

4.4. Experimental Setup and Result

In this section the experimental setup of the stand-alone SynRG and the test procedure are initially introduced. Later the measurement results are presented and compared with the simulation results.

4.4.1. Experimental Setup

To verify the obtained results from *dq* simulations and mathematical analysis, a 5 hp SynRM, introduced in section 5.3 is connected to a 100 µF capacitor bank and operated as a stand-alone generator. The size of the capacitor bank is chosen based on the magnetization curve of the machine, rated speed, and the rated output voltage of the machine, and is explained in section 5.3. Fig. 4-9 shows the experimental setup including the SynRM, the DC motor (as the prime mover), the capacitor bank, and the measurement instruments. A programmable DC drive is used to control the acceleration of the DC motor (the prime mover) and thus the start-up process of the SynRG with different acceleration values. The speed of the DC machine and therefore the SynRG rotor speed is increased using a ramp function with the specified slope representing various acceleration values used in the simulation.

Initially the core of the SynRM is magnetized by connecting a DC supply to the machine's phase winding. At this stage the capacitors are disconnected to ensure that the initial capacitor voltage remains zero. Therefore the self-excitation is only studied based on the residual magnetism in the ferromagnetic core. The required time for applying the DC current and magnetizing the core depends on the time constant of the inductive-resistive circuit of the machine. Thus considering the *d*-axis inductance of the machine and the phase winding resistance this time constant will not be greater than 0.08 seconds. Once the core is magnetized, the DC supply is disconnected. At this stage the magnetic material follows its BH loop on the recoil line until it reaches its residual flux value shown in Fig. 4-4. Then the machine is connected to the capacitor bank and rotated using the prime mover as shown in Fig. 4-9. The test procedure is carried out for several values of the magnetizing current, ranging from 1 A to 10 A, and several acceleration values, ranging from 1.5 to 8 rad/s^2 (mechanical accelerations). After each experiment the machine is discharged using the resistor bank connected to the system. To perform this task after a successful self-excitation, the machine is stopped while connected to the resistor bank (as load). Therefore the current drawn by the load consumes the core magnetization and the voltage on the capacitors insuring a zero state condition for the future tests.

During the pre-magnetizing process using the DC supply, the rotor aligns with the produced static magnetic field, and is magnetized in the direction of the *d*-axis flux. During

this process, the stator is also magnetized. However the residual flux of the rotor core induces voltage in the stator phase winding, since the rotor is the only moving part of the machine. Therefore it is sufficient to only consider the effect of the residual magnetism in the rotor core, as also explained in the previous section.

Fig. 4-9 Experimental setup of the SynRG

4.4.2. Experimental Results

After pre-magnetizing the core and connecting the capacitor bank (100 μF capacitors), the SynRM is driven from zero speed to the rated speed (calculated in section 5.3) using the coupled DC motor (the prime mover) to the SynRM shaft. As stated earlier in this section the acceleration value to achieve the rated speed affects the occurrence of the self-excitation, and it is controlled by the programmable DC drive. Fig. 4-10 (a) shows the experimental voltage waveform of the SynRG during the self-excitation procedure. Fig. 4-10 (b) demonstrates the simulation result of the phase voltage obtained from the dq model of the SynRG system in similar condition.

At the initial start-up the machine operates in no-load condition. Thus it is only connected to the capacitor bank and the current which flows in the winding is the capacitor current (mainly the d-axis current component). The rms value of the phase current in the no-load condition (the magnetizing current required to maintain the generator operation of the machine) is around 5.7 A. Fig. 4-10 (b) depicts the simulation result for the phase voltage using the dq model in a similar condition. The rms value of the voltage in Fig. 4-10 (a) is 158.56 V and its frequency is 42.5 Hz. The simulation result shown in Fig. 4-10 (b) has the rms value of 159.8 V at 41.4 Hz.

The acceptable agreement between the simulation results and the experimental results shows the validity of the *dq* model and the estimated residual flux using the Energetic Model. Note that both figures are presenting the time span upon the self-excitation. Therefore the effect of acceleration cannot be observed clearly. However it is evident on the time axis (horizontal axis of Fig. 4-10). The *d*-axis and *q*-axis flux linkage curves obtained from the simulation for the case shown in Fig. 4-10 are similar to the ones shown in Fig. 4-6 (d) and Fig. 4-6 (b), respectively. The *q*-axis flux linkage curve of this operating condition is shown in Fig. 4-10 (c).

(a)

(b)

(c)
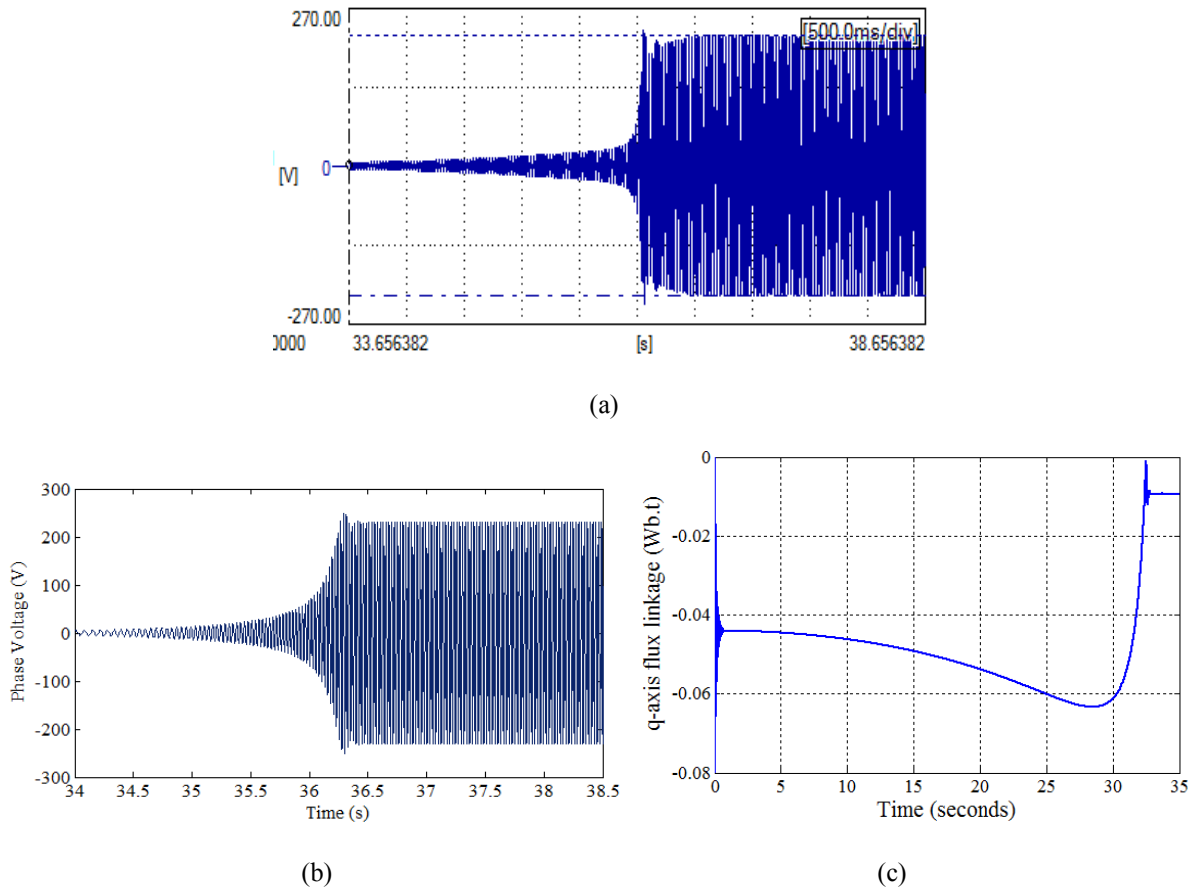
Fig. 4-10 Comparison of the phase voltage (a). Experimental result (b). Simulation using the dq model (c) *q*-axis flux linkage of the machine

Fig. 4-11(a), and (b) compare the line current waveforms of the SynRG obtained from the experiment and the *dq* model of the SynRG. The rms value of the current in the steady-state condition (after self-excitation transition) obtained from the measurement is 5.7 A, while the *dq* model steady state value of the current is 6.2 A. This difference can be explained based on the modeling method of the capacitor bank. In the *dq* model the capacitors are considered ideal.
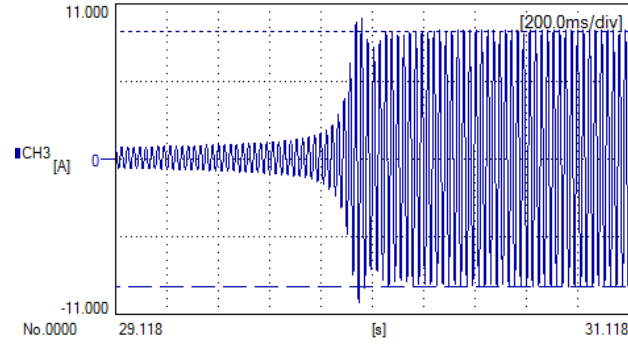
(a)
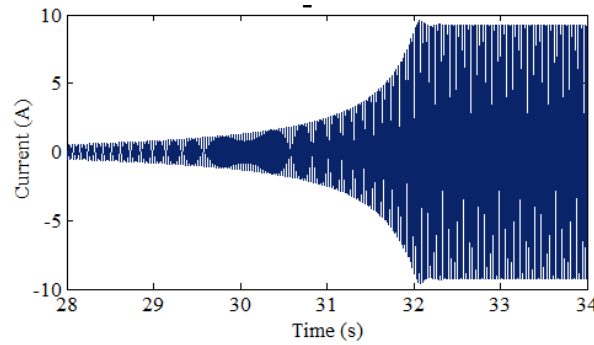
(b)

Fig. 4-11 Comparison of the line current; (a) Experimental result; (b) Simulation result

4.4.3. Experimental Study of the Residual Flux and Acceleration Value on the Self-Excitation Procedure of the SynRG

It was shown in the previous section that the amount of the residual flux and the start-up acceleration value of the SynRG must be considered for a successful voltage build-up. In this section it is shown that these two criteria for a successful self-excitation of the SynRG are independent from one another. In other words, to achieve the rated voltage in the steady-state condition both of the above mentioned criteria must be fulfilled. To identify the impact of the residual flux and the start-up acceleration value a set of experiments including various values of the pre-magnetization current (to assess the effect of the residual flux value), and different acceleration values (to assess the effect of the start-up acceleration value) are performed. Each value of the pre-magnetization current used for magnetizing the core prior to the start-up procedure is repeated for several start-up acceleration values. Therefore an estimation of the possible conditions for successful self-excitation of the SynRG is obtained.

116

The experimental results of the stand-alone SynRG operated from different initial conditions (residual magnetism), and various start-up acceleration values are presented in Fig. 4-12. In the figure, the blue circles represent the experiments which resulted in successful self-excitation and the red crosses represent the experiments which resulted in voltage collapse. As stated earlier the start-up acceleration is controlled using a DC drive that controls the speed of the DC motor (the prime mover), and the residual magnetism is provided using a DC supply which is connected to the machine's phase winding prior to the start-up procedure. This DC supply energizes the core according to the desired current magnitude. It is also important to demagnetize the core after each experiment to ensure that the residual flux value obtained from pre-magnetizing the core for the next experiment is mainly controlled by the pre-magnetizing current, and is not influenced by the previous operation.

The graph in Fig. 4-12 is divided into three sections. Area 1 characterized by high magnetization current (Above 5.5 A) and low acceleration (below 3.55 rad/s^2) is the area in which all the experiments resulted in a successful self-excitation of the generator. This means that if the magnetization current and the start-up acceleration value are within these boundaries, the successful self-excitation is assured to happen. Area 2 represents a threshold region in which there are points associated with experiments showing both a successful voltage build-up and a voltage collapse condition. In other words operating the SynRG with these initial condition values, and start-up acceleration values may or may not result in a successful voltage build-up. It was shown in section 5.3 that the system parameters such as winding resistance affects the transient values of the system parameters such as q-axis flux linkage. It was demonstrated that the variation in the winding resistance (due to heat for example) can result in a condition in which the same start-up acceleration value results in a voltage collapse condition. Therefore, such region of operation is considered unreliable for a successful self-excitation. The remaining points in Fig. 4-12 do not result in successful self-excitation and are located either below the minimum magnetization current (at 3.8 A) line or passed the maximum acceleration line (at 6 rad/s^2). Thus it is evident that using these initial residual magnetism values or starting the machine with these start-up acceleration values will not definitely result in voltage build-up.

Fig. 4-12 also shows that the maximum allowable acceleration affects the self-excitation procedure independently from the amount of the residual flux, since experiments which have

acceleration values above 6 rad/s^2 would not self-excite irrespective of the magnetization current used to pre-magnetize the core before the start-up procedure.
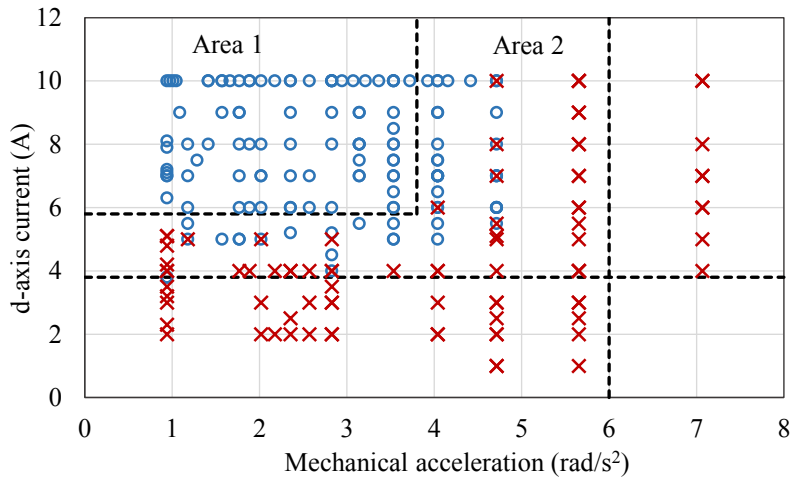
Fig. 4-12 SynRG test results summary

Fig. 4-13 (a) and Fig. 4-13 (b) show the two examples representing the same acceleration value, below the maximum allowable acceleration, with two different levels of pre-magnetization. In Fig. 4-13 (a) the machine is pre-magnetized with 7 A DC current prior to starting. Then the rotor is rotated using the prime mover with an acceleration value of 2.66 rad/s^2. Fig. 4-13 (b) shows an experimental result with the same acceleration value, but a lower pre-magnetizing current (4 A). The effect of low pre-magnetizing current can be clearly seen in these two figures, which shows the effect of the amount of residual flux on the self-excitation phenomenon.
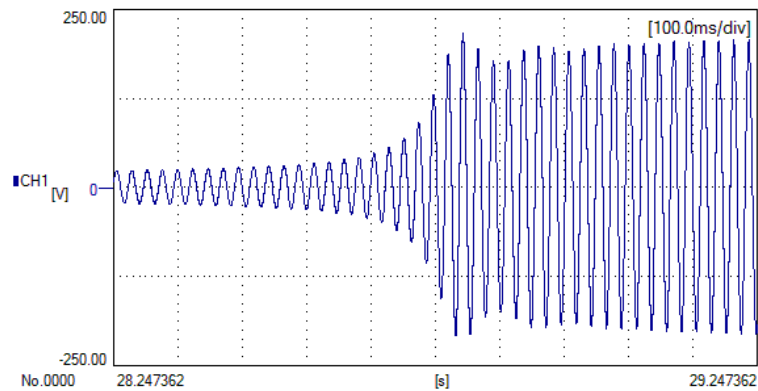
(a)
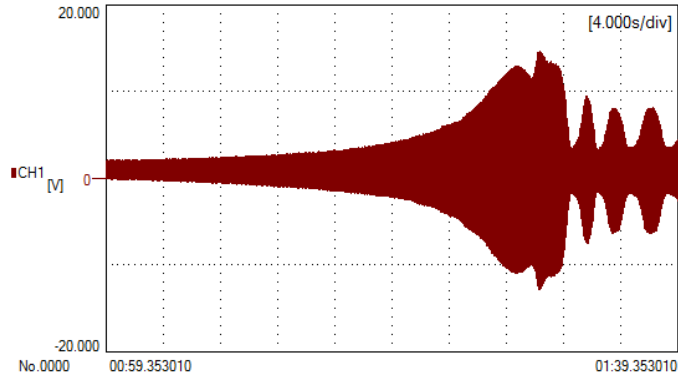
(b)

Fig. 4-13 Effect of the residual flux on the self-excitation; (a) Successful self-excitation after pre-magnetizing with 7 A; (b) Voltage collapse after pre-magnetizing with 4 A

The different accelerations applied to the shaft on the tests shows that even if the minimum residual flux is provided, the self-excitation is not guaranteed. Only acceleration values below the maximum acceptable acceleration will result in the voltage build-up. It was observed that above a certain acceleration (shown in Fig. 4-12) self-excitation will not happen irrespective of the amount of residual flux. However these two criteria define marginal boundaries which are depicted in Fig. 4-12.

Fig. 4-14 (a) and Fig. 4-14 (b) show the experimental result of the self-excitation after magnetizing the core with 7 A with different acceleration values. It can be seen that when the generator is accelerated faster than a certain value, which is depicted in Fig. 4-12, self-excitation does not occur and the terminal voltage collapses. Such experiments have been repeated several times with different magnetization currents and different accelerations, and the same results were achieved each time.
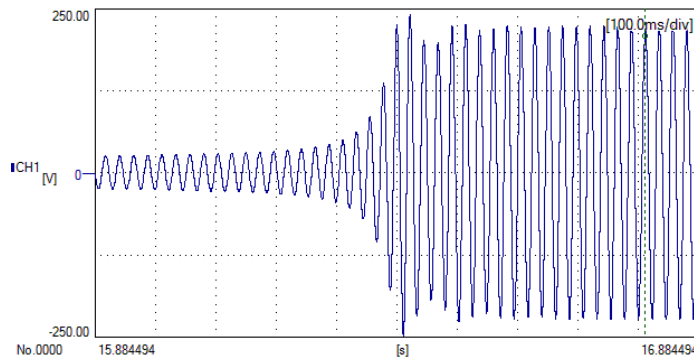
(a)
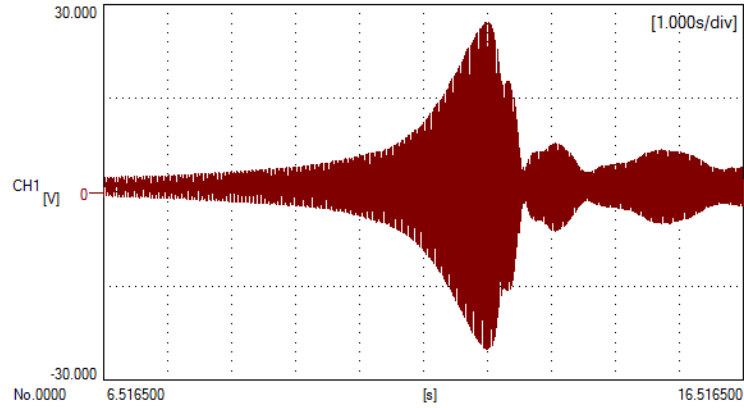
(b)

Fig. 4-14 Self-excitation after pre-magnetizing with 7 A; (a) Successful voltage build-up (acceleration=4 rad/s^2); (b) Voltage collapse due to fast acceleration (acceleration=5.8 rad/s^2)

The effect of start-up acceleration can also be observed by comparing Fig. 4-13 (a), and Fig. 4-14 (a). A higher acceleration value results in a bigger overshoot value in the phase voltage upon reaching the steady state value, as it is shown in the two figures. In Fig. 4-13 (a) with a lower acceleration value the overshoot value in the phase voltage is 214.69 V, while in Fig. 4-14 (a) the higher start-up acceleration has resulted in a larger overshoot value of the phase voltage which is equal to 240.63 V. This observation clearly shows the effect of start-up acceleration on the self-excitation phenomenon. In Fig. 4-13 (b), and Fig. 4-14 (b) which show the cases of unsuccessful self-excitation, the maximum value of the phase voltage right before the terminal voltage collapses, are different. For the case with sufficient initial condition (Fig. 4-14 (b)) the terminal voltage reaches around 30 V before it collapses due to fast acceleration. However in the case with insufficient initial condition (Fig. 4-13 (b)) the peak value of the terminal voltage is less than 15 V. This observation reveals the difference in the initial conditions the two cases are initiated from, and thus the origin of the failure in voltage build-up. A similar observation on the effect of initial condition and start-up acceleration on the self-excitation of a stand-alone SynRG is also reported in [91].

Although the effect of the minimum residual magnetism and the corresponding required pre magnetization current, and the acceleration can be explained using the *dq* model of the SynRG, the voltage collapse due to the two criteria cannot be observed in the simulations. As explained earlier in this chapter, the mathematical prediction of the equations (4.1) to (4.4) suggests that any non-zero initial condition can result in a successful voltage build-up. However the experiments show that there is a need for a minimum residual flux in the system

(as explained in this chapter). This minimum residual magnetism is obtained by analyzing the behavior of the system as shown in section 4.3.1. The effect of start-up acceleration on the voltage build-up process can be studied by analyzing the q-axis flux linkage of the machine as shown in section 4.3.2. However the voltage collapse due to high acceleration cannot be observed in the current dq model that is developed for the SynRG, since the lookup tables used for the d-axis and q-axis flux linkage curves do not include the conditions through which the machine is demagnetized due to high acceleration values. Although it is possible to analyze the q-axis flux linkage curve of the machine for various start-up acceleration values as demonstrated in section 4.3.2, and conclude the occurrence of the self-excitation accordingly. The effect of the required minimum residual flux and hence the required pre-magnetization current to obtain that, can also be studied by analyzing the system characteristics through the nonlinear system of equations as shown in section 4.3.1. However as discussed in the chapter since the mathematical analysis of the system predicts the occurrence of the self-excitation irrespective of the value of the initial condition in the system, the dq simulation cannot be directly used to conclude the successful voltage build-up. Therefore as demonstrated earlier in this chapter, the analysis of the system of equation of the SynRG is required to identify the minimum required residual flux and the required pre-magnetization current to achieve that.

4.5. Summary of the Chapter

In this chapter the stand-alone SynRG was presented and the criteria to ensure a successful self-excitation was identified. It was observed in the simulations that the voltage build-up procedure in SynRGs depends on maintaining a minimum required residual flux in the ferromagnetic core material prior to the start-up procedure. The required magnetizing current to provide the minimum required residual flux, was obtained using the dq model, the Energetic Model, and the machine's geometry and parameters. This observation was validated using several experiments performed on a stand-alone SynRG with different magnetization levels.

The effect of start-up acceleration on the q-axis flux linkage was also studied. It was shown that high acceleration values can create transients in the q-axis flux linkage waveform that leads to core demagnetization. Hence the maximum acceptable acceleration that creates acceptable transients was determined using simulations, and later verified by experiments. This value depends on the machine's characteristics, and must be identified using the dq model.

Above this maximum acceleration, the voltage build-up procedure will not take place fully and the terminal voltage will collapse after a few cycles. It was also shown that the phase winding resistance has a significant impact on the voltage build-up procedure. Therefore a successful self-excitation does not only depend on the presence of a minimum residual flux in the core, but also depends on the acceleration value through which the rated speed is achieved. The repeatability of the results for different magnetization currents and different acceleration shows the accuracy of the estimated value for the residual flux.

For a successful operation and start-up of the stand-alone SynRG the system parameters including the machine's characteristics (d and q axis inductances and phase winding resistance), the size of the capacitor bank, the rated speed of the machine, and type of the load (resistive, inductive, or capacitive) must be initially determined. Based on the machine's characteristics (d-axis and q-axis inductances) the minimum pre-magnetizing current, and the operational speed (which also depends on the size of the capacitor bank) must be identified. The system must be also simulated using the dq model and the q-axis flux linkage waveform should be analyzed to obtain the maximum acceptable start-up acceleration. Through this procedure the variation of system parameters, such as winding resistance as shown in this chapter, must also be considered for a successful voltage build-up procedure.

Chapter 5   Conclusion and Future Work

5.1.   Conclusion

In this thesis an analytical model for analysis, modeling, and design of SynRMs and PM assisted SynRMs was presented. The proposed model incorporates the effect of the flux barriers of the rotor of the SynRM in an air gap function. Based on the stator winding configuration, the winding function of the machine is obtained. Using the air gap function and the winding function, phase inductances of the machine are calculated and the electromagnetic torque of the machine is estimated using the coenergy method. The model was further expanded for modeling and characterization of a segmented-pole SynRM made of CRGO steel laminations. It was shown that the proposed method for incorporating the effect of the flux barriers of the SynRM, has the capability to include the main design parameters of the SynRM in the analytical model. Therefore geometrical features such as size and location of the rotor flux barriers, electric features such as winding configuration and winding turns, and magnetic features such steel permeability can be modeled using the proposed modeling approach. The model capability in SynRM characterization was tested using measurements and FEA simulations performed on a 7.5 hp SynRM. Although an acceptable agreement was observed between the results of the analytical model, and measurement results, some deviations were also noticed as presented in Chapter 2 since the proposed analytical model does not include the effect of steel saturation. Although incorporating the effect of saturation is possible as it was shown for the CRGO steel permeability, it adds up to the complexity of the analytical model. Therefore since the simplicity of the model is one of the main goals of this analytic approach, steel saturation was not considered.

Based on the proposed analytical model a segmented-pole SynRM made of CRGO steel laminations was also studied. It was observed from experiments, FEA simulation, and the analytical model that despite theoretical expectation, the application of CRGO steel does not have a significant impact on saliency ratio improvement of the SynRM. The proposed design topology is highly saturated due to the large flux barriers' widths, and the shape of the flux barriers do not allow for full utilization of the CRGO steel properties. Therefore a modified design was presented for a better utilization of the CRGO steel lamination. However since the effect of steel permeability compared to the effect of flux barriers on creating rotor saliency is

small, the obtained gain despite using a CRGO steel even in the modified segmented-pole SynRM is not significant.

The proposed analytical method was also used to design a PM assisted SynRM. In the proposed design topology the utilized permanent magnets are placed inside the rotor core in a manner to contribute to the d-axis flux of the machine. Instead of using rare-earth permanent magnet materials, AlNiCo magnets were used in order to reduce the manufacturing cost and also study the effectiveness of non-rare-earth permanent magnet materials on performance improvement of SynRMs. For a better comparison the finalized topology was also simulated considering N48 permanent magnet material (rare-earth magnet). The comparison revealed a slight improvement in the output torque and power factor of the PM assisted SynRM made of the rare-earth permanent magnet material when compared to the PM assisted SynRM made of AlNiCo 9 magnets. The final PM assisted SynRM was further characterized and compared with the SynRM based on torque-speed envelopes and efficiency map analysis. For the same DC bus voltage the base speed of the PM assisted SynRM is lower than the base speed of the SynRM with the same size. This is due to the induced back-EMF from the permanent magnets of the rotor. However the generated electromagnetic torque of the PM assisted SynRM is higher than the SynRM torque. The PM assisted SynRM also has a higher efficiency when compared to the SynRM as shown in Chapter 3.

In Chapter 4 the generator operation of the stand-alone SynRM was studied. It was shown that for a successful operation of the SynRG as a stand-alone power generation unit, certain criteria must be met. These criteria were identified using the dq model of the SynRG connected to a capacitor bank. It was observed that a minimum initial condition must be present in the system prior to the start-up procedure, and the start-up of the SynRG must be performed with an acceleration value below a maximum value. The minimum residual flux is a function of machine's geometry and magnetic characteristics that can be obtained by d-axis and q-axis inductance measurement. The maximum allowable start-up acceleration which is applied to the SynRG using the prime mover depends on machine's parameters such as d-axis inductance, q-axis inductance, phase winding resistance and the size of the capacitor bank. It was observed that for a successful self-excitation both of the abovementioned criteria must be fulfilled.

5.2. Future Work

This research work can be further extended to:

- The proposed analytical model in Chapter 2 can be extended to include more complicated features of the SynRM such as core saturation.

- The proposed analytical model has the capacity to incorporate various geometrical features such as slot effect, and various faulty conditions such as eccentricity, and winding faults. Such features can be included either in the winding function and the air gap function of the machine. Therefore the proposed analytical model can be used for modeling and analysis of the machine under faulty conditions.

- The analytical model can be modified as a general design tool in order to obtain the main design parameters of a SynRM based on the application requirement. To do so the torque equation of the SynRM which is dependent on the machine's dimensions, electric loading, and magnetic loading (as shown in Chapter 1) can be embedded in the analytical model. Therefore based on the application requirements the main dimensions of the machine can be estimated. Based on the obtained rotor outer diameter the number, shape, and sizes of the flux barriers can be determined in order to provide the required saliency ratio.

- The generator operation of the SynRG as an autonomous stand-alone power generation unit can be studied. In such system the SynRG is connected to a battery through a bidirectional power converter. The battery can supply the excess load if needed. It can also be used to provide the required initial condition if the SynRG is demagnetized due to a fault (as discussed in Chapter 5).

- The effect of start-up acceleration on the voltage collapse cases can be implemented in the MATLAB Simulink by incorporating the rate of the change of the q-axis flux linkage in the Simulink model. Therefore the occurrence of self-excitation can be predicted by studying the q-axis flux linkage curve of the SynRM.

References

[1] B. Kramer, S. Chakrabotry and B. Kroposki, "A Review of Plug-in Vehicles and Vehicle-to-Grid Capability," in Industrial Electronics, 2008. IECON 2008. 34th Annual Conference of IEEE, Orlando, FL, 2008.

[2] R. G. Gago, S. F. Pinto and J. F. Silva, "G2V and V2G Electric Vehicle Charger for Smart Grids," in IEEE International Smart Cities Conference (ISC2), Trento, Italy, 2016.

[3] X. Zhang, Q. Wang and G. Xu, "A review of Plug-in Electric Vehicles as Distributed Energy Storages in Smart Grid," in 5th IEEE OES Innovative Smart Grid Technologies Europe, Istanbul, 2014.

[4] F. Laureri, L. Puliga, M. Robba, F. Defino and G. Odena Bulto, "An Optimization Model for the Integration of Electric Vehicles and Smart Grids: Problem Definition and Experimental Validation," in IEEE International Smart Cities Conference (ISC2), Trento, Italy, 2016.

[5] S. Taghavi, Design of Synchronous Reluctance Machines for Automotive Applications, Montreal, QC, Canada: A Thesis in the Department of Electrical and Computer Engineering, Concordia University, Montreal, Canada, 2015.

[6] S. Taghavi and P. Pillay, "A Sizing Methodology of the Synchronous Reluctance Motor for Traction Applications," IEEE Journal of Emerging and Selected Topics in Power Electronics, vol. 2, no. 2, pp. 329-340, June 2014.

[7] A. Vagati, "The Synchronous Reluctance Solution: A New Alternative in AC Drives," in Industrial Electronics, Control and Instrumentation, 1994. IECON '94., 20th International Conference on, Bologna, 5-9 Sep 1994.

[8] A. Alolah, "Steady-State Operating Limits of Three Phase Self-Excited Reluctance Generator," Generation, Transmission and Distribution, IEE Proceedings C, vol. 139, no. 3, pp. 261-268, May 1992.

[9] S. Taghavi and P. Pillay, "A Comparative Study of Synchronous Reluctance Machine Performance with Different Pole Numbers for Automotive Applications," in Industrial Electronics Society, IECON 2014 - 40th Annual Conference of the IEEE, Dallas, TX, 2014.

[10] T. Matsuo and T. A. Lipo, "Rotor Design Optimization of Synchronous Reluctance Machine," IEEE Transactions on Energy Conversion, vol. 9, no. 2, pp. 359-365, June 1994.

[11] D. Staton, T. Miller and S. Wood, "Maximising the saliency Ratio of the Synchronous Reluctance Motor," Electric Power Applications, IEE Proceedings B, vol. 140, no. 4, pp. 249-259, July 1993.

[12] ABB, ABB, 2016. [Online]. Available: http://new.abb.com/motors-generators/iec-low-voltage-motors/frequency-controlled-motors/synchronous-reluctance-motor-drive-packages/synrm-verified-package-efficiency. [Accessed 2017].

[13] E. Obe, "Calculation of inductances and torque of an axially laminated synchronous reluctance motor," IET Electric Power Application, vol. 4, no. 9, pp. 783-792, December 2009.

[14] A. Ogunjuyigbe, A. Jimoh, D. Nicolae and E. Obe, "Analysis of synchronous reluctance machine with magnetically coupled three-phase windings and reactive power compensation," IET Electric Power Applications, vol. 4, no. 4, pp. 291-303, 2009.

[15] A. Vagati, A. Canova, M. Pastorelli, M. Chiampi and M. Repetto, "Design Refinement of Synchronous Reluctance Motors Through Finite-Element Analysis," IEEE Transaction on Industry Applications, vol. 36, no. 4, pp. 1094-1102, July/August 2000.

[16] N. Bedetti, S. Calligaro and R. Petrella, "Stand-Still Self-Identification of Flux Characteristics for Synchronous Reluctance Machines Using Novel Saturation Approximating Function and Multiple Linear Regression," IEEE Trans. on Industry Applications, vol. 52, no. 4, pp. 3083-3092, 2016.

[17] N. Bianchi, S. Bolognani and D. Bon, "Rotor flux barrier design for torque ripple reduction in synchronous reluctance and PM-assisted synchronous reluctance motors," IEEE Trans. on industry applications, vol. 45, no. 3, pp. 921-928, 2009.

[18] Z. Azar and Z. Q. Zhu, "Performance Analysis of Synchronous Reluctance Machines Having Nonoverlapping Concentrated Winding and Sinusoidal Bipolar with DC Bias Excitation," IEEE Trans. on Industry Applications, vol. 50, no. 5, pp. 3346-3356, 2014.

[19] M. Palmieri, M. Perta and F. Cupertino, "Design of a 50.000 r/min Synchronous Reluctance Machine for an Aeronautic Diesel Engine Compressor," IEEE Trans. on Industry Apllications, vol. 52, no. 5, pp. 3831-3838, 2016.

[20] H. Kiriyama, S. Kawano, Y. Honda and T. Higaki, "High Performance Synchronous Reluctance Motor with Multi-flux Barrier for the appliance industry," in Industry Applications Conference, 1998. Thirty-Third IAS Annual Meeting. The 1998 IEEE , St. Louis, MO, Oct. 1998.

[21] I. Boldea, Z. Fu and S. Nasar, "Performance Evaluation of Axially-Laminated Anisotropic (ALA) Rotor Reluctance Synchronous Motors," in Industry Applications Society Annual Meeting, 1992., Conference Record of the 1992 IEEE, Houston, TX, Oct. 1992.

[22] A. Vagati, G. Franceschini, I. Marongiu and G. Troglia, "Design Criteria of High Performance Synchronous Reluctance Motors," in Industry Applications Society Annual Meeting, 1992., Conference Record of the 1992 IEEE, Houston, TX, Oct. 1992.

[23] M. Ibrahim, L. Masisi and P. Pillay, "Design of Variable-Flux Permanent-Magnet Machines Using Alnico Magnets," IEEE Transactions on Industry Applications, vol. 51, no. 6, pp. 4482-4491, 2015.

[24] Y. Wang, N. Bianchi, S. Bolonami and L. Alberti, "Synchronous Motors for Traction Applications," in Electrical and Electronic Technologies for Automotive, 2017 International Conference of, Torino, Italy, 2017.

[25] A. Vagati, A. Canova, M. Chiampi, M. Pastorelli and M. Repetto, "Desing refinement of synchronous reluctance motors through finite-element analysis," IEEE Trans. on Industry Applications, vol. 36, no. 4, pp. 1094-1102, 2000.

[26] S. Maroufian and P. Pillay, "Torque characterization of a synchronous reluctance machine using an analytical model," in Power Electronics, Drives and Energy Systems (PEDES), 2016 IEEE International Conference on, Trivandrum, India, 2016.

[27] G. Bacco and N. Bianchi, "Choice of Flux-barriers Position in Synchronous Reluctance Machines," in Energy Conversion Congress and Exposition (ECCE), 2017 IEEE, Cincinnati, OH, USA, 2017.

[28] M. Degano, H. Mahmoud, N. Bianchi and C. Gerada, "Synchronous reluctance machine analytical model optimization and validation through finite element analysis," in Electrical Machines (ICEM), 2016 XXII International Conference on, Lausanne, Switzerland, 2016.

[29] C. M. Spargo, B. C. Mecrow and J. D. Widmer, "A Seminumerical Finite-Element Postprocessing Torque Ripple Analysis Technique for Synchronous Electric Machines Utilizing the Air-Gap Maxwell Stress Tensor," IEEE Trans. on Magnetics, vol. 50, no. 5, p. 7026909, 2014.

[30] X. Luo, A. El-Antably and T. A. Lipo, "Multiple coupled circuit modeling of synchronous reluctance machines," in Industry Applications Society Annual Meeting, Denver, CO, 1994.

[31] M. Kamper, "Effect of rotor dimensions and cross magnetisation on Ld and Lq inductances of reluctance synchronous machine with cageless flux barrier rotor," Electric Power Applications, IEE Proceedings, vol. 141, no. 4, pp. 213-220, Jul 1994.

[32] M. N. Fathy Ibrahim, A. S. Abdel-khalik, E. E. M. Rashad and P. Sergeant, "An Improved Torque Density Synchronous Reluctance Machine with a Combined Star-Delta Winding Layout," IEEE Transactions on Energy Conversion, vol. 33, no. 3, pp. 1015-1024, 2018.

[33] Z. Yang and F. Tadashi, "Direct Output Power Control for PWM Converter-Based Super-High-Speed Reluctance Generator," IEEE Trans. on Industry Application, vol. 28, no. 1, pp. 57-63, 1992.

[34] R. Moncada, B. Pavez, J. Tapia and J. Pyrhonen, "Operation Analysis of Synchronous Reluctance Machine in Electric Power Generation," in International conference on electrical machines (ICEM), Berlin, Germany, 2014.

[35] W. s. Abu-Elhaija and A. Muetze, "self-Excitation and stability at speed transients of Self-Excited Single-Phase Reluctance Generators," IEEE Trnas. on Sustainable Energy, vol. 4, no. 1, pp. 136-144, 2013.

[36] Y. Rahim, J. Fletcher and N. Hassanian, "Performance Analysis of Salient-Pole Self-Excited Reluctance Generators Using a Simplified Model," IET Renewable Power Generation, vol. 4, no. 3, pp. 253-260, 2010.

[37] A. Alolah, "Steady-state operating limits of three phase self-excited reluctance generator," IEE proceeding C generation and transmission, vol. 139, no. 3, pp. 261-268, 1992.

[38] S. Guha and N. C. Kar, "Saturation Modeling and Stability Analysis of Synchrnous Reluctance Generator," IEEE Trans. on Energy conversion, vol. 23, no. 3, pp. 814-823, 2008.

[39] N. Eldeen, A. M. Hassanian, A. Y. M. Abbas and A. S. G. Hussien, "Performance Analysis of Isolated Self-Excited Reluctance Generators. Connected to Diode Bridge Rectifier," SUST journal of engineering and computer science (JESC), vol. 16, no. 3, pp. 1-18, 2015.

[40] M. Anajjar and D. Gerling, "Synchronous Reluctance Generator with FPGA Control of Three-Level Neutral-Point-Clamped Converter for Wind Power Application," in Power Electronics and Motion Control Conference (PEMC), 2016 IEEE International, Varna, Bulgaria, 2016.

[41] A. E. Hoffer, R. H. Moncada, B. J. Pavez, J. A. Tapia and L. Laurila, "A High Efficiency control Strategy for Synchronous Reluctance Generator Including Saturation," in XXII International Conference on Electrical Machines (ICEM), Lausanne, Switzerland, 2016.

[42] T. Fukao, Z. Yang and M. Matsui, "Voltage Control of Super High-Speed Reluctance Generator System with a PWM Voltage Source Converter," IEEE Trans. on Industry Applications, vol. 28, no. 4, pp. 880-886, 1992.

[43] M. Bodson and O. Kiselychnyk, "Analysis of triggered self-excitation in induction generators and experimental validation," IEEE transactions on energy conversion , vol. 27, no. 2, pp. 238-249, 2012.

[44] M. Bodson and O. Kiselychnyc, "On the triggering of self-excitation in induction generators," in International symposium of power electronics, electrical drives automation and motion (SPEEDAM), Pisa, Italy, 2010.

[45] Y. Rahim, A. Mohamadien and A. Al Khalaf, "Comparison between the Steady-State performance of Self-Excited Reluctance and Inducion Generators," IEEE Trans. on Energy Conversion, vol. 5, no. 3, pp. 519-525, 1990.

[46] Y. Tan, K. M. Muttaqi, L. Meegahapola and P. Ciufo, "Deadband Control of Doubly-Fed Induction Generator Around Synchrnous Speed," IEEE Trans. on energy Conversion, vol. 31, no. 4, pp. 1610-1621, 2016.

[47] O. Ojo and W. Zhiqing, "Synchronous operation of a dual-winding reluctance generator," IEEE transactions on energy conversion, vol. 12, no. 4, pp. 357-362, 1997.

[48] I. Boldea, Z. Fu and S. Nasar, "High performance synchronous reluctance generator," IEE proceeding B electric power applications, vol. 140, no. 2, pp. 124-130, 1993.

[49] M. E. Baran and A. J. Goetze, "Equivalent Circuits of AC Machines Based on Field Analyis," IEEE Trans. on Power Systems, vol. 9, no. 2, pp. 565-572, 1994.

[50] V. Ostovic, Dynamics of Saturated Electric Machines, New York: Springer-Verlag Inc., 1989.

[51] M. Amrhein and P. T. Krein, "Force Calculation in 3-D Magnetic Equivalent Circuit Networks with a Maxwell Stress Tensor," IEEE Trans. on Energy Conversion, vol. 24, no. 3, pp. 587-593, 2009.

[52] A. J. Pina, Y. Alsmadi and L. Xu, "Analytical Model for the Minimization of Torque Ripple in Permanent Magnets Assisted Synchronous Reluctance Motors Through Asymmetric Rotor Poles," in Energy Conversion Congress and Exposition (ECCE), Montreal, QC, Canada, 2015.

[53] T. Lipo, Analysis of Synchrnous Machines, Second edition, Boca Raton, FL: CRC Press, Taylor and Francis Group, 2012.

[54] N. A. Al Nuaim and H. Toliyat, "A Method for Dynamic Simulation and Detection of Dynamic Air gap Eccentrcicity in Synchronous Machines," in IEEE International Electric Machines and Drives, Milwaukee, WI, USA, 1997.

[55] R. Qu and T. Lipo, "General Closed-Form Analytical Expressions for Air gap Inductances for surface-mounted Permanent Magnet and Induction Machines," in IEEE International Electric Machines and Drives Conference, Madison, WI, USA, 2003.

[56] O. Ojo, A. Ginart, O. Omozusi and A. Jimoh, "Modeling and Analysis of a Single-Phase Synchronous Reluctance Machine Including Saturation Effect," in IEEE Industry Application Society Annual Meeting, New Orleans, Louisiana, USA, 1997.

[57] I. Sadeghi, H. Ehya and J. Faiz, "Analytic method for eccentricity fault diagnosis in salient-pole synchronous generators," in International Conference on Optimization of Electrical and Electronic Equipment (OPTIM) & 2017 Intl Aegean Conference on Electrical Machines and Power Electronics (ACEMP), Brasov, Romania, 2017.

[58] I. Boldea, Reluctance Synchronous Machines and Drives, Oxford: Clarendon press, 1996.

[59] N. Bianchi and B. Chalmers, "Axially Laminated Reluctance Motor: Analytical and Finite-Element Methods for Magnetic Analysis," IEEE Trans. on Magnetics, vol. 38, no. 1, pp. 239-245, 2002.

[60] S. Taghavi and P. Pillay, "A Novel Grain-Oriented Lamination Rotor Core Assembly for a Synchronous Reluctance Traction Motor With a Reduced Torque Ripple Algorithm," IEEE Trans. on Industry Applications, vol. 52, no. 5, pp. 3729-3738, 2016.

[61] K. J. Meessen, J. J. H. Paulides and E. A. Lomonova, "Force Calculation in 3-D Cylindrical Structures Using Fourier Analysis and the Maxwell Stress Tensor," IEEE Trans. on Magnetics, vol. 49, no. 1, pp. 536-545, 2013.

[62] H. VuXuan, D. Lahaye, S. Ani, H. Polinder and J. Ferreira, "Effect of Design Parameters on Electromagnetic Torque of PM Machines with Concentrated Windings Using Nonlinear Dynamic FEM," in IEEE International Electric Machines and Drives Conference (IEMDC), Niagra Falls, ON, 2011.

[63] N. Bianchi, E. Fornasiero and W. Soong, "Optimal Selection of PM Flux Linkage in a PM Assisted Synchronous Reluctance Machine," in Electrical Machines (ICEM), Berlin, Germany, 2014.

[64] J. Kitao, Y. Takahashi, K. Fujiwara, A. Ahgon, t. Matsuo and A. Daikoku, "Input and Output Power in Finite-Element Analysis of Electric Machines Taking Account of Hysteretic Property," IEEE Trans. on Magnetics, vol. PP, no. 99, pp. 1-4, 2017.

[65] A. Takbash, M. Ibrahim and P. Pillay, "Torque ripple reduction of a variable flux motor," in Energy Conversion Congress and Exposition (ECCE), 2016 IEEE, Milwaukee, WI, USA, 2016.

129

[66] S. Mishara, T. A. Lipo and S. V. Pamidi, "Design and analysis of a novel brushlesshigh temperature superconducting synchronous machine," in Electric Machines and Drives Conference (IEMDC), 2017 IEEE International, Miami, FL, USA, 2017.

[67] S. Taghavi and P. Pillay, "A Novel Grain-Oriented Lamination Rotor Core Assembly for a Synchronous Reluctance Traction Motor with a Reduced Torque Ripple Algorithm," IEEE Trans. on Industry Applications, vol. 52, no. 5, pp. 3729-3738, 2016.

[68] H. Cai, B. Guan and L. Xu, "Low-Cost Ferrite PM-Assisted Synchronous Reluctance Machine foe Electric Vehicles," IEEE Trans. on Industrial Electronics, vol. 61, no. 10, pp. 5741-5748, 2014.

[69] M. Barcaro, T. Pradella and I. Furlan, "Low-Torque Ripple Design of a Ferrite-Assisted Synchronous Reluctance Motor," IET Electric Power Applications, vol. 10, no. 5, pp. 319-329, 2015.

[70] N. Bianchi, S. Bolognani, D. Bon and M. Dai Pre, "Torque Harmonic Compensation in a Synchronous Reluctance Motor," IEEE Trans. on Energy Conversion, vol. 23, no. 2, pp. 466-473, 2008.

[71] H. Cong Liu, I.-G. Kim, Y. Jun Oh, J. Lee and S.-C. Go, "Design of Permanent Magnet-Assisted Synchronous Reluctance Motor for Maximized Back-EMF and Torque Ripple Reduction," IEEE Trans. on Magnetics, vol. 53, no. 6, pp. 1-4, 2017.

[72] T. A. Huynh and M.-F. Hsieh, "Comparative Study of PM-Assisted SynRM and IPMSM on Constant Power Speed Range for EV Applications," IEEE Transaction on Magnetics, vol. 53, no. 11, pp. 1-6, 2017.

[73] Y. Wang, G. Bacco and N. Bianchi, "Geometry Analysis and Optimization of PM-Assisted Reluctance Motors," IEEE Transaction on Industry Applications, vol. 53, no. 5, pp. 4338-4347, 2017.

[74] P. Guglielmi, G. Giraudi, G. Pellegrino and A. Vagati, "P.M. Assisted Synchronous Reluctance Drive for Minimal Hybrid Application," in Conference Record of the 2004 IEEE Industry Applications Conference, 2004. 39th IAS Annual Meeting., Seattle, WA, USA, 2004.

[75] M. Gamba, G. Pellegrino and A. Vagati, "A New PM-Assisted Synchronous Reluctance machine with a nonconventional fractional slot per pole combination," in Optimization of Electrical and Electronic Equipment (OPTIM), 2014 International Conference on, Bran, Romania, 2014.

[76] W. Zhao, F. Xing, X. Wang, T. A. Lipo and B.-i. Kwon, "Design and Analysis of a Novel PM-Assisted Synchronous Reluctance Machine with Axially Integrated Magnets by the Finite-Element Method," IEEE Trans. on Magnetics, vol. 53, no. 6, 2017.

[77] N. Bianchi, E. Fornasiero, M. Ferrari and M. Castiello, "Experimental Comparison of PM-Assisted Synchronous Reluctance Motors," IEEE Trans. on Industry Applications, vol. 52, no. 1, pp. 163-171, 2016.

[78] M. Barcaro and N. Bianchi, "Interior PM Machines using Ferrite to Substitute Rare–Earth Surface PM Machines," in International conference on Electrical Machines (ICEM), Marseille, France, 2012.

[79] R. Lohninger, H. Grabner, G. Weidenholzer, S. Silber and W. Amrhein, "Modeling, simulation, and Design of a Permanent Magnet Assisted Synchronous Reluctance Machine," IEEE Transaction on Industry Applications, vol. 51, no. 1, pp. 196-203, 2015.

[80] J. Baek, S. S. Reddy Bonthu, S. Kwak and S. Choi, "Optimal design of five-phase permanent magnet assisted synchronous reluctance motor for low output torque ripple," in Energy Conversion Congress and Exposition (ECCE), 2014 IEEE, Pittsburgh, PA, USA, 2014.

[81] M. T. Bin Tarek and S. Choi, "Design and rotor shape modification of a multiphase high speed permanent magnet assisted synchronous reluctance motor for stress reduction," in Energy Conversion Congress and Exposition (ECCE), 2017 IEEE, Cincinnati, OH, USA, 2017.

[82] D. C. Hanselman, Brushless Permanent-Magnet Motor Design, Orono, Maine: McGraw-Hill, Inc., 1994.

[83] T. J. E. Miller, Brushless Permanent Magnet and Reluctance Motor Drives, New York: Clarendon Press OXFORD, 1989.

[84] O. Ojo, "Limit-Cycle and Small Signal Dynamics of Self-Excited Snchronous Reluctance Generator," in 26th southeastern Symposium of System Theory, Athens, Ohio, USA, 1994.

[85] O. Ojo, G. Dong and M. Osaretin Omoigui, "Analysis of a Synchronous Reluctance Machine with an Auxiliary Single-Phase Winding," IEEE Transaction of Industry Applications, vol. 39, no. 5, pp. 1307-1313, 2003.

[86] S. Maroufian and P. Pillay, "Self-excitation criteria of the synchronous reluctance generator in stand-alone mode of operation," in IEEE International Conference on Power Electronics, Drives and Energy Systems (PEDES), Trivandrum, India, 2016.

[87] S. S. Maroufian and P. Pillay, "Self-Excitation Criteria of the Synchronous Reluctance Generator in Stand-Alone Mode of Operation," IEEE Transactions on Industry Applications, vol. 54, no. 2, pp. 1245-1253, 2018.

[88] M. Bodson and O. Kiselynchynk, "On the Capacitor Voltage Needed to Trigger Self-Excitation in Induction Generators," in 19th Mediterranean Conference on control and Automation, Pisa, Italy, 2011.

[89] Y. Zhang, P. Pillay, M. Ibrahim and M. C. Cheng, "Magnetic characteristic and core losses in machine laminations: high frequency loss prediction from low frequency measurements," IEEE transactions on industry applications, vol. 48, no. 2, pp. 623-629, 2011.

[90] H. Hauser, Y. Melikhov and D. C. Jiles, "Examination of the equivalence of ferromagnetic hysteresis models describing the dependence of magnetization on magnetic field and stress," IEEE Transaction on Magnetics, vol. 45, no. 2, pp. 1940-1949, 2009.

[91] Y. Wang and N. Bianchi, "Investigation of Self-Excited Synchronous Reluctance Generators," IEEE Transaction on Industry Applications, vol. 54, no. 2, pp. 1360-1369, 2017.